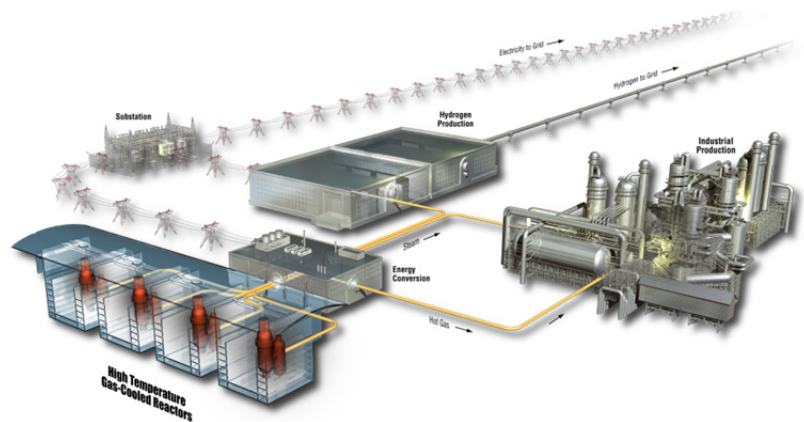


# AGR-1 Compact 5-3-1 Post-Irradiation Examination Results

Paul A. Demkowicz  
Philip L. Winston  
Jason M. Harp  
Scott A. Ploger

December 2016

The INL is a  
U.S. Department of Energy  
National Laboratory  
operated by  
Battelle Energy Alliance



**DISCLAIMER**

This information was prepared as an account of work sponsored by an agency of the U.S. Government. Neither the U.S. Government nor any agency thereof, nor any of their employees, makes any warranty, expressed or implied, or assumes any legal liability or responsibility for the accuracy, completeness, or usefulness, of any information, apparatus, product, or process disclosed, or represents that its use would not infringe privately owned rights. References herein to any specific commercial product, process, or service by trade name, trade mark, manufacturer, or otherwise, does not necessarily constitute or imply its endorsement, recommendation, or favoring by the U.S. Government or any agency thereof. The views and opinions of authors expressed herein do not necessarily state or reflect those of the U.S. Government or any agency thereof.

# **AGR-1 Compact 5-3-1 Post-Irradiation Examination Results**

**Paul A. Demkowicz  
Philip L. Winston  
Jason M. Harp  
Scott A. Ploger**

**December 2016**

**Idaho National Laboratory  
INL ART Program  
Idaho Falls, Idaho 83415**

**<http://www.inl.gov>**

**Prepared for the  
U.S. Department of Energy  
Office of Nuclear Energy  
Under DOE Idaho Operations Office  
Contract DE-AC07-05ID14517**



INL ART Program

AGR-1 Compact 5-3-1 Post-Irradiation  
Examination Results

INL/EXT-15-36354  
Revision 0

December 2016

Reviewed by:

  
\_\_\_\_\_  
John D. Stempien  
Advanced Gas Reactor Fuel Program Post-Irradiation  
Examination Technical Lead

12/01/2016  
\_\_\_\_\_  
Date

Approved by:

  
\_\_\_\_\_  
Travis R. Mitchell  
INL ART Project Manager

12/1/2016  
\_\_\_\_\_  
Date

  
\_\_\_\_\_  
Michelle T. Sharp  
INL Quality Engineer

12/1/16  
\_\_\_\_\_  
Date

  
\_\_\_\_\_  
Paul A. Demkowicz  
Advanced Gas Reactor Fuels Program Lead

12/1/16  
\_\_\_\_\_  
Date



## SUMMARY

Destructive post-irradiation examination was performed on Advanced Gas Reactor (AGR)-1 fuel Compact 5-3-1, which was irradiated to a final compact-average burnup of 16.93% fissions per initial metal atom and a time-average, volume-average temperature of 1040°C. Analysis of this compact focused on characterizing the extent of fission product release from the particles, examining particles to determine the condition of the kernels and coating layers, and experimentally verifying the fuel burnup. Work included deconsolidation of the compact and leach-burn-leach analysis, visual inspection and gamma counting of individual particles, measurement of isotopic inventories in the fuel by mass spectrometry and subsequent burnup calculations, analyzing the fission product inventory in the kernels and coating fragments separately in a small number of particles, metallurgical preparation of selected particles, and examination of particle cross-sections with optical microscopy.

Deconsolidation-leach-burn-leach (DLBL) analysis revealed no particles with failed tristructural isotropic or failed silicon carbide (SiC) layers (as indicated by a very low uranium inventory in all of the leach solutions). The DLBL data also provided information on the inventory of fission products retained in the compact outside of the SiC layers. The total fraction of the predicted Ag-110m inventory in the DLBL solutions was  $9.07 \times 10^{-3}$ , indicating significant release from the particles and retention in the compact matrix or outer pyrolytic carbon during irradiation. Cesium inventory was very low; the fraction of the compact inventory in the DLBL solutions was  $2.45 \times 10^{-6}$  and  $6.46 \times 10^{-6}$  for Cs-134 and Cs-137, respectively. Cerium and europium were found at levels greater than the equivalent inventory in one particle, and strontium levels were almost as high, indicating the release of small quantities through intact SiC. The data also revealed that the Pd-105 inventory in the compact outside of SiC was approximately 0.5% of the predicted compact inventory, indicating release through intact coatings and retention in the matrix or outer pyrolytic carbon at nearly the same level as silver.

Gamma counting of individual particles revealed that the level of silver release spanned a very large range (the ratio of measured-to-calculated Ag-110m inventory for 58 gamma counted particles ranged from 1.05 to less than 0.15). The average measured-to-calculated activity ratio for all other isotopes measured with gamma spectrometry was below a value of 1.0; this is believed to be due to a bias in the predicted values for the particles and not to a significant release from the particles. One particle was identified with a very low inventory of all fission products measured, suggesting that the particle had abnormally low fissile content at the beginning of irradiation. However, cermographic examination of this particle in the cross-section did not reveal any obvious features that would explain the low fission product inventory.

Investigation of the fission product inventory in kernels and coating fragments recovered from 13 fractured particles indicated that cerium and ruthenium remain almost entirely in the kernels. In contrast, the behavior of cesium exhibited a large variability, with two particles having a relatively small fraction of Cs-134 remaining in the kernels (average of 0.1), while the remaining particles retained a large fraction in the kernels (average of 0.9). The reason for the relatively low retention in two of the kernels is not yet known. The fraction of Eu-154 retained in the kernels exhibited a bimodal distribution. The average fraction retained in the kernels in one population of six particles was 0.93; these particles also exhibited the highest level of silver retention among the particles tested prior to removing the coating layers. The average fraction retained in the kernels in the second population was 0.62. These particles correspond to those with the lowest level of silver retention among the particles examined. These data indicate that the level of europium retained in the kernels correlates with silver retention in the intact particles and therefore may be related to differences in the irradiation temperature of the particles. Data for all of the isotopes suggest that fission products found in the recovered coating fragments is primarily located in the buffer layer.

The morphology of the kernels, buffer layers, and inner pyrolytic carbon (IPyC) layers in the deconsolidated Compact 5-3-1 particles examined is generally similar to that observed during ceramography of AGR-1 compact cross sections. Specifically, many particles displayed a continuous gap between the buffer and IPyC layers that was driven by buffer densification and followed by buffer-IPyC debonding during irradiation. Partial debonding occurred in many other particles along the observable buffer-IPyC interface. Approximately 18% of the particles exhibited fractures in the buffer layer.

IPyC fracture tendencies observed in deconsolidated Compact 5-3-1 particles reinforced findings from ceramography of Compact 5-1-2 cross sections. AGR-1 Variant 1 fuel was again found to be more likely than other fuel types to contain fractures through the entire IPyC layer with IPyC-SiC debonds at the crack tips. IPyC-SiC debonds were found more frequently in particles with IPyC cracks when the particles were examined at multiple levels. One individually cross-sectioned particle is of interest, as it exhibits a coating morphology (IPyC fracture and IPyC-SiC delamination) that may be indicative of the preliminary stages of SiC failure. This particle has been preserved for future microanalysis and comparison with particles with similar coating morphology, but evidence of SiC failure.

Although several particles examined in cross-section exhibited an extreme range of measured Ag-110m inventory (i.e., measured-to-calculated activity ratios in the examined particles ranged from less than 0.18 to 1.05), no obvious correlations between particle morphology and silver release were observed. Several cross-sectioned particles have been selected for future detailed examination using electron microscopy and elemental analysis to explore the behavior of fission products in the coating layers.

## **ACKNOWLEDGEMENTS**

The valuable contributions of numerous Idaho National Laboratory staff members in performing experimental work and data analysis are acknowledged. This includes Martin Kearns (performing deconsolidation-leach-burn-leach analysis, particle inspection, particle gamma counting, and mount loading), Jeffrey Berg (technical direction and data analysis of deconsolidation-leach-burn-leach results), Dr. Jeffrey Giglio and Daniel Cummings (inductively coupled plasma-mass spectroscopy experiments and data analysis), Brian Storms (particle gamma counting and Sr-90 analysis), and Brian Frickey and Cad Christensen (preparation of ceramographic mounts).



# CONTENTS

SUMMARY .....	vii
ACKNOWLEDGEMENTS .....	ix
ACRONYMS .....	xv
1. INTRODUCTION .....	1
1.1 Background .....	1
1.2 Compact 5-3-1 Post-Irradiation Examination Objectives and Overview .....	2
2. DECONSOLIDATION-LEACH-BURN-LEACH .....	4
3. PARTICLE INSPECTION AND GAMMA COUNTING .....	10
3.1 Visual Inspection .....	10
3.2 Particle Gamma Counting .....	10
4. BURNUP ANALYSIS .....	18
5. PARTICLE CRACKING AND GAMMA COUNTING OF KERNELS AND COATINGS .....	21
5.1 Particle Selection and Kernel Recovery, Inspection, and Diameter Measurement .....	21
5.2 Kernel and Coating Gamma Counting .....	24
5.3 Kernel and Coating Analysis Conclusions .....	30
6. PARTICLE MOUNT PREPARATION AND CERAMOGRAPHY .....	31
6.1 Single Particle Mounts .....	31
6.1.1 Particle AGR1-531-059 (Mount 19U) .....	35
6.1.2 Particle AGR1-531-038 (Mount 20U) .....	36
6.1.3 Particle AGR1-531-019 (Mount 21U) .....	38
6.1.4 Particle AGR1-531-006 (Mount 22U) .....	38
6.1.5 Particle AGR1-531-031 (Mount 23U) .....	40
6.1.6 Particle AGR1-531-033 (Mount 24U) .....	40
6.1.7 Particle AGR1-531-018 (Mount 25U) .....	41
6.1.8 Fission Product Behavior .....	42
6.2 Mount U4 .....	42
6.2.1 Preparation and Examination .....	42
6.2.2 Mount U4 Ceramography Results .....	45
6.3 Future Work .....	48
7. COMPACT 5-3-1 POST-IRRADIATION EXAMINATION RESULTS SUMMARY .....	48
8. LESSONS LEARNED AND RECOMMENDATIONS .....	49
9. REFERENCES .....	49
Appendix A Deconsolidation-leach-burn-leach Procedure .....	52
Appendix B Particle Inspection and Irradiated Microsphere Gamma Analysis .....	57

## FIGURES

Figure 1. Photograph (left) and x-radiograph (right) of an unirradiated AGR-1 fuel compact. UCO kernels and non-fueled end caps are clearly visible in the x-radiograph. .... 2

Figure 2. PIE flowchart for Compact 5-3-1. .... 3

Figure 3. AGR-1 Compact 5-3-1 deconsolidation in Cell 5 showing accumulated particles on thimble frit. .... 4

Figure 4. High turbidity between 35 and 45 minutes. .... 5

Figure 5. Image of particles from AGR-1 Compact 5-3-1 following burn-leach analysis. .... 11

Figure 6. Decay-corrected Ce-144 activity in 60 particles from AGR-1 Compact 5-3-1. Particle AGR1-531-018 had abnormally low Ce-144 activity. .... 14

Figure 7. M/C activity ratios for several isotopes determined from gamma scanning intact Compact 5-3-1 (Harp 2014) and from gamma counting individual particles. .... 17

Figure 8. Ag-110m M/C activity ratios for 60 gamma-counted particles from AGR-1 Compact 5-3-1. Red data represents particles for which no Ag-110m was detected; therefore, the minimum detectable activity was used to calculate the M/C ratio. The location of specific particles chosen for mounting and microanalysis are labeled on the distribution. .... 18

Figure 9. Images of kernels and coating debris recovered after particle cracking. (a) particle AGR1-531-013 kernel, (b) coating fragments, (c) kernel from particle AGR1-531-050 adjacent to graticule markings, (d) kernel from particle AGR1-531-047 showing a piece of adhered buffer layer, (e) kernel from particle AGR1-531-016 exhibiting a ridge of kernel that extruded into a buffer crack during irradiation, and (f) kernel from particle AGR1-531-037 with essentially complete buffer layer still attached. .... 22

Figure 10. Distribution of estimated kernel diameters based on an analysis of the images. The two particles at the upper end of the distribution are AGR1-531-008 and AGR1-531-037. .... 23

Figure 11. Fraction of original particle inventory that was measured in the kernels and coatings of cracked particles. .... 25

Figure 12. Correlation between the fraction of the original intact particle inventory of Ru-106 and Ce-144 recovered in coating fragments from 13 AGR-1 Compact 5-3-1 particles. .... 27

Figure 13. Images of the kernels from particles AGR1-531-002 and AGR1-531-016. .... 28

Figure 14. The fraction of the original Eu-154 inventory in each particle that was found in the recovered kernel vs. the estimated particle size of the recovered kernel. .... 29

Figure 15. The relationship between the Ag-110m M/C activity ratio in the intact particles and the fraction of the original intact particle inventory of Eu-154 (left), and Cs-134 (right) that was found in the recovered kernels. .... 30

Figure 16. Cross-sectional diagram through center of a Compact 5-3-1 single particle mount. .... 33

Figure 17. Dial indicator-based mount thickness gauge with standards and mount centering holders. .... 34

Figure 18. Beta-browned epoxy surrounding particle AGR1-531-059 (left) and irregular separation near its kernel-buffer interface (right).	36
Figure 19. Kernel protrusions into fractured buffer cavities in particle AGR1-531-038.	37
Figure 20. Thin strips of buffer adhering to the IPyC interior near kernel protrusions in particle AGR1-531-038.	37
Figure 21. Outer buffer peeling and unusual kernel features in particle AGR1-531-019.	38
Figure 22. SiC fractures from preparation (left) and details near IPyC fracture (right) in particle AGR1-531-006.	39
Figure 23. Rotated buffer inside IPyC layer (left) and uranium carbide skin separation (right) in particle AGR1-531-031.	40
Figure 24. Type Ai particle AGR1-531-033.	41
Figure 25. Buffer fracture pattern (left) and kernel microstructure (right) in particle AGR1-531-018.	41
Figure 26. Design and particle loading arrangement in Mount U4.	43
Figure 27. Montage of Mount U4 at the seventh level examined.	44
Figure 28. Mount U4 particles at seventh level, rotated after some grinding (left) and partially covered by back-pot (right).	44
Figure 29. Mount U4 multi-level results (average 4.5 levels) versus single level results from Mount U4 and Compact 5-1-2 cross sections.	45
Figure 30. Frequency of IPyC cracks by particle type for cross-sectioned AGR-1 compacts and deconsolidated, burned back particles in Compact 5-3-1 Mount U4.	46
Figure 31. The only Mount U4 particle with SiC cracks, shown at the sixth polish level examined.	47
Figure 32. IPyC cracks, IPyC-SiC debonds, and SiC fractures from Level 4 (left) to Level 9 (right).	47
Figure A-1. Deconsolidation configuration.	54
Figure A-2. Framework with deconsolidation tube/vial (left) and two Soxhlet extractor stations.	55
Figure B-1. Cutaway view of the camera optical orientation without shielding.	58
Figure B-2. Assembled isometric view of macroscope stages and shielding.	59
Figure B-3. Post deconsolidation particle viewed on the end of the vacuum tweezer needle.	60
Figure B-4. MFC Analytical Laboratory Cell 4 spectrometer configuration.	61
Figure C-1. Particle morphologies observed in AGR-1 fuel particle cross sections, where “i” denotes an intact buffer and “f” denotes a fractured buffer (Ploger et al. 2012).	64

## TABLES

Table 1. Identification and irradiation conditions for AGR-1 Compact 5-3-1.....	3
Table 2. Predicted inventory of isotopes in AGR-1 Compact 5-3-1 based on physics calculations (Sterbentz 2013). .....	6
Table 3. Fission products in the deconsolidation and leach solutions from Compact 5-3-1 expressed as decay-corrected activity (Bq) and compact fraction (based on calculated inventories [Sterbentz 2013]). .....	7
Table 4. Uranium and plutonium inventory in the deconsolidation and leach solutions from Compact 5-3-1 expressed as total mass ( $\mu\text{g}$ ) and compact fraction (based on calculated inventories [Sterbentz 2013]). .....	8
Table 5. Inventory of selected fission products determined by ICP-MS analysis of the Compact 5-3-1 DLBL solutions, expressed as total mass ( $\mu\text{g}$ ) and compact fraction (based on calculated inventories [Sterbentz 2013]). .....	9
Table 6. Decay-corrected activities (in Bq) for isotopes measured by gamma counting of particles from irradiated Compact 5-3-1. ....	11
Table 7. Ratio of measured isotope activity in particles AGR1-531-018 and AGR1-531-046 to the average activity in all analyzed particles. ....	15
Table 8. Average M/C activity ratios for 58 gamma-counted particles. Note that the averages do not include the contribution from particles AGR1-531-018 and AGR1-531-046. ....	16
Table 9. Mass spectrometry burnup data compared to other techniques in % FIMA. ....	19
Table 10. Comparison of measured actinide content to simulation. ....	20
Table 11. The M/C Ag-110m activity ratio of particles cracked for recovery of the kernels and the estimated diameter of the kernels after removal of the coating layers. ....	21
Table 12. Fraction of original intact particle inventory in the kernels and coatings and the totals. ....	26
Table 13. Compact 5-3-1 particle mounts. ....	32

## ACRONYMS

AGR	advanced gas reactor
ATR	Advanced Test Reactor
C/E	calculated-to-experimental
DLBL	deconsolidation-leach-burn-leach
EML	Electron Microscopy Laboratory
EOI	end of irradiation
FIMA	fissions per initial metal atom
HF	hydrofluoric acid
HFEF	Hot Fuel Examination Facility
ICP-MS	inductively coupled plasma mass spectroscopy
IPyC	inner pyrolytic carbon
M/C	measured-to-calculated
MFC	Materials and Fuel Complex
OPyC	Outer pyrolytic carbon
PIE	post-irradiation examination
SiC	silicon carbide
TRISO	tristructural isotropic
UCO	Uranium oxide, uranium carbide fuel



# AGR-1 Compact 5-3-1 Post-Irradiation Examination Results

## 1. INTRODUCTION

### 1.1 Background

The Advanced Gas Reactor (AGR) Fuel Development and Qualification Program was established to perform the requisite research and development on tristructural isotropic (TRISO)-coated particle fuel to support deployment of a high-temperature gas-cooled reactor. The work continues as part of the Advanced Reactor Technologies TRISO Fuel Program. The overarching program goal is to provide a baseline fuel qualification dataset to support licensing and operation of a high-temperature gas-cooled reactor. To achieve these goals, the program includes the elements of fuel fabrication, irradiation, post-irradiation examination (PIE) and safety testing, fuel performance, and fission product transport (INL 2015).

A series of fuel irradiation experiments is being planned and conducted in the Advanced Test Reactor (ATR) at Idaho National Laboratory (INL). These experiments will provide data on fuel performance under irradiation, support fuel process development, qualify the fuel for normal operating conditions, provide irradiated fuel for safety testing, and support the development of fuel performance and fission product transport models. The first of these irradiation tests, designated AGR-1, began in the ATR in December 2006 and ended in November 2009. This experiment was conducted primarily to act as a shakedown test of the multicapsule test train design and provide early data on fuel performance for use in fuel fabrication process development. It also provided samples for post-irradiation safety testing, where fission product retention of the fuel at high temperatures will be experimentally measured. Capsule design and details of the AGR-1 experiment have been presented previously (Grover, Petti, and Maki 2010, Maki 2009).

The AGR-1 uranium oxide, uranium carbide (UCO) fuel kernels were fabricated by Babcock & Wilcox (now BWX Technologies) Nuclear Operations Group (Barnes et al. 2008). Kernels were nominally 350  $\mu\text{m}$  in diameter and  $^{235}\text{U}$  enrichment was 19.74%. The TRISO coatings were applied at Oak Ridge National Laboratory. Nominal coating thicknesses were 100  $\mu\text{m}$  for the porous carbon buffer, 40  $\mu\text{m}$  for the inner pyrolytic carbon (IPyC) layer, 35  $\mu\text{m}$  for the silicon carbide (SiC) layer, and 40  $\mu\text{m}$  for the outer pyrolytic carbon (OPyC) layer. The coated particles were formed into right cylindrical compacts at Oak Ridge National Laboratory that were nominally 12.4 mm in diameter and 25.1 mm in length. The fuel compacts have about 1.5-mm thick fuel-free end caps at the top and bottom (Figure 1). A baseline fuel type and three fuel variants were included in the AGR 1 irradiation, with each variant fabricated by varying one step of the coating process to produce slightly different IPyC or SiC coating properties (Hunn, Jellison, and Lowden 2007). A summary of particle and compact properties is presented in the AGR-1 Test Plan (Maki 2009). One key goal of the experiment is to identify any fuel performance differences between the fuel types, either during irradiation or during post-irradiation high-temperature safety tests, to support optimization of the fuel fabrication process and the eventual selection of a reference fuel for qualification.

A total of 72 compacts were irradiated in the AGR-1 experiment. The experiment completed 620 effective full-power days in the reactor and achieved a peak calculated compact-average burnup of 19.6% fissions per initial metal atom (FIMA) with zero particle failures observed, based on the measured fission gas release-to-birth rate ratios (Grover, Petti, and Maki 2010). At the completion of irradiation, the test train was shipped to the Materials and Fuels Complex (MFC) at INL to initiate PIE and high-temperature safety testing. The primary objectives of the AGR-1 PIE and safety testing were to (a) assess the overall performance of the test train and components and provide data to verify the test train thermal analyses, (b) evaluate the fission product retention of the fuel during irradiation and

high-temperature post-irradiation safety tests, and (c) characterize the fuel compacts and individual particles to assess the condition of the matrix material, kernels, and coatings and to document any concerns. Details of the activities planned as part of PIE and safety testing, including planned activities for specific compacts, have been described in the AGR-1 Post-Irradiation Examination Plan (Demkowicz 2010).

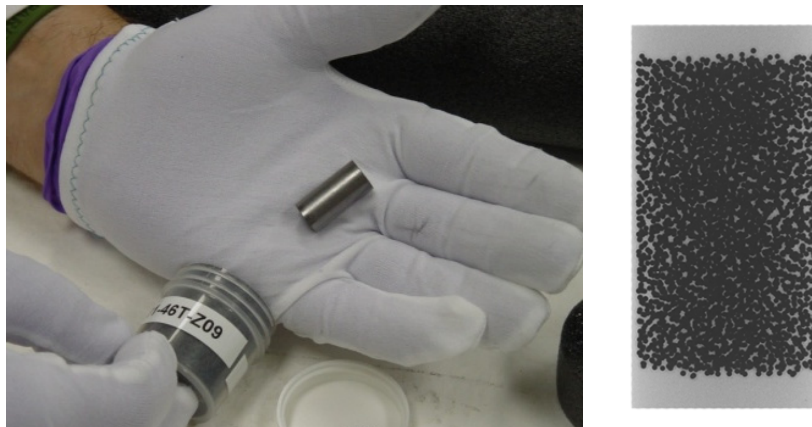


Figure 1. Photograph (left) and x-radiograph (right) of an unirradiated AGR-1 fuel compact. UCO kernels and non-fueled end caps are clearly visible in the x-radiograph.

Upon receipt at the MFC Hot Fuel Examination Facility (HFEF), the AGR-1 test train was unpackaged, visually inspected, and examined using gamma spectrometry. The test train was then sectioned into individual capsules that were opened to remove the fuel compacts and other internal capsule components for PIE. The fuel compacts, graphite fuel holders, and metal capsule shells were measured to determine the degree of dimensional change that occurred during irradiation. Results of test train inspection and nondestructive examination, disassembly, and dimensional measurements are presented in the report titled, *AGR-1 Irradiated Test Train Preliminary Inspection and Disassembly First Look* (Demkowicz et al. 2011). All irradiated AGR-1 fuel compacts were also gamma scanned in axial increments to determine the inventory of fission products and experimentally measure burnup prior to proceeding with destructive PIE (Harp 2014).

## 1.2 Compact 5-3-1 Post-Irradiation Examination Objectives and Overview

Compact 5-3-1 is composed of Variant 1 fuel particles and was located in Level 3, Stack 1 of Capsule 5 in the AGR-1 experiment (Maki 2009). Details of fuel fabrication and properties are presented in the AGR-1 Variant 1 particle and compact data packages (Hunn and Lowden 2006a; Hunn, Montgomery, and Pappano 2006). Some of the irradiation conditions for this compact are listed in Table 1. The specific PIE objectives for Compact 5-3-1 are as follows:

1. Perform deconsolidation-leach-burn-leach (DLBL) analysis to (a) identify the number of particles with failed SiC that may be present in the compact, (b) determine the inventory of fission products outside the SiC layer, and (c) provide particles for subsequent examination.
2. Perform gamma-ray spectrometry on a subset of particles to quantify the inventory of major fission products to examine variations in fission product retention.
3. Examine kernel and coating microstructures of selected particles to better understand fuel irradiation behavior and mechanisms of fission product diffusion and release. Examination methods include optical microscopy, electron microscopy (e.g., scanning electron microscopy and transmission

electron microscopy), and elemental analysis (e.g., energy dispersive spectroscopy and wavelength dispersive spectroscopy).

4. Perform burnup analysis on a subset of particles using mass spectrometry and compare values to those calculated based on physics simulations of the AGR-1 irradiation.
5. Separate coatings from kernels in a subset of particles, visually examine the particle components after separation, and gamma count the kernels and coating separately to assess the inventory of fission products in each.

A flowchart of the analysis that has been completed on Compact 5-3-1 is provided in Figure 2.

Table 1. Identification and irradiation conditions for AGR-1 Compact 5-3-1.

Compact ID <sup>a</sup>	Fabrication ID	Fuel Type	Burnup (% FIMA <sup>b</sup> )	Fast Fluence $\times 10^{25}$ (n/m <sup>2</sup> ) <sup>b</sup>	Irradiation Temperature (°C) <sup>c</sup>
AGR-1 5-3-1	LEU01-47T-Z23	Variant 1	16.93	3.60	1040

a. The X-Y-Z naming convention denotes the location in the irradiation test train: Capsule-Level-Stack.  
b. Based on physics calculations (Sterbentz 2013).  
c. Volume-averaged, time-averaged temperature, based on thermal calculations (Hawkes 2012).

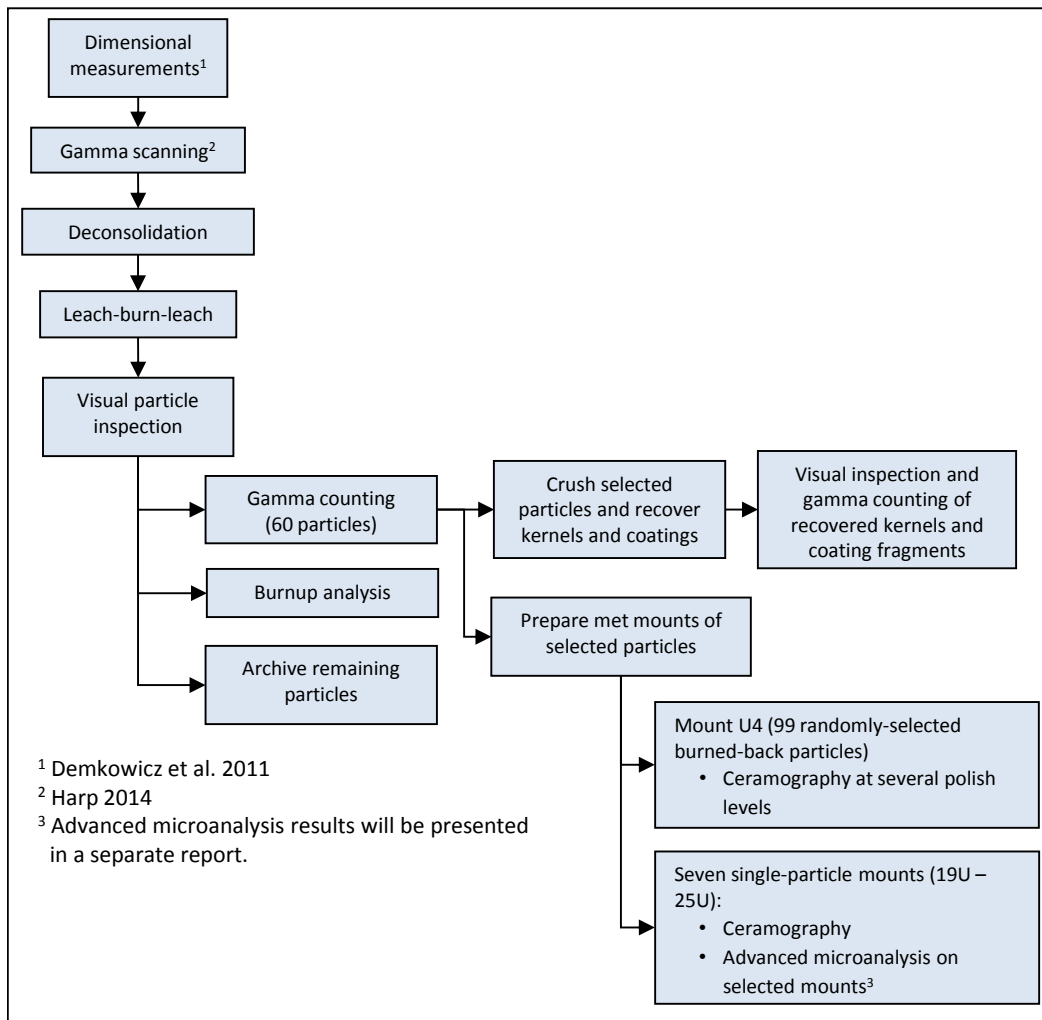


Figure 2. PIE flowchart for Compact 5-3-1.

## 2. DECONSOLIDATION-LEACH-BURN-LEACH

The general process for compact DLBL analysis is given in Appendix A. Compact 5-3-1 was received in the Analytical Laboratory on September 9, 2011. Receipt weight was 5.3183 g. The DLBL process was performed in Hot Cell 5 in the Analytical Laboratory A-wing. Deconsolidation was performed September 27, 2011. Total deconsolidation time was 189 minutes. During deconsolidation, the power supply was in constant voltage mode set at 10 volts. Deconsolidation average power input was 7.8 watts. The process began with the beaker slightly overfilled due to one of the power switches being off initially. Particles began to drop through the perforated support grid and continued to do so rather slowly for the next 60 minutes. Heavy turbidity was observed between 35 and 45 minutes. Particle separation rate was very slow between 55 and 60 minutes. After allowing the system to sit undisturbed from 60 to 115 minutes due to limited change in the compact, it was determined that the support grid had become plugged with approximately 6 mm of particle and matrix debris. Between 115 and 150 minutes, the power supply was turned off and the anode foot and deconsolidation tube were moved in an attempt to dislodge the plug in the deconsolidation tube support grid. At 150 minutes, the voltage was adjusted to 11 V, the power supply was reset to constant current control mode, and bubbling was noted at the anode foot. The compact appeared to have been completely consumed. At 180 minutes, the blockage in the deconsolidation tube was cleared by moderate agitation of the deconsolidation tube. Figure 3 and Figure 4 show some photographs taken during various stages of deconsolidation.

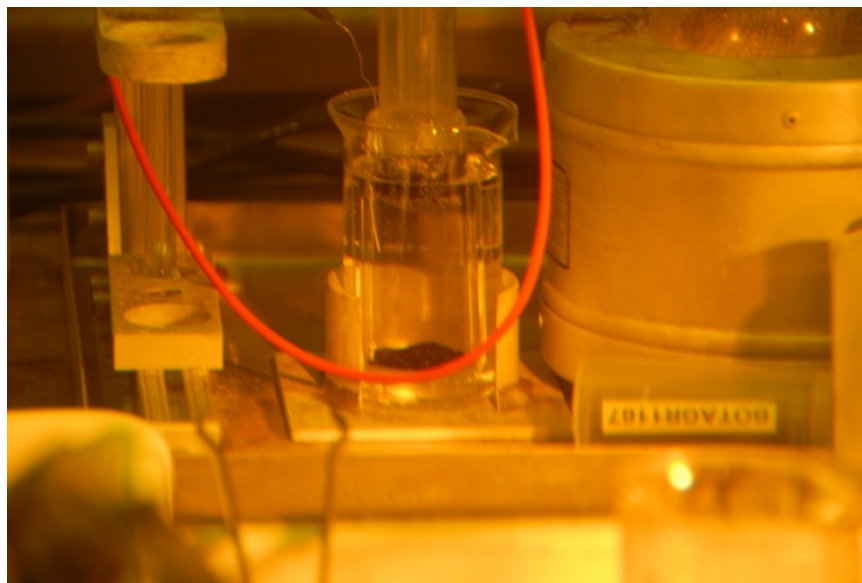


Figure 3. AGR-1 Compact 5-3-1 deconsolidation in Cell 5 showing accumulated particles on thimble frit.

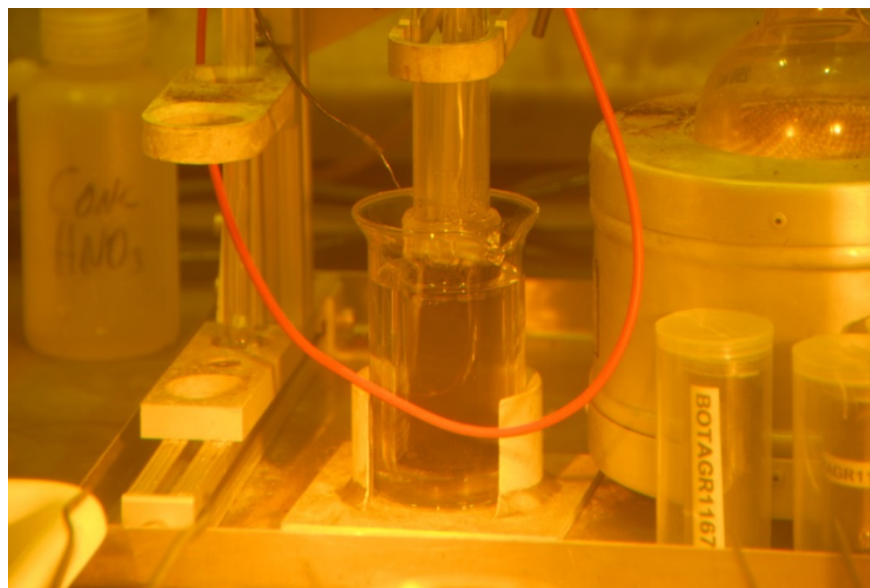


Figure 4. High turbidity between 35 and 45 minutes.

The first two 24-hour pre-burn leaches were performed on September 27 and 28, 2011. The period for the siphon cycle during the first leach was 10 minutes. The thimble drained approximately 25% during each cycle (i.e., approximately 75% of the solution remained in the thimble during each siphon cycle). Incomplete draining occurred because fines plugged the frit at the bottom of the thimble. The siphon cycle time for the second pre-burn leach was also 10 minutes. Both leach steps were completed in 24 hours.

Following the second pre-burn leach step, the thimble was transferred to a covered fused-silica beaker, which was put into the Vulcan muffle furnace. The operating temperature of 750°C was reached on September 30, 2011. The oxidation step was completed on October 3, 2011. To ensure that a consistent oxygen flow was maintained, the furnace external ventilation fan was adjusted to yield a flow rate that caused the pinwheel mounted above the exhaust chimney to barely rotate.

The post-burn leaches were started on October 4 and completed on October 6, 2011. Both leach steps had 24-hour durations. Siphon cycle times for the first leach was 11 minutes. The second leach started at the 11-minute cycle time, but increased to 41 minutes after 19 hours and then to 21 minutes at 22 hours, presumably as a function of the amount of fines on the thimble frit. Approximately 60% of the solution remained in the thimble during each siphon cycle for the first leach. The second leach started with approximately 60% remaining in the thimble during each cycle, but this decreased to 20% by the end of the step.

No grab samples of the particles were taken at intermediate steps during the DLBL process. The net weight of the resulting post-burn-leach particles was 2.4417 g.

The deconsolidation solution and pre-burn and post-burn leach solutions were analyzed using gamma ray spectrometry and mass spectrometry. This was accomplished by taking 10-mL aliquots of all of the deconsolidation and leach solutions from the nominal 150 to 200-mL leach volumes. The samples were transferred to the B-wing counting rooms of the Analytical Laboratory in MFC-752 to facilitate gamma spectrometry with less background interference than would be observed in the A-wing Hot Cell 4 spectrometer. In the B-wing, the solutions were counted on Detector B. Detector B, located in Laboratory B-30, is a +3,000-V high purity germanium, coaxial detector connected to a Canberra digital Multi-Channel Analyzer and uses APEX peak analysis software. The detector is located within a steel vault that has walls approximately 25-cm thick to provide shielding. This detector is calibrated for use

with a maximum sample-to-detector distance of 1 meter. Samples are placed on plastic jigs that allow precise placement in relation to the detector. A multi-line gamma source ranging from 59.4 to 1,836 keV was used to calibrate the detector.

To measure the Sr-90 content of the solutions, strontium was separated onto a solid crown-ether ion exchange medium, then eluted from the media and precipitated as a carbonate. A Tennelec gas-flow proportional unit was used to determine the amount of beta activity per mass of precipitate to determine sample Sr-90 content. Mass spectrometric analysis of the DLBL solutions was performed using a VG Plasma Quad inductively-coupled plasma mass spectrometer (ICP-MS).

The measured fission product radioisotope activities were decay-corrected to November 7, 2009, 12:00 GMT, the end of the AGR-1 irradiation (EOI) plus 1 day. Decay corrections were calculated using the equation

$$A = A_0 e^{-\lambda t} \quad (1)$$

where  $A$  is the activity at time  $t$ ,  $A_0$  is the activity at  $t = 0$ , and  $\lambda$  is the decay constant ( $\lambda = \ln(2)/t_{1/2}$ , and  $t_{1/2}$  is the half-life). Isotope half-life data were taken from the ENDF/B-VII.1 library (Chadwick et al. 2011). Values were then compared to the predicted compact inventory at EOI plus 1 day based on ECAR-958, Revision 2 (Sterbentz 2013) to calculate the fraction of the compact inventory. Predicted inventory of key isotopes presented in this report for Compact 5-3-1 are given in Table 2.

Table 2. Predicted inventory of isotopes in AGR-1 Compact 5-3-1 based on physics calculations (Sterbentz 2013).

Isotope	Inventory (Bq) @ EOI + 1 day
Ag-110m	1.91E+08
Ce-144	2.17E+11
Cs-134	2.00E+10
Cs-137	1.74E+10
Eu-154	6.51E+08
Eu-155	4.70E+08
Ru-106	5.26E+10
Sb-125	1.28E+09
Sr-90	1.49E+10
Zr-95	2.58E+11
Isotope	Inventory (g) @ EOI + 1 year
U-234	1.77E-03
U-235	2.99E-02
U-236	2.41E-02
U-238	6.94E-01
Pu-239	8.13E-03
Pu-240	4.37E-03

The inventory of selected fission product radioisotopes in each of the five DLBL solutions is given in Table 3, both as decay-corrected activity and the equivalent Compact 5-3-1 fraction. The inventory of

uranium and plutonium isotopes and fission products determined by ICP-MS are given in Table 4 and Table 5 in absolute measured mass and equivalent compact fraction. No decay correction has been applied to the isotope masses in Table 4 and Table 5 due to the negligible impact on values; however, the values are compared with the predicted compact inventories 1 year after the end of irradiation (November 6, 2010, 12:00 GMT) to account for minor increases in predicted inventory due to decay of parent isotopes.

Note that in Tables 3 through 5, a compact fraction of  $2.41 \times 10^{-4}$  is equivalent to a single particle inventory based on 4,150 particles per compact (Hunn, Montgomery, and Pappano 2006). In cases where the activity or mass was below the detection limit for the method, the detection limit was used to calculate the values in the tables and these values were included in the process totals. If the entries based on detection limits accounted for greater than 50% of the total, then the total was listed as a threshold value (preceded by “<”).

Table 3. Fission products in the deconsolidation and leach solutions from Compact 5-3-1 expressed as decay-corrected activity (Bq) and compact fraction (based on calculated inventories [Sterbentz 2013]).

	Activity (Bq) <sup>a</sup>								
	Ag-110m	Ce-144	Cs-134	Cs-137	Eu-154	Eu-155	Ru-106	Sb-125	Sr-90
Deconsolidation	6.33E+5	<4E+4	8.47E+3	1.91E+4	3.00E+5	2.25E+5	<4E+4	<5E+3	9.76E+5
Pre-burn leach 1	9.84E+4	3.06E+4	1.90E+3	7.79E+3	4.66E+4	4.37E+4	<3E+4	<3E+3	1.51E+5
Pre-burn leach 2	7.48E+3	2.30E+5	1.09E+3	7.71E+3	8.97E+3	8.30E+3	<2E+4	<2E+3	1.44E+4
Post-burn leach 1	9.87E+5	7.35E+7	2.24E+4	3.59E+4	4.06E+5	3.44E+5	<8E+4	1.51E+4	1.71E+6
Post-burn leach 2	8.12E+3	1.90E+5	1.50E+4	4.19E+4	1.00E+3	<1E+3	1.51E+4	<4E+3	4.27E+4
	Compact Fraction <sup>b</sup>								
	Ag-110m	Ce-144	Cs-134	Cs-137	Eu-154	Eu-155	Ru-106	Sb-125	Sr-90
Deconsolidation	3.31E-3	<2E-7	4.24E-7	1.10E-6	4.60E-4	4.79E-4	<8E-7	<4E-6	6.55E-5
Pre-burn leach 1	5.15E-4	1.41E-7	9.51E-8	4.48E-7	7.16E-5	9.30E-5	<5E-7	<3E-6	1.02E-5
Pre-burn leach 2	3.92E-5	1.06E-6	5.48E-8	4.44E-7	1.38E-5	1.77E-5	<3E-7	<2E-6	9.64E-7
Post-burn leach 1	5.17E-3	3.39E-4	1.12E-6	2.06E-6	6.24E-4	7.33E-4	<1E-6	1.18E-5	1.14E-4
Post-burn leach 2	4.25E-5	8.77E-7	7.53E-7	2.41E-6	1.54E-6	<3E-6	2.88E-7	<3E-6	2.87E-6
Process totals	9.07E-3	3.42E-4	2.45E-6	6.46E-6	1.17E-3	1.33E-3	<3E-6	2.32E-5	1.94E-4
Particle equivalent	3.77E+1	1.42E+0	1.02E-2	2.68E-2	4.86E+0	5.51E+0	<1E-2	9.64E-2	8.05E-1
a. Measured activity data taken from AL Report No. 94111 (2014).									
b. Note that a fraction of 2.41E-4 is equivalent to a single particle inventory.									

Uranium inventory in all of the DLBL solutions was very low (Table 4), indicating that no kernels were exposed during any of the leaching steps. This is consistent with data from the AGR-1 irradiation, indicating that there were no particles with failed TRISO layers in Capsule 5 (Collin 2015), as well as the observation that there were no elevated levels of cesium found adjacent to Compact 5-3-1 in the graphite holder from Capsule 5 (Demkowicz et al. 2013) that might indicate particles with failed SiC.

The total Ag-110m inventory found in all of the solutions amounted to a compact fraction of  $9.1 \times 10^{-3}$ , equivalent to the inventory in 38 particles. Total cesium inventory was very low,  $2.4 \times 10^{-6}$  and  $6.5 \times 10^{-6}$  for Cs-134 and Cs-137, respectively. The total inventory of Ce-144, Eu-154, and Eu-155 exceeded the level of a single particle, while the total Sr-90 inventory was just below this level. This indicates release of small quantities of these isotopes through intact SiC coatings. All of these isotopes exhibited relatively large inventory in the first post-burn leach solution. The largest inventory of actinides was also found in this solution. Relatively high isotopic inventory in the first post-burn leach solution has been observed previously (Demkowicz et al. 2012, for example) and is believed to be due to conversion of various carbon-rich phases into more soluble oxides during the burn step and subsequent dissolution in the first post-burn leach.

Table 4. Uranium and plutonium inventory in the deconsolidation and leach solutions from Compact 5-3-1 expressed as total mass ( $\mu\text{g}$ ) and compact fraction (based on calculated inventories [Sterbentz 2013]).

	Mass ( $\mu\text{g}$ ) <sup>a</sup>					
	U-234	U-235	U-236	U-238	Pu-239	Pu-240
Deconsolidation	<2E-2	6.54E-2	4.00E-3	9.12E-1	2.50E-2	<1E-2
Pre-burn leach 1	<2E-2	8.60E-2	3.60E-3	7.34E-1	6.40E-2	<2E-2
Pre-burn leach 2	<5E-2	1.79E-1	1.00E-2	3.49E+0	2.60E-2	<3E-2
Post-burn leach 1	<5E-2	4.96E-1	2.20E-1	8.96E+0	3.67E-1	4.78E-1
Post-burn leach 2	<7E-2	2.13E-1	2.50E-2	2.89E+0	2.10E-2	<4E-2
	Compact Fraction <sup>b</sup>					
	U-234	U-235	U-236	U-238	Pu-239	Pu-240
Deconsolidation	<1E-5	2.19E-6	1.66E-7	1.31E-6	3.08E-6	<2E-6
Pre-burn leach 1	<1E-5	2.87E-6	1.49E-7	1.06E-6	7.87E-6	<3E-6
Pre-burn leach 2	<3E-5	5.98E-6	4.15E-7	5.03E-6	3.20E-6	<7E-6
Post-burn leach 1	<3E-5	1.66E-5	9.13E-6	1.29E-5	4.52E-5	1.09E-4
Post-burn leach 2	<4E-5	7.12E-6	1.04E-6	4.16E-6	2.58E-6	<9E-6
Process totals	<1E-4	3.47E-5	1.09E-5	2.45E-5	6.19E-5	1.31E-4
Particle equivalent	<5E-1	1.44E-1	4.52E-2	1.02E-1	2.57E-1	5.45E-1
a. Measured mass data taken from AL Report No. 94111 (2014).						
b. Note that a fraction of 2.41E-4 is equivalent to a single particle inventory.						

The ICP-MS data for isotopes with mass numbers ranging from 85 to 116 and 128 to 154 were scrutinized for potential interferences when interpreting the data. Mass spectrometry has additional complications compared to gamma spectrometry in this context, including (a) the possibility of mass interferences (e.g., multiple isotopes of the same atomic mass or monoxide species forming in the plasma) and (b) the possibility of contributions from naturally occurring contamination in the samples. The often very small quantities of analytes in the solutions also enhanced the possibility of small amounts of natural contamination significantly affecting the signal. After careful review of the data, it was determined that results for some of the mass numbers exhibited evidence of these issues (e.g., mass ratios for isotopes of a particular element correlating very well with natural isotopic abundances, suggesting trace contamination introduced during sample processing). In some instances, therefore, it was decided that the results were unlikely to represent fission products present in the compact outside of SiC. Table 5 lists the isotopes for which there was reasonable confidence in the values within the limitations discussed below.

Table 5. Inventory of selected fission products determined by ICP-MS analysis of the Compact 5-3-1 DLBL solutions, expressed as total mass ( $\mu\text{g}$ ) and compact fraction (based on calculated inventories [Sterbentz 2013]).

	<b>Mass (<math>\mu\text{g}</math>)<sup>a</sup></b>									
	<b>Pd-105</b>	<b>Ag-109</b>	<b>Cd-111</b>	<b>Cd-112</b>	<b>Cd-114</b>	<b>La-139</b>	<b>Ce-140</b>	<b>Nd-143</b>	<b>Nd-145</b>	<b>Sm-152</b>
Deconsolidation	<7E-2	6.75E-1	8.23E-1	1.57E+0	1.86E+0	1.40E-1	3.30E-1	6.00E-3	6.00E-3	6.92E-2
Pre-burn leach 1	2.00E+0	1.49E-1	2.45E-1	4.85E-1	5.47E-1	1.16E-1	1.49E-1	<1E-2	6.00E-3	2.90E-2
Pre-burn leach 2	4.20E-1	2.00E-2	1.87E-1	3.50E-1	3.89E-1	4.90E-2	8.30E-2	1.20E-2	1.40E-2	1.20E-2
Post-burn leach 1	2.54E+0	1.14E+0	5.92E-1	6.91E-1	7.24E-1	3.45E+0	4.39E+0	2.24E+0	2.52E+0	1.37E+0
Post-burn leach 2	4.60E-1	<5E-2	1.72E-1	3.22E-1	3.67E-1	<9E-2	<2E-1	<2E-2	<2E-2	<2E-2
	<b>Compact Fraction<sup>b</sup></b>									
	<b>Pd-105</b>	<b>Ag-109</b>	<b>Cd-111</b>	<b>Cd-112</b>	<b>Cd-114</b>	<b>La-139</b>	<b>Ce-140</b>	<b>Nd-143</b>	<b>Nd-145</b>	<b>Sm-152</b>
Deconsolidation	<7E-5	3.74E-3	1.41E-2	5.06E-2	4.32E-2	2.46E-5	5.77E-5	1.82E-6	1.88E-6	1.15E-4
Pre-burn leach 1	1.98E-3	8.25E-4	4.21E-3	1.56E-2	1.27E-2	2.03E-5	2.61E-5	<3E-6	1.88E-6	4.82E-5
Pre-burn leach 2	4.16E-4	1.11E-4	3.21E-3	1.13E-2	9.02E-3	8.57E-6	1.45E-5	3.64E-6	4.39E-6	1.99E-5
Post-burn leach 1	2.51E-3	6.31E-3	1.02E-2	2.23E-2	1.68E-2	6.04E-4	7.68E-4	6.80E-4	7.90E-4	2.28E-3
Post-burn leach 2	4.55E-4	<3E-4	2.95E-3	1.04E-2	8.51E-3	<2E-5	<4E-5	<6E-6	<6E-6	<3E-5
Process totals	5.43E-3	1.13E-2	3.47E-2	1.10E-1	9.01E-2	6.73E-4	9.02E-4	6.95E-4	8.05E-4	2.49E-3
Particle equivalent	2.25E+1	4.67E+1	1.44E+2	4.57E+2	3.74E+2	2.79E+0	3.74E+0	2.88E+0	3.34E+0	1.03E+1

a. Measured mass data taken from AL Report No. 94111 (2014).  
b. Note that a fraction of 2.41E-4 is equivalent to a single particle inventory.

The Ag-109 data in Table 5 are in good agreement with Ag-110m data (Table 3). Note that the cumulative compact fraction for Ag-109 is within 25% of the value for Ag-110m. Palladium data are of significant interest due to the behavior of palladium in the particles, in particular the tendency to react with SiC and the observation that palladium can be found inside the SiC microstructure of irradiated particles (e.g., Demkowicz et al. 2016a, van Rooyen et al. 2014). The Pd-105 data in Table 5 suggest that an appreciable amount is released from the intact SiC layers (total compact fraction of  $5.4 \times 10^{-3}$  found in the compact outside of SiC). Note that the fraction for Pd-105 is within approximately a factor of 2 of the values for both silver isotopes. While the cadmium values in Table 5 suggest significant inventory in the compact outside of SiC (ranging from 3.5 to 11% of the compact inventory), the values are suspect, because the mass ratios in this range more closely resemble natural abundance than the predicted ratios expected from fission, and there is a potential source of natural cadmium contamination in the hot cells used to process these specimens. The conclusion is that these values may be heavily influenced by sample contamination and do not accurately represent release of cadmium isotopes through the intact SiC layers.

The Ce-140 value in Table 5 is within less than a factor of three of the Ce-144 value in Table 3. The compact fractions for the lanthanides La-139, Nd-143, and Nd-145 in Table 5 are all similar; they also are in a similar range as the cerium isotopes Ce-140 and Ce-144. Therefore, a tentative conclusion is that these data represent a small but measurable level of release from the particles. The fraction of Sm-152 was relatively high ( $2.5 \times 10^{-3}$ ) and was close to the values observed for Eu-154 and Eu-155.

It is recommended that the use of sample blank solutions be employed during analysis of future DLBL specimens. This would help to more definitively identify contamination from natural sources in the samples and improve the ability to interpret the ICP-MS DLBL results.

### **3. PARTICLE INSPECTION AND GAMMA COUNTING**

#### **3.1 Visual Inspection**

Details about the equipment and procedures for visual particle inspection and gamma spectrometry of individual particles are given in Appendix B. Visual examination of the Compact 5-3-1 particles revealed particles that were uniformly free of surface discolorations or deposits (Figure 5). Some apparent variation in reflectivity exists, but this is an artifact of lighting. Sixty particles were randomly selected using the particle handling system and placed in individual glass vials for gamma spectrometry.

#### **3.2 Particle Gamma Counting**

A total of 60 particles from Compact 5-3-1 were gamma counted following the second post-burn leach. Each particle was counted for either 2 or 4 hours. The gamma counting was performed between November 1, 2011, and March 1, 2012. Details of the gamma counting equipment and procedure are given in Appendix B.

Table 6 provides the decay-corrected activity of each isotope measured in the particles (all activity values are decay corrected to EOI plus 1 day, as discussed in Section 2). Twenty-three of the particles analyzed had Ag-110m activity below detection limits. The detection limit for these particles was used to calculate the decay-corrected activities listed in Table 6 preceded by “<.” These values were used in calculating the average and standard deviation for Ag-110m activity in the table. However, the averages and standard deviations in Table 6 do not include contributions from particles AGR1-531-018 and AGR1-531-046 (discussed below).

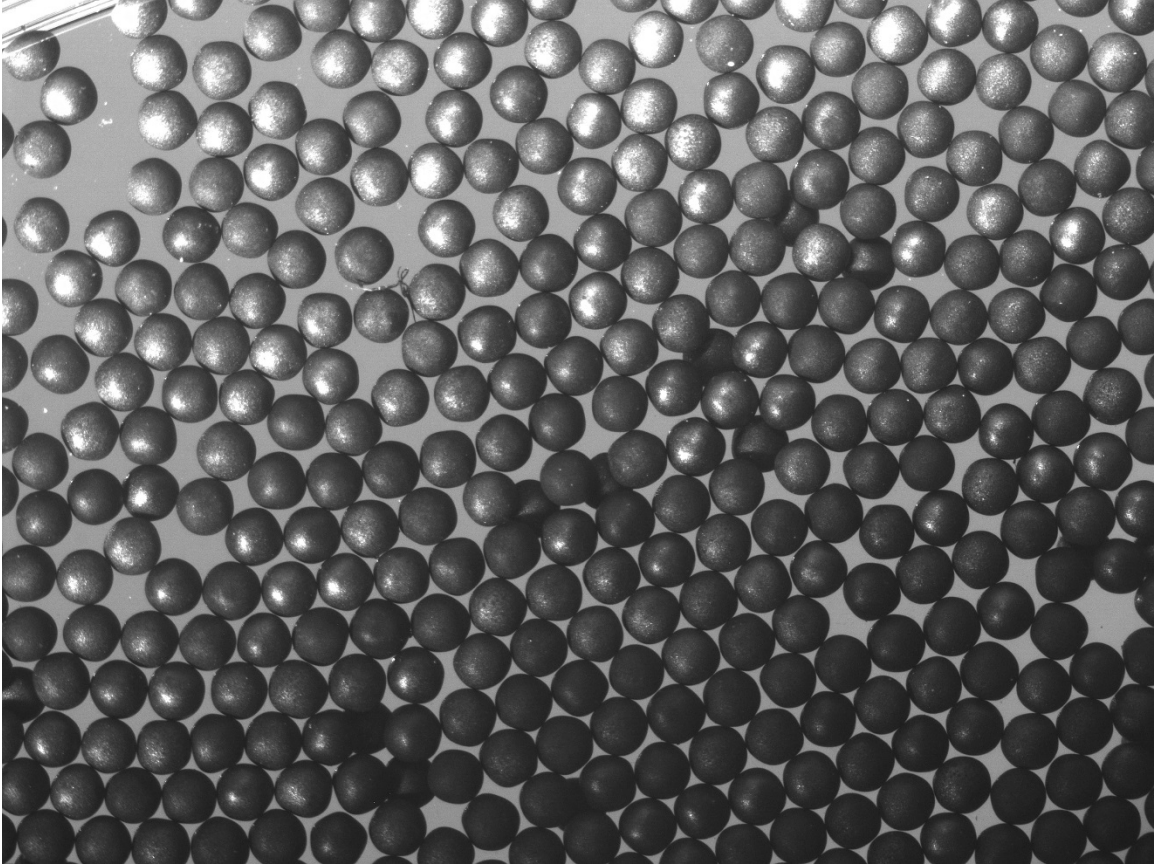


Figure 5. Image of particles from AGR-1 Compact 5-3-1 following burn-leach analysis.

Table 6. Decay-corrected activities (in Bq) for isotopes measured by gamma counting of particles from irradiated Compact 5-3-1.

Particle No.	Activity (Bq) <sup>a</sup>								
	Ag-110m	Ce-144	Cs-134	Cs-137	Eu-154	Eu-155	Ru-106	Sb-125	Zr-95
AGR1-531-01	2.54E+4	4.80E+7	4.24E+6	3.81E+6	1.19E+5	7.41E+4	9.71E+6	1.72E+5	5.92E+7
AGR1-531-02	<1.1E+4	5.07E+7	4.64E+6	4.07E+6	1.27E+5	9.29E+4	1.01E+7	1.99E+5	5.84E+7
AGR1-531-03	<8.3E+3	5.54E+7	4.57E+6	4.22E+6	1.31E+5	7.42E+4	1.07E+7	2.03E+5	6.92E+7
AGR1-531-04	<1.2E+4	5.23E+7	4.66E+6	4.07E+6	1.28E+5	9.15E+4	1.08E+7	1.90E+5	5.95E+7
AGR1-531-05	4.33E+4	4.50E+7	4.57E+6	3.85E+6	1.29E+5	8.45E+4	1.09E+7	1.88E+5	4.81E+7
AGR1-531-06	5.25E+4	5.66E+7	4.94E+6	4.38E+6	1.39E+5	7.47E+4	1.19E+7	2.17E+5	6.89E+7
AGR1-531-07	2.92E+4	4.64E+7	4.19E+6	3.69E+6	1.16E+5	6.97E+4	9.26E+6	1.81E+5	5.14E+7
AGR1-531-08	4.15E+4	5.02E+7	4.61E+6	4.11E+6	1.29E+5	7.52E+4	9.99E+6	1.87E+5	5.97E+7
AGR1-531-09	<1.2E+4	4.97E+7	4.19E+6	3.85E+6	1.16E+5	7.92E+4	9.46E+6	1.97E+5	6.37E+7
AGR1-531-010	<8.8E+3	4.83E+7	4.09E+6	3.74E+6	1.15E+5	5.98E+4	9.03E+6	1.67E+5	5.67E+7
AGR1-531-011	4.01E+4	4.86E+7	4.54E+6	3.99E+6	1.28E+5	6.48E+4	1.01E+7	1.76E+5	5.08E+7
AGR1-531-012	<1.2E+4	4.89E+7	4.14E+6	3.79E+6	1.14E+5	8.97E+4	9.25E+6	1.74E+5	6.32E+7
AGR1-531-013	<1.2E+4	4.88E+7	3.59E+6	3.50E+6	1.07E+5	5.99E+4	9.41E+6	1.64E+5	6.41E+7
AGR1-531-014	1.01E+4	4.79E+7	4.05E+6	3.68E+6	1.15E+5	6.99E+4	9.14E+6	1.83E+5	6.33E+7
AGR1-531-015	8.93E+3	4.42E+7	3.31E+6	3.15E+6	9.56E+4	7.14E+4	8.35E+6	1.51E+5	6.04E+7

Table 6. (continued).

Particle No.	Activity (Bq) <sup>a</sup>								
	Ag-110m	Ce-144	Cs-134	Cs-137	Eu-154	Eu-155	Ru-106	Sb-125	Zr-95
AGR1-531-016	<1.2E+4	5.40E+7	5.14E+6	4.42E+6	1.35E+5	9.74E+4	1.13E+7	2.06E+5	6.23E+7
AGR1-531-017	3.88E+4	4.59E+7	4.59E+6	3.84E+6	1.25E+5	6.99E+4	9.90E+6	1.80E+5	5.34E+7
AGR1-531-018 <sup>b</sup>	5.97E+3	7.04E+6	6.77E+5	9.39E+5	2.01E+4	1.65E+4	1.50E+6	3.10E+4	7.01E+6
AGR1-531-019	<9.0E+3	5.05E+7	4.50E+6	4.00E+6	1.24E+5	7.54E+4	1.02E+7	1.81E+5	6.51E+7
AGR1-531-020	<1.2E+4	4.53E+7	3.95E+6	3.57E+6	1.10E+5	6.50E+4	8.69E+6	1.55E+5	5.78E+7
AGR1-531-021	<1.2E+4	5.23E+7	4.52E+6	4.00E+6	1.27E+5	6.50E+4	1.06E+7	2.01E+5	6.95E+7
AGR1-531-022	4.79E+4	5.02E+7	4.79E+6	4.07E+6	1.34E+5	9.55E+4	1.11E+7	1.98E+5	5.80E+7
AGR1-531-023	3.90E+4	4.50E+7	4.59E+6	3.88E+6	1.25E+5	7.50E+4	9.71E+6	1.77E+5	4.81E+7
AGR1-531-024	3.30E+4	4.87E+7	3.90E+6	3.71E+6	1.11E+5	7.00E+4	9.38E+6	1.73E+5	7.29E+7
AGR1-531-025	<1.5E+4	5.38E+7	5.42E+6	4.54E+6	1.49E+5	9.01E+4	1.16E+7	1.83E+5	5.57E+7
AGR1-531-026	4.26E+4	4.36E+7	4.41E+6	3.75E+6	1.20E+5	7.51E+4	9.47E+6	1.81E+5	4.24E+7
AGR1-531-027	<1.2E+4	4.46E+7	3.40E+6	3.29E+6	9.58E+4	7.06E+4	8.61E+6	1.73E+5	5.62E+7
AGR1-531-028	3.65E+4	4.58E+7	4.43E+6	3.80E+6	1.25E+5	7.01E+4	9.46E+6	1.75E+5	5.36E+7
AGR1-531-029	<1.2E+4	4.41E+7	4.19E+6	3.63E+6	1.15E+5	8.87E+4	8.98E+6	1.72E+5	5.09E+7
AGR1-531-030	4.58E+4	4.77E+7	4.76E+6	4.08E+6	1.32E+5	8.02E+4	1.10E+7	2.00E+5	4.71E+7
AGR1-531-031	4.88E+4	4.70E+7	4.60E+6	3.88E+6	1.29E+5	8.02E+4	1.09E+7	1.78E+5	5.13E+7
AGR1-531-032	<1.2E+4	4.61E+7	3.93E+6	3.63E+6	1.09E+5	6.52E+4	9.10E+6	1.64E+5	5.83E+7
AGR1-531-033	4.58E+4	4.73E+7	4.75E+6	4.00E+6	1.32E+5	7.22E+4	1.01E+7	1.82E+5	5.15E+7
AGR1-531-034	3.37E+4	4.17E+7	3.75E+6	3.37E+6	1.05E+5	8.02E+4	8.72E+6	1.67E+5	4.35E+7
AGR1-531-035	3.06E+4	5.40E+7	4.68E+6	4.27E+6	1.31E+5	7.52E+4	1.08E+7	2.01E+5	7.16E+7
AGR1-531-036	3.64E+4	4.20E+7	4.10E+6	3.54E+6	1.14E+5	8.37E+4	8.89E+6	1.54E+5	4.36E+7
AGR1-531-037	4.58E+4	4.90E+7	4.87E+6	4.15E+6	1.34E+5	8.39E+4	1.04E+7	1.81E+5	4.98E+7
AGR1-531-038	<9.3E+3	5.53E+7	4.23E+6	4.00E+6	1.23E+5	6.03E+4	1.11E+7	1.89E+5	7.02E+7
AGR1-531-039	5.55E+4	5.39E+7	5.48E+6	4.62E+6	1.54E+5	1.07E+5	1.26E+7	2.09E+5	6.51E+7
AGR1-531-040	3.60E+4	4.77E+7	4.34E+6	3.88E+6	1.22E+5	8.36E+4	9.43E+6	1.78E+5	5.03E+7
AGR1-531-041	3.05E+4	4.87E+7	4.11E+6	3.75E+6	1.17E+5	7.19E+4	9.61E+6	1.83E+5	6.14E+7
AGR1-531-042	4.82E+4	4.89E+7	4.78E+6	4.05E+6	1.33E+5	7.70E+4	1.07E+7	1.99E+5	6.23E+7
AGR1-531-043	1.03E+4	5.02E+7	4.27E+6	3.83E+6	1.19E+5	6.73E+4	9.83E+6	1.80E+5	5.76E+7
AGR1-531-044	<1.0E+4	4.66E+7	4.09E+6	3.60E+6	1.14E+5	7.60E+4	9.73E+6	1.67E+5	5.36E+7
AGR1-531-045	<1.0E+4	4.70E+7	4.58E+6	3.89E+6	1.25E+5	8.53E+4	9.82E+6	1.79E+5	5.32E+7
AGR1-531-046 <sup>b</sup>	6.96E+4	5.41E+7	6.61E+6	4.84E+6	1.77E+5	1.30E+5	1.36E+7	2.09E+5	5.59E+7
AGR1-531-047	4.56E+4	4.91E+7	4.88E+6	4.05E+6	1.38E+5	8.54E+4	1.09E+7	1.76E+5	4.52E+7
AGR1-531-048	4.46E+4	5.27E+7	5.00E+6	4.32E+6	1.37E+5	9.05E+4	1.06E+7	1.89E+5	7.20E+7
AGR1-531-049	3.86E+4	4.81E+7	3.98E+6	3.73E+6	1.13E+5	7.36E+4	9.49E+6	1.72E+5	6.22E+7
AGR1-531-050	3.62E+4	4.73E+7	4.57E+6	3.97E+6	1.24E+5	9.58E+4	9.72E+6	1.72E+5	5.51E+7
AGR1-531-051	4.26E+4	4.83E+7	4.44E+6	3.90E+6	1.22E+5	7.94E+4	9.53E+6	1.81E+5	5.99E+7
AGR1-531-052	<1.1E+4	4.60E+7	4.24E+6	3.69E+6	1.16E+5	7.89E+4	9.56E+6	1.75E+5	5.28E+7
AGR1-531-053	3.70E+4	4.73E+7	4.37E+6	3.74E+6	1.21E+5	7.79E+4	9.46E+6	1.74E+5	5.80E+7
AGR1-531-054	3.71E+4	5.26E+7	4.14E+6	3.97E+6	1.21E+5	7.53E+4	1.05E+7	1.99E+5	7.12E+7
AGR1-531-055	7.49E+3	4.75E+7	3.88E+6	3.49E+6	1.09E+5	7.02E+4	9.34E+6	1.76E+5	6.12E+7

Table 6. (continued).

Particle No.	Activity (Bq) <sup>a</sup>								
	Ag-110m	Ce-144	Cs-134	Cs-137	Eu-154	Eu-155	Ru-106	Sb-125	Zr-95
AGR1-531-056	3.75E+4	4.76E+7	4.42E+6	3.81E+6	1.22E+5	8.00E+4	9.61E+6	1.85E+5	5.66E+7
AGR1-531-057	<7.2E+3	5.33E+7	4.31E+6	3.97E+6	1.24E+5	8.72E+4	1.01E+7	1.94E+5	6.70E+7
AGR1-531-058	<1.1E+4	5.04E+7	4.04E+6	3.72E+6	1.16E+5	8.16E+4	9.92E+6	1.74E+5	6.24E+7
AGR1-531-059	<7.2E+3	4.69E+7	3.52E+6	3.40E+6	1.03E+5	7.28E+4	9.15E+6	1.70E+5	5.73E+7
AGR1-531-060	<1.1E+4	4.83E+7	4.03E+6	3.68E+6	1.14E+5	7.24E+4	9.20E+6	1.71E+5	6.18E+7
Average	2.64E+4	4.87E+7	4.37E+6	3.87E+6	1.22E+5	7.77E+4	9.94E+6	1.81E+5	5.82E+7
SD	1.58E+4	3.33E+6	4.43E+5	2.91E+5	1.13E+4	9.93E+3	8.66E+5	1.37E+4	7.68E+6
CV <sup>c</sup>	59.8%	6.8%	10.2%	7.5%	9.2%	12.8%	8.7%	7.6%	13.2%

a. Measured activity taken from AL Report No. 94112 (2013).  
b. Values for particles AGR1-531-018 and AGR1-531-046 are not included in the averages and standard deviations reported in the table.  
c. Coefficient of variation.

Figure 6 shows the distribution of decay-corrected Ce-144 activities of 60 particles from Compact 5-3-1 that have been normalized to the mean. Note that there was one particle with abnormally low Ce-144 activity (AGR1-531-018). A second particle (AGR1-531-046) also exhibited isotope ratios that deviated significantly from the averages (although the Ce-144 activity was relatively close to the mean and, therefore, is not obvious in Figure 6). Table 7 lists the ratio of decay-corrected activities for particles AGR1-531-018 and AGR1-531-046 to the mean value for all particles. While most isotopes in AGR1-531-018 have an activity that is about 15% of the mean, several are notably higher (Ag-110m, Cs-137, and Eu-155). While the higher value for Ag-110m could easily be explained by significant variation in silver retention in the Compact 5-3-1 particles, the reason for the higher value for Cs-137, in particular, is not clear. The results appear to indicate that this particle had an undersized or otherwise abnormal kernel containing significantly less fissile material than normal particles. The particle was mounted separately for cross-sectional analysis and the results are discussed in Section 6.

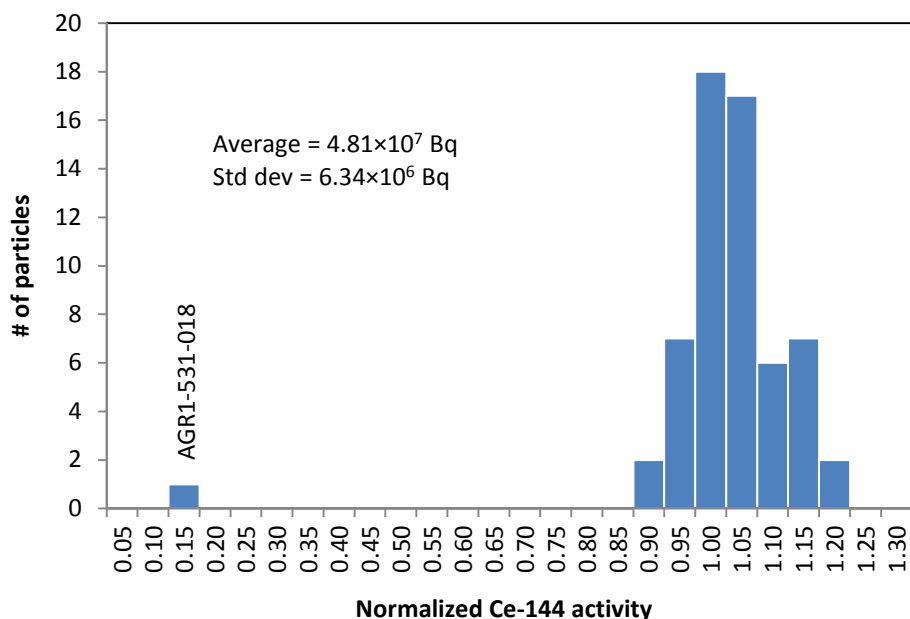


Figure 6. Decay-corrected Ce-144 activity in 60 particles from AGR-1 Compact 5-3-1. Particle AGR1-531-018 had abnormally low Ce-144 activity.

Particle AGR1-531-046 had isotopic activities that were higher than the average, but not in a uniform manner (Table 7). Therefore, it does not appear that this particle simply had a kernel larger than the average. It is notable that the decay-corrected activities for this particle (Table 6) are close to the average decay-corrected particle activities observed in AGR-1 Compacts 4-1-1 (burnup 19.4% FIMA) and 3-2-1 (burnup 19.1% FIMA), both of which were previously processed in a similar manner in the same hot cell (Demkowicz et al 2016a, Demkowicz et al. 2016b). Specifically, the activities for the isotopes Ag-110m, Ce-144, Cs-134, Cs-137, Eu-154, Ru-016, and Sb-125 in AGR1-531-046 were all within 8% of the average activity in particles from compacts 4-1-1 and 3-2-1. It therefore appears possible that AGR1-531-046 could be a particle from one of these compacts that inadvertently cross-contaminated the Compact 5-3-1 particle sample.

Table 7. Ratio of measured isotope activity in particles AGR1-531-018 and AGR1-531-046 to the average activity in all analyzed particles.

Isotope	[Particle activity]/[Avg activity]	
	AGR1-531-018	AGR1-531-046
Ag-110m	0.22	2.60
Ce-144	0.15	1.13
Cs-134	0.16	1.52
Cs-137	0.24	1.26
Eu-154	0.17	1.46
Eu-155	0.21	1.67
Ru-106	0.15	1.38
Sb-125	0.17	1.16
Zr-95	0.12	0.97

For each isotope,  $X$ , the measured inventory in each particle ( $A_i^X$ ) was compared with the value predicted by physics calculations (Sterbentz 2013). The predicted activity in a particle was determined by dividing the predicted activity for Compact 5-3-1 ( $A_{531(calc)}^X$ ) by the average number of particles per AGR-1 Variant 1 compact (4,150). A normalization was then applied to this value to minimize the particle-to-particle variation in starting fissile content (i.e., the result of variation in as-fabricated kernel characteristics such as diameter, density, and stoichiometry) and burnup. For most isotopes, this was accomplished by dividing by the ratio of the measured Cs-137 activity in particle  $i$  ( $A_i^{Cs137}$ ) to the average measured Cs-137 activity for all  $n$  particles measured ( $\sum_{i=1}^n (\frac{1}{n}) A_i^{Cs137}$ ). The result is a ratio of measured-to-calculated (M/C) isotope activity, normalized for variations in fissile content and burnup as shown in *Equation (2)*. In certain instances, this ratio can be used to represent an estimate of the fraction of the original inventory that was retained in the particle. However, it is subject to errors due to biases in the predicted inventory in the compact.

$$\frac{\left[ A_i^X / \left( \frac{A_{531(calc)}^X}{4150} \right) \right]}{A_i^{Cs137} / \sum_{i=1}^n (\frac{1}{n}) A_i^{Cs137}} \quad (2)$$

Cs-137 activity was used to normalize the values because it has a relatively high activity, is readily quantified with low uncertainty, is generated as a linear function of burnup, and is well retained in particles with intact SiC. In the case of Cs-137, Ce-144 activity was used in *Equation (2)* (instead of Cs-137) to normalize the values for variation in fissile content and burnup.

Table 8 lists the average M/C activity ratio for several isotopes in Compact 5-3-1. These are the average of the individual values calculated for each particle, but do not include the contribution from particles AGR1-531-018 and AGR1-531-046. Note that two values are provided for Ag-110m. The first value (“high”) includes the decay-corrected activities based on detection limits in Table 6 when calculating the M/C ratio for each particle and includes these values in the average. The second value (“low”) assumes an activity of zero in all particles with no detectable Ag-110m activity and therefore uses M/C=0 for these particles in determining the average. Thus, these two values will bound the actual average value.

The values in Table 8 are all below 1.0. In the case of Ag-110m, this is likely to be primarily due to a relatively high loss of silver from some particles (discussed further below). For the remaining isotopes, it is unlikely that release from particles can explain the values. The low values for Eu-154, Eu-155, Sb-125, Ru-106, and Zr-95 are commonly observed in gamma-counted particles from other AGR-1 compacts (Demkowicz et al. 2016a, Demkowicz et al. 2016b) and are a consequence of a high bias in the predicted isotopic inventories in Table 2 (Sterbentz 2013). For all isotopes listed in Table 8, the M/C values are somewhat lower than those determined for the intact compact based on data from gamma scanning (Harp 2014). Figure 7 shows the M/C values for the particles compared to those for the intact compact. The reason for the bias toward lower values for the particles is not clear. The compact gamma scanning data include inventory in the particles and outside the particles (i.e., in the compact matrix and OPyC layers), while the particle gamma counting data includes the inventory inside particles only. However, there is insufficient inventory of any of these isotopes in the compact outside of the SiC layers (Table 3) to significantly account for the greater values determined for the compacts.

Table 8. Average M/C activity ratios for 58 gamma-counted particles. Note that the averages do not include the contribution from particles AGR1-531-018 and AGR1-531-046.

<b>Isotope</b>	<b>M/C</b>	<b>SD</b>	<b>CV</b>
Ag-110m (high)	0.56	3.2E-01	57.5%
Ag-110m (low)	0.47	4.2E-01	90.3%
Ce-144	0.94	4.7E-02	5.0%
Cs-134	0.91	3.8E-02	4.2%
Cs-137	0.93	4.6E-02	5.0%
Eu-154	0.78	2.5E-02	3.2%
Eu-155	0.69	7.7E-02	11.1%
Ru-106	0.79	3.1E-02	4.0%
Sb-125	0.59	2.9E-02	4.9%
Zr-95	0.94	1.3E-01	13.4%

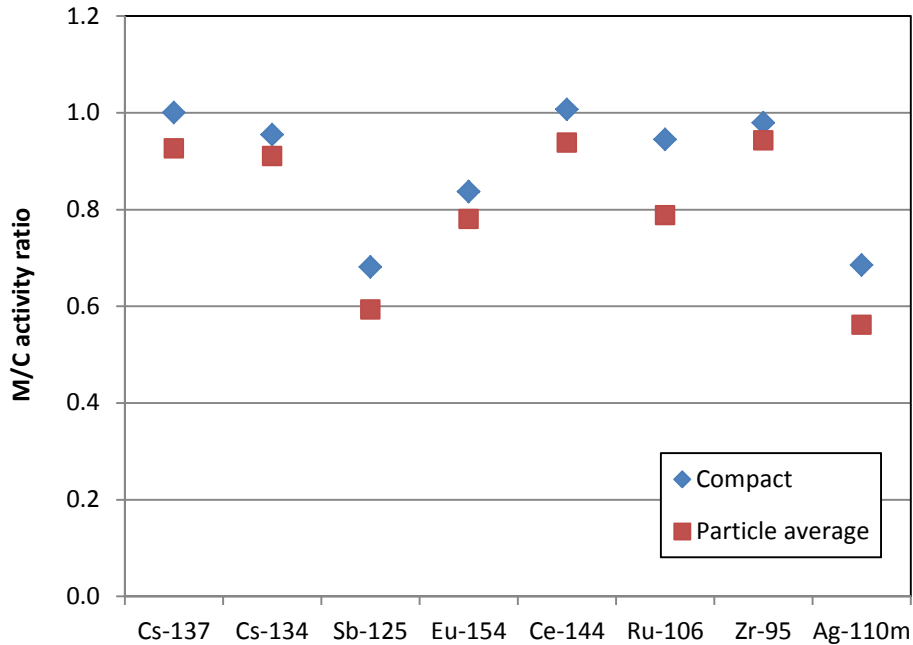


Figure 7. M/C activity ratios for several isotopes determined from gamma scanning intact Compact 5-3-1 (Harp 2014) and from gamma counting individual particles.

The distribution of Ag-110m M/C activity ratios is presented in Figure 8. Of the original 60 particles gamma counted, a total of 23 had no detectable Ag-110m (see Table 6). The reported detection limit was used to calculate the M/C ratio, and these values are plotted in red in Figure 8. These values are considered an upper bound on the actual M/C ratio for these particles. The data exhibit a bimodal distribution, with an upper region between 0.53 and 1.20 (average = 0.85) and a lower region between 0.15 and 0.31 (average = 0.24). (Note that the particle at 1.20 is AGR1-531-046, which had an abnormal distribution of fission products as discussed above.) It is not clear if this behavior is due to variations in temperature among particles, differences in SiC microstructure among particles, or other factors. Several particles were selected for preparation and microanalysis (discussed in Section 6) based on the Ag-110m M/C activity ratio. Particles for which results are presented in Section 6 are labeled in Figure 8, indicating their location in the distribution. One of the objectives of the microanalysis of the particles is to determine if microstructural characteristics are correlated with the silver retention behavior of the particles. Note that one of the particles analyzed microscopically was AGR1-531-018, which was analyzed to better understand the cause of the abnormally low fission product activities in this particle.

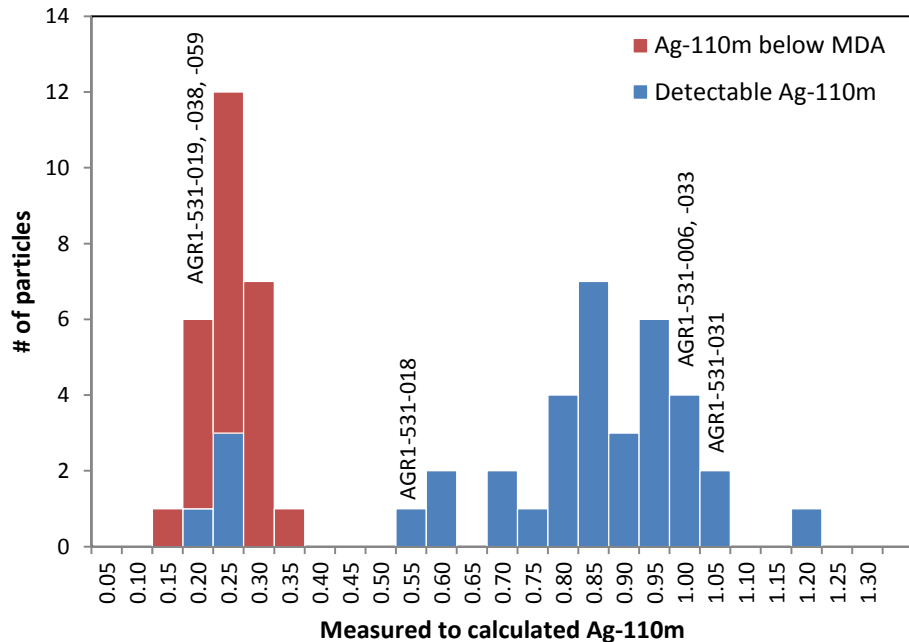


Figure 8. Ag-110m M/C activity ratios for 60 gamma-counted particles from AGR-1 Compact 5-3-1. Red data represents particles for which no Ag-110m was detected; therefore, the minimum detectable activity was used to calculate the M/C ratio. The location of specific particles chosen for mounting and microanalysis are labeled on the distribution.

#### 4. BURNUP ANALYSIS

The burnup of Compact 5-3-1 was determined using ICP-MS measurements. Four sets of 20 burned-back particles were randomly selected. Each set was crushed to expose the fuel kernels, oxidized in air to convert insoluble carbides to soluble oxides, and the residue leached in an acid solution to recover all actinides and fission products present in the kernels. When comparing the amount of plutonium recovered during burnup analysis of particles from AGR-1 Compacts 6-3-2 and 3-2-1 (which occurred prior to 5-3-1 processing) to the expected inventory from physics simulations of the AGR-1 irradiation experiment, the ratio of calculated inventory to the inventory determined experimentally (C/E ratio) was significantly greater than 1, suggesting that either the simulation was over-predicting plutonium in the fuel or the plutonium was not being fully recovered from the crushed particles. To address the possibility of incomplete recovery of plutonium from the particles, one sample of 20 particles from Compact 5-3-1 was processed using the same procedure as the sample from Compact 3-2-1 (oxidation at 750°C, 8M nitric acid dissolution, see Demkowicz et al. 2016b), while the procedure for the remaining three sets of 20 particles was varied slightly by the addition of a small amount of hydrofluoric acid (HF) to the leach solution. These three sets of crushed particles were oxidized in air at 750°C for 24 hours and leached in 8M nitric acid to which three drops of concentrated HF were added. The oxidized kernels and acid solution were kept near boiling for approximately 1 hour. Diluted aliquots of the final leach solution from each of the four samples were analyzed using ICP-MS to determine the mass of actinides and fission products, which were then used to determine the burnup of Compact 5-3-1. The measured burnup values were compared to simulations and burnup values from previous gamma spectrometry measurements.

Burnup is calculated from ICP-MS measurements by using the measured mass of a specific fission product in the fuel, the cumulative fission yield of that specific fission product, and the total mass of actinides present in the sample. Ideally, the fission products used in the calculations should have a small neutron absorption cross section, a high cumulative fission yield, and a similar fission yield for that isobar

(same atomic number) between uranium and plutonium fission. Chemically, the fission product must also readily dissolve during the leaching process. This technique uses the following formula to calculate burnup based on specific fission products detected in the ICP-MS spectrum.

$$BU = \frac{\left( \frac{N_{fp}}{y_{fp}} \right)}{\left( \left( \frac{N_{fp}}{y_{fp}} \right) + N_{Act} \right)} \times 100 \quad (3)$$

In Equation (3),  $BU$  is the burnup,  $N_{fp}$  is number of atoms of a specific fission product  $fp$  measured in the sample,  $y_{fp}$  is the cumulative fission yield of fission product  $fp$  in the studied fuel, and  $N_{Act}$  is the number of atoms of actinides in the sample. For the AGR-1 test, most of the fission occurred in U-235; therefore, it is reasonable to use the U-235 cumulative fission yields for the various fission products. However, detailed simulations of the AGR-1 experiment (Sterbentz 2013) allow for the creation of effective cumulative fission product yields that are a weighted average of the different fission product yields based on the relative amount of fission that occurred in different actinides over the course of the experiment. The correction due to effective fission products can be as much as 5% for some isotopes which is on the order of the uncertainty in the measurements. The effective cumulative fission product yields were used in these calculations.

Six isotopes work reliably well for the ICP-MS technique in the AGR-1 fuel: La-139, Ce-140, Ce-142, Pr-141, Nd-145, and Nd-146. These isotopes occur on the higher-atomic-number peak of the bimodal fission product distribution. The differences between the U-235 yield and Pu-239 yield are fairly small in this region as well. All of these isotopes are nonradioactive and have relatively small neutron absorption cross sections, with the exception of Nd-145. Because of their cross sections, the number of Nd-145 and Nd-146 atoms in the samples and their respective yields are usually summed to determine the cumulative mass at 145 and 146 for the burnup measurement. In this calculation, the burnup measurement was found by taking the average result from Equation (3) for La-139, Ce-140, Ce-142, Pr-141, and the Nd-145/Nd-146 combined result.

Mass spectrometry data were provided in Analytical Laboratory report for Log number 94113 (dated December 6, 2012). Using the approach outlined in the previous paragraphs, the burnup of Compact 5-3-1 was found to be 16.3% FIMA. This is the average of the value determined from the three samples processed using HF addition to the nitric acid leach solution, as described above. This value compares well with both the predicted value of 16.88% FIMA (Sterbentz 2011)<sup>1</sup> and the two values of 15.9% and 16.9% FIMA determined based on gamma scanning of the intact compact (Harp 2014). The estimated relative uncertainty on the burnup value determined by mass spectrometry is 5%, and the uncertainty on the values determined by gamma spectrometry is 3% for the ratio method and 5% for the direct method (details in Harp 2014). Table 9 summarizes the burnup results for Compact 5-3-1 determined from the various methods.

Table 9. Mass spectrometry burnup data compared to other techniques in % FIMA.

Compact	Mass Spectrometry	Gamma Spectrometry Direct	Gamma Spectrometry Ratio	Simulation
5-3-1	16.3(±0.8) %	16.9(±0.8) %	15.9(±0.5) %	16.88%

<sup>1</sup> Note that the AGR-1 physics predictions in ECAR-958 Revision 1 (Sterbentz 2011), instead of Revision 2 (Sterbentz 2013), were used in the burnup comparisons presented in this section and in Harp 2014 and Harp et al. 2014. This is the reason for the discrepancy between the predicted values from simulation in Tables 1 and 9.

It is also constructive for the purposes of evaluating the AGR-1 physics simulations to compare the actinide mass of each isotope measured by ICP-MS to the mass predicted by simulation. The expected masses of 20 TRISO particles for several different actinide isotopes were determined based on Sterbentz (2013) and compared to the ICP-MS results. The predicted mass per kernel was determined by taking the predicted total mass in the compact from Sterbentz (2013) and dividing by the estimated number of particles in the compact (i.e., 4,150). The updated simulations in Sterbentz (2013) versus Sterbentz (2011) are used in this table. The updated simulations were performed in part to better capture Pu production in an effort to improve comparisons between simulations and mass spectrometry. Because the mass of the individual kernels used for the measurement was not known, it was assumed that each particle had average mass. Comparison of the calculated to experimental values for each of the samples is detailed in Table 10. Note that sample 94113-1 is the one processed without the addition of HF to the nitric acid and is not included in the computed average C/E ratio provided in the table. The data indicate that the addition of HF appears to have improved plutonium recovery by approximately 15 to 20% when comparing the amount of recovered plutonium to the expected plutonium content from simulations. The ICP-MS results for the three major uranium isotopes in the fuel agree well with the simulations. However, the addition of HF appears to have increased the inventory of uranium in the samples, as well as plutonium (i.e., the C/E values have decreased with the addition of HF to the leach solution). In previous ICP-MS burnup measurements, uranium content in the solutions agreed well with simulations without the addition of HF. For Pu-239 and Pu-240, there is, on average, an approximately 25 to 30% over prediction of plutonium content in the kernels by the simulations when HF is added to the leach, whereas the over prediction is in the range of 43 to 49% without HF. The C/E values of nearly 1.5 for the plutonium isotopes in sample 94113-1 are similar to the C/E values seen for Compacts 3-2-1 and 6-3-2. In subsequent burnup measurements, it may be desirable to add more HF to the solution to determine if additional plutonium is still not being recovered by the leach. However, the discrepancy may now be due to errors in the simulation.

Table 10. Comparison of measured actinide content to simulation.

<b>Actinide Content (µg/sample)</b>					
	<b>U-235</b>	<b>U-236</b>	<b>U-238</b>	<b>Pu-239</b>	<b>Pu-240</b>
Predicted <sup>a</sup>	144.2	116.1	3345.3	38.0	21.0
94113-1 <sup>b</sup>	111	96.4	2710	25.5	14.7
94113-2	143	113	3240	30.4	17.5
94113-3	129	106	3030	28.1	16.3
94113-4	144	114	3240	29.3	16.7
<b>C/E Values for each Sample</b>					
94113-1 <sup>b</sup>	1.299	1.204	1.234	1.492	1.431
94113-2	1.008	1.027	1.033	1.251	1.202
94113-3	1.118	1.095	1.104	1.354	1.291
94113-4	1.001	1.018	1.033	1.298	1.260
Average <sup>c</sup>	1.04	1.05	1.06	1.30	1.25
a. Sterbentz 2013. b. No HF in final leach solution. c. Average is for samples 9411-2, 9411-3, and 9411-4 only.					

## 5. PARTICLE CRACKING AND GAMMA COUNTING OF KERNELS AND COATINGS

As a test to determine the efficacy of removing irradiated particle coatings and recovering kernels intact, several gamma-counted particles from Compact 5-3-1 were selected for additional processing and examination. Kernels recovered in this manner are intended to be used in heating tests in the Fuel Accident Condition Simulator furnace and may also be used for re-irradiation tests, where kernels will be placed in the neutron radiography reactor at HFEF and irradiated for short durations to generate short-lived I-131 and Xe-133. Subsequent heating tests can then be performed to evaluate iodine and xenon release at elevated temperatures.

### 5.1 Particle Selection and Kernel Recovery, Inspection, and Diameter Measurement

Particles were selected primarily based on their Ag-110m inventory with the objective of obtaining particles that span approximately the entire range of values displayed in Figure 8. Each particle was placed individually into a cylindrical steel cavity, and a steel anvil was dropped to fracture the coating layers. The resulting pieces were then placed on a glass slide and inspected with the particle handling microscope (described in Appendix B) in an attempt to recover both the kernel and the coating fragments. A total of 20 particles were cracked in this manner and 13 particles were processed successfully (i.e., both the intact kernel and the coating fragments were recovered and placed in separate vials). Table 11 lists the particles that were processed successfully, along with the Ag-110m M/C ratios determined previously for the intact particles prior to cracking. Note that for some particles, no Ag-110m activity was detectable; therefore, the minimum detectable activity was used to calculate the M/C ratio, as discussed in Section 3.2 (values preceded by “<” in Table 11).

Table 11. The M/C Ag-110m activity ratio of particles cracked for recovery of the kernels and the estimated diameter of the kernels after removal of the coating layers.

Particle No.	Ag-110m M/C	Diameter (μm)
AGR1-531-01	0.56	398
AGR1-531-02	<0.23	396
AGR1-531-05	0.94	405
AGR1-531-08	0.84	524
AGR1-531-09	0.25	395
AGR1-531-012	<0.26	392
AGR1-531-013	<0.28	371
AGR1-531-016	<0.22	410
AGR1-531-017	0.84	350
AGR1-531-037	0.92	507
AGR1-531-041	0.68	385
AGR1-531-047	0.94	401
AGR1-531-050	0.76	402

Figure 9 shows examples of kernels and coatings fragments generated by this process. Some kernels exhibited noteworthy features, including small pieces of buffer layer still attached (Figure 9[d]) and kernel deformities that appear to be the results of the kernel partially extruding into a crack in the buffer layer (Figure 9[e]), which is a behavior that has been routinely observed previously in cross sections of particles that have cracked buffer layers (Ploger et al. 2012).

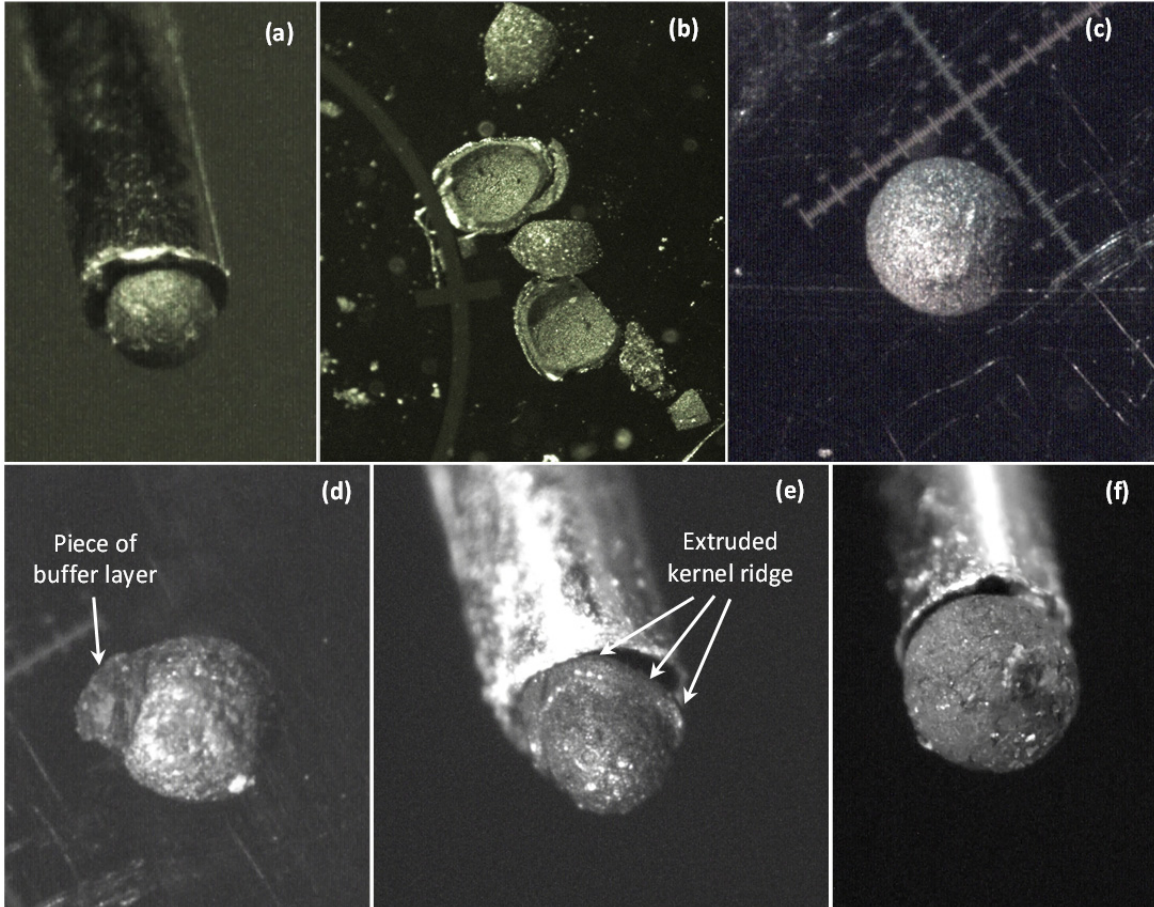


Figure 9. Images of kernels and coating debris recovered after particle cracking. (a) particle AGR1-531-013 kernel, (b) coating fragments, (c) kernel from particle AGR1-531-050 adjacent to graticule markings, (d) kernel from particle AGR1-531-047 showing a piece of adhered buffer layer, (e) kernel from particle AGR1-531-016 exhibiting a ridge of kernel that extruded into a buffer crack during irradiation, and (f) kernel from particle AGR1-531-037 with essentially complete buffer layer still attached.

The kernels were imaged on a glass slide with graticule markings (e.g., Figure 9[c]), and the average diameter was estimated based on the images. The diameters were determined by measuring the length of lines drawn across the particle diameter at different azimuths on a single image and comparing these to the known dimensions indicated by the graticule (individual gradations on the graticule are 10  $\mu\text{m}$ ). Three lines were drawn for each kernel and the average was calculated. In cases where the kernels had obvious pieces of buffer attached, these buffer fragments were avoided when drawing the measurement lines. Image quality and lighting varied to a certain degree; therefore, diameters determined in this manner are considered approximate. The estimated diameters are given in Table 11. Figure 10 shows the distribution of estimated diameters. Note that two particles had values significantly higher than the others (particles AGR1-531-008 and -037). These particles appeared spherical (e.g., Figure 9[f]) but larger in diameter than other kernels.

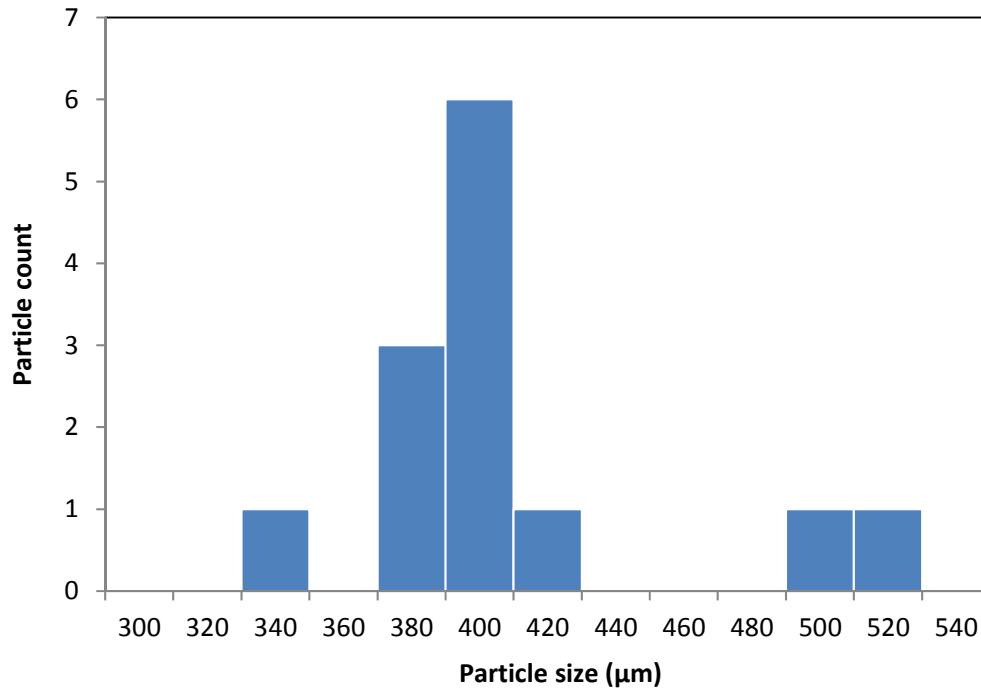


Figure 10. Distribution of estimated kernel diameters based on an analysis of the images. The two particles at the upper end of the distribution are AGR1-531-008 and AGR1-531-037.

Measurements on irradiated kernels and buffer layers have been performed on particles from AGR-1 Compact 1-3-1 (Bower et al. 2016), a Variant 3 fuel compact with similar burnup (16.1% FIMA) to Compact 5-3-1. The mean diameter of kernels was found to be 380 μm (standard deviation = 19 μm). Note that this is larger than the as-fabricated mean of 350 μm due to radiation-induced swelling of the kernel. The mean diameter of buffer layers in “Type A” particles (in which the buffer detached completely from the IPyC layer and densified in continuous contact with the kernel [described in Ploger et al. 2012]) was found to be 513 μm (standard deviation = 15 μm). This value is smaller than the as-fabricated mean of 558 μm due to radiation-induced buffer shrinkage (partially offset by concurrent kernel swelling). Comparing these measurements with the values in Table 11 and Figure 10, it appears that the size distribution of the lower population is consistent with essentially bare kernels—with the exception of obvious adhered buffer fragments, as in particle AGR1-531-047 (Figure 9[d])—and exhibiting a significant distribution in values (likely due to variations in as-fabricated dimensions and irradiation behavior, extruded kernel ridges increasing the measured diameter, and other uncertainties in the post-irradiation diameter measurement). Based on their appearance and estimated diameters, it is concluded that the two particles in the upper distribution have essentially the complete buffer layer still attached to the kernel. This might be expected to result from cracking of a Type A particle. In this report, the portion of the particle containing the kernel is often referred to as the “kernel,” regardless of the amount of buffer still attached.

## 5.2 Kernel and Coating Gamma Counting

The recovered kernels and coating debris were placed in separate glass vials for gamma counting. The vials were gamma counted using the same equipment used for analysis of the intact particles and described in Appendix B.<sup>2</sup> Because of the very low activity expected in the coating debris, count times of 24 hours were used for all of the vials. No Ag-110m was detected in either the kernels or coating debris, because the counting was performed more than 1,800 days after the end of irradiation (7.2 half-lives of Ag-110m, resulting in less than 1% of the inventory from the end of irradiation remaining). The measured activity for each isotope was decay-corrected to EOI plus 1 day (as described in Section 2). For each particle,  $i$ , the decay-corrected values for each isotope,  $X$ , for both the kernel ( $A_{kernel,i}^X$ ) and the coatings ( $A_{coatings,i}^X$ ) were then compared to the value originally determined for the intact particle ( $A_i^X$ ) to determine the fraction of the original particle inventory in the kernel and coatings, as shown in Equations (4) and (5), respectively.

$$\frac{A_{kernel,i}^X}{A_i^X} \quad (4)$$

$$\frac{A_{coatings,i}^X}{A_i^X} \quad (5)$$

Figure 11 shows the fraction of the original inventory in the kernel and coatings for Ce-144, Ru-106, Cs-134, and Eu-154 (Cs-137 data were generally very similar to Cs-134 data). The corresponding data are provided in Table 12. For Ce-144 and Ru-106, the total inventory quantified in the kernels and coatings is very close to the original inventory measured in the intact particles. The total combined inventory in kernels and coatings expressed as a fraction of the original inventory ranges from 1.01 to 1.08 for Ce-144 and 0.99 to 1.05 for Ru-106. For both isotopes, the majority of the inventory is found in the recovered portion containing the kernel (i.e., the fraction of the original inventory found in the recovered coating fragments is 0.01 to 0.07 for Ce-144 and 0.01 to 0.11 for Ru-106). This is not surprising because these elements are expected to exist in relatively stable phases in the kernel, either as the oxide (cerium) or in metallic inclusions (ruthenium). Figure 12 shows that the inventory of these two isotopes in the coatings tends to be correlated (i.e., when Ce-144 inventory in the coating fragments is high, Ru-106 is as well). The two particles with the lowest inventory in the recovered coating fragments are AGR1-531-008 and AGR1-531-037 (approximately 1% of the original inventory of Ce-144 and Ru-106 found in the coating fragments), which are the two particles with intact buffer adhered to the kernels. This may be an indication that the majority of cerium and ruthenium in the recovered coating fragments is in the buffer layer. It also does not preclude the possibility that the recovered coating fragments from the other 11 particles include portions of the “carbide skin” that surrounds the kernels and broke away from the kernel with the buffer layer and that this region contains most of the cerium and ruthenium.

---

2 The equipment was the same, with the exception of the gamma detector. The gamma detector described in Appendix B failed following gamma-counting the intact 5-3-1 particles. A new detector was installed and used for gamma-counting the separated kernels and coating fragments described here. The new detector was a 20% efficient high-purity germanium Ortec Model GEM20PA-70.

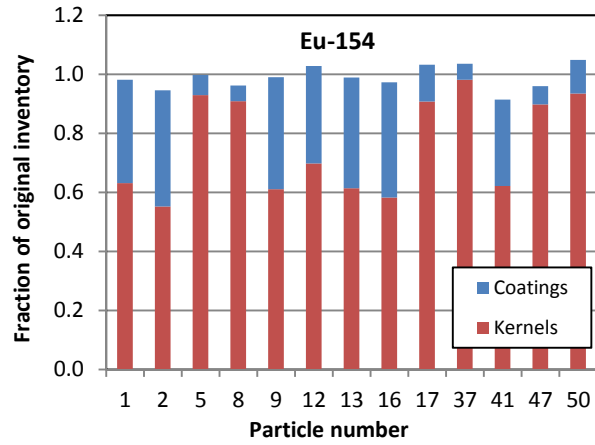
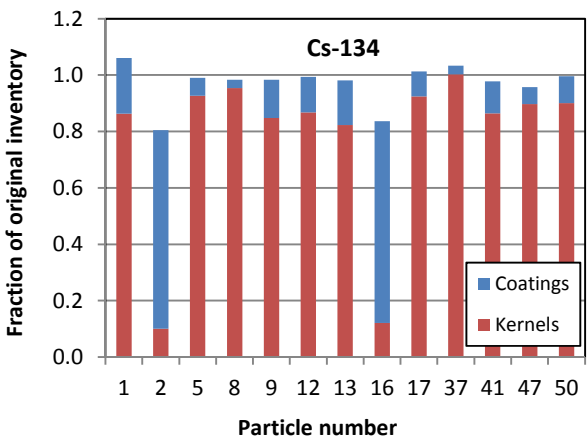
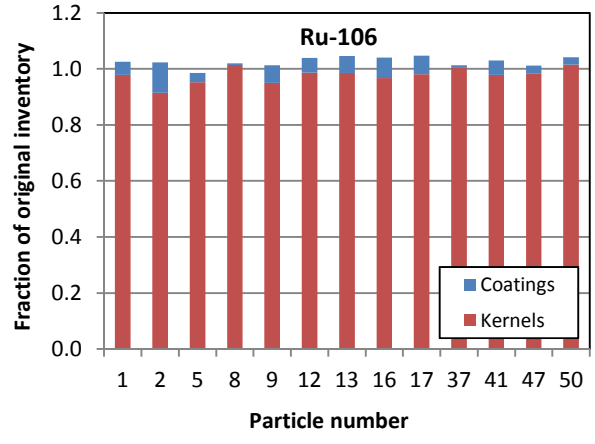
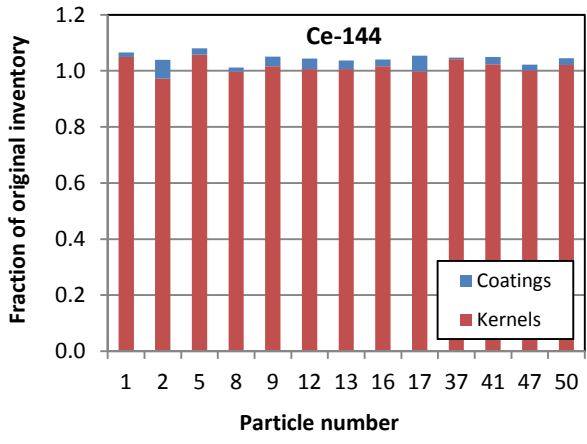


Figure 11. Fraction of original particle inventory that was measured in the kernels and coatings of cracked particles.

Table 12. Fraction of original intact particle inventory in the kernels and coatings and the totals.

Particle No.	Ru-106			Cs-134			Ce-144			Eu-154		
	Kernels	Coatings	Total									
AGR1-531-001	0.98	0.05	1.03	0.86	0.20	1.06	1.05	0.02	1.07	0.63	0.35	0.98
AGR1-531-002	0.92	0.11	1.02	0.10	0.70	0.80	0.97	0.07	1.04	0.55	0.39	0.95
AGR1-531-005	0.95	0.03	0.99	0.93	0.06	0.99	1.06	0.02	1.08	0.93	0.07	1.00
AGR1-531-008	1.01	0.01	1.02	0.95	0.03	0.98	1.00	0.01	1.01	0.91	0.05	0.96
AGR1-531-009	0.95	0.06	1.01	0.85	0.14	0.98	1.02	0.03	1.05	0.61	0.38	0.99
AGR1-531-012	0.99	0.05	1.04	0.87	0.13	0.99	1.01	0.04	1.04	0.70	0.33	1.03
AGR1-531-013	0.99	0.06	1.05	0.82	0.16	0.98	1.01	0.03	1.04	0.61	0.38	0.99
AGR1-531-016	0.97	0.07	1.04	0.12	0.72	0.84	1.02	0.02	1.04	0.58	0.39	0.97
AGR1-531-017	0.98	0.07	1.05	0.92	0.09	1.01	1.00	0.06	1.05	0.91	0.12	1.03
AGR1-531-037	1.01	0.01	1.01	1.00	0.03	1.03	1.04	0.01	1.05	0.98	0.05	1.04
AGR1-531-041	0.98	0.05	1.03	0.86	0.11	0.98	1.02	0.03	1.05	0.62	0.29	0.91
AGR1-531-047	0.98	0.03	1.01	0.90	0.06	0.96	1.00	0.02	1.02	0.90	0.06	0.96
AGR1-531-050	1.02	0.03	1.04	0.90	0.09	1.00	1.02	0.02	1.04	0.94	0.11	1.05
Maximum	1.02	0.11	1.05	1.00	0.72	1.06	1.06	0.07	1.08	0.98	0.39	1.05
Average	0.98	0.05	1.03	0.78	0.19	0.97	1.02	0.03	1.04	0.76	0.23	0.99
Minimum	0.92	0.01	0.99	0.10	0.03	0.80	0.97	0.01	1.01	0.55	0.05	0.91

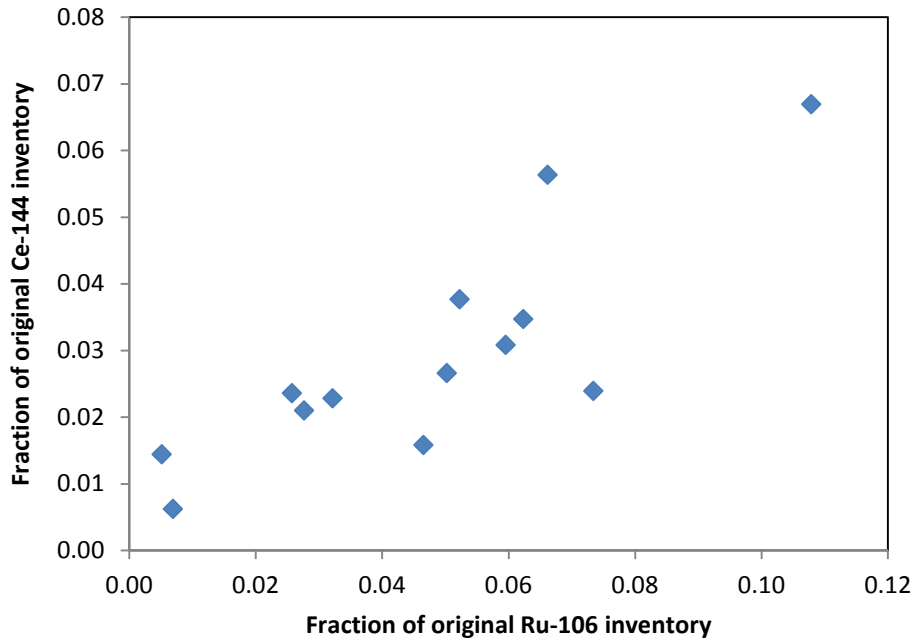


Figure 12. Correlation between the fraction of the original intact particle inventory of Ru-106 and Ce-144 recovered in coating fragments from 13 AGR-1 Compact 5-3-1 particles.

Cs-134 and Eu-154 behavior differed substantially compared to Ce-144 and Ru-106. With the exception of two particles (i.e., AGR1-531-002 and AGR1-531-016), the total inventory of Cs-134 found in the recovered kernels and coating fragments averaged 1.00 (Figure 11, Table 12). However, a larger percentage of the inventory was located in the coating fragments compared to Ce-144 and Ru-106; for these 11 particles, the average fraction in the recovered coating fragments was 0.10 and the average fraction in the kernels was 0.90. Particles AGR1-531-002 and AGR1-531-016 deserve special consideration because they contained very low inventory in the recovered kernels (0.10 and 0.12, respectively) and relatively larger inventory in the coating fragments (0.70 and 0.72, respectively). Based on visual inspection of the recovered kernels, there were no obvious features that distinguished them from the other kernels. Both were roughly spherical (without significant portions obviously missing), and their estimated diameters (Table 11) were close to the average for the lower population in Figure 10. Figure 13 shows images of both kernels. AGR1-531-002 had a relatively rough surface, and AGR1-531-016 exhibited evidence of the kernel having extruded into a fracture in the buffer layer during irradiation. However, in spite of the low Cs-134 inventory in the recovered kernels from these two particles, the Ce-144 and Ru-106 inventory in the kernels was still relatively high (Table 12 and Figure 11), supporting the observation that no significant portions of the kernels were missing.

It is not known from the available data where the cesium specifically resided in the recovered coating fragments. However, it is worth noting that the two particles with the lowest Cs-134 inventory in the recovered coating fragments are AGR1-531-008 and AGR1-531-037 (i.e., the two with an intact buffer surrounding the kernel), which also had the lowest inventory of Ce-144 and Ru-106 in the coating fragments.

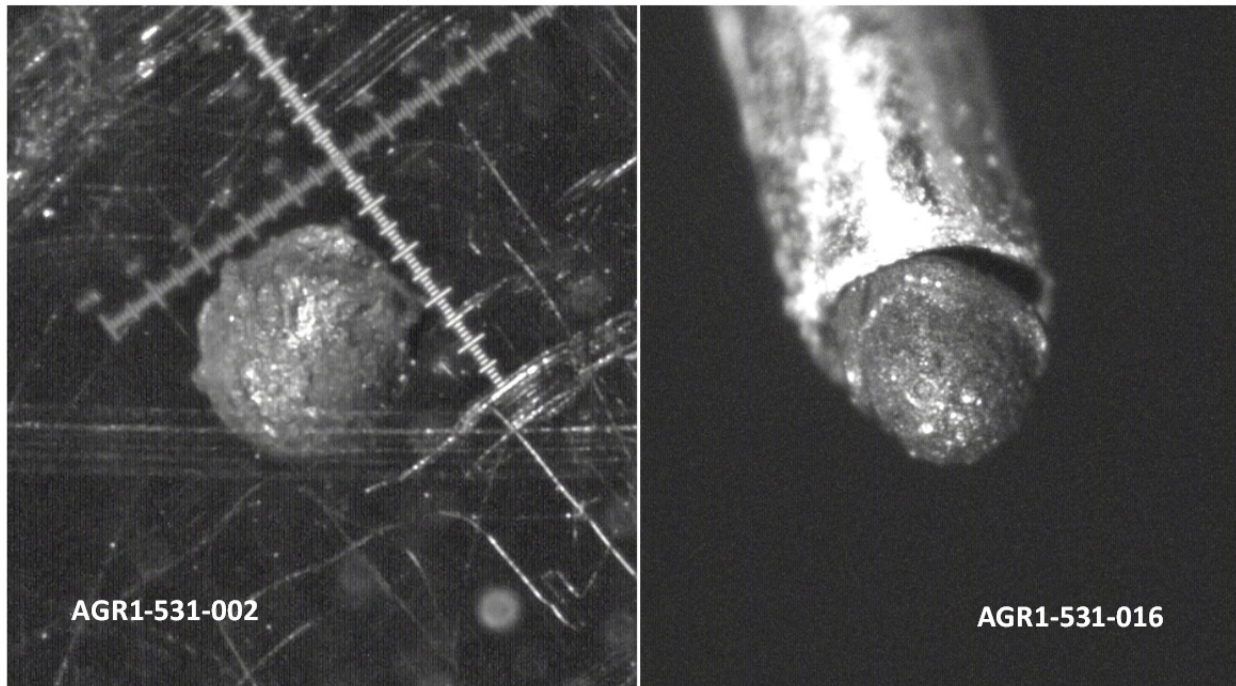


Figure 13. Images of the kernels from particles AGR1-531-002 and AGR1-531-016.

Eu-154 was generally well accounted for in the kernels and coating fragments; the total fraction of the original particle Eu-154 inventory was 0.91 to 1.05 for all particles (Table 12). However, the average fraction of the total inventory found in the coating fragments (0.23) was higher for Eu-154 than for any of the other isotopes. As with the other isotopes in this study, the particles with the lowest fraction found in the recovered coating fragments were AGR1-531-008 and AGR1-531-037. This suggests that a significant fraction of the europium in the coating fragments resided in the buffer layer. The distribution of Eu-154 between the recovered kernels and coating fragments is bimodal in nature. Figure 14 shows the fraction of the original particle inventory that was found in the kernels vs. the estimated kernel diameters. The upper population has an average value of 0.93 (std. dev. = 0.03) and the lower population has an average value of 0.62 (std. dev. = 0.05). Note that the two kernels with larger diameters (due to the intact buffer attached to the kernel) are in the upper population; aside from these two particles, there does not appear to be a diameter dependence for the fraction of Eu-154 in the kernel. Visual inspection of the recovered kernels did not reveal any obvious features to distinguish the kernels in the upper distribution from those in the lower distribution (with the exception of the two particles with an intact buffer attached). The two particles with very low retention of cesium in the kernels (AGR1-531-002 and AGR1-531-016) also had the lowest fraction of Eu-154 in the kernels.

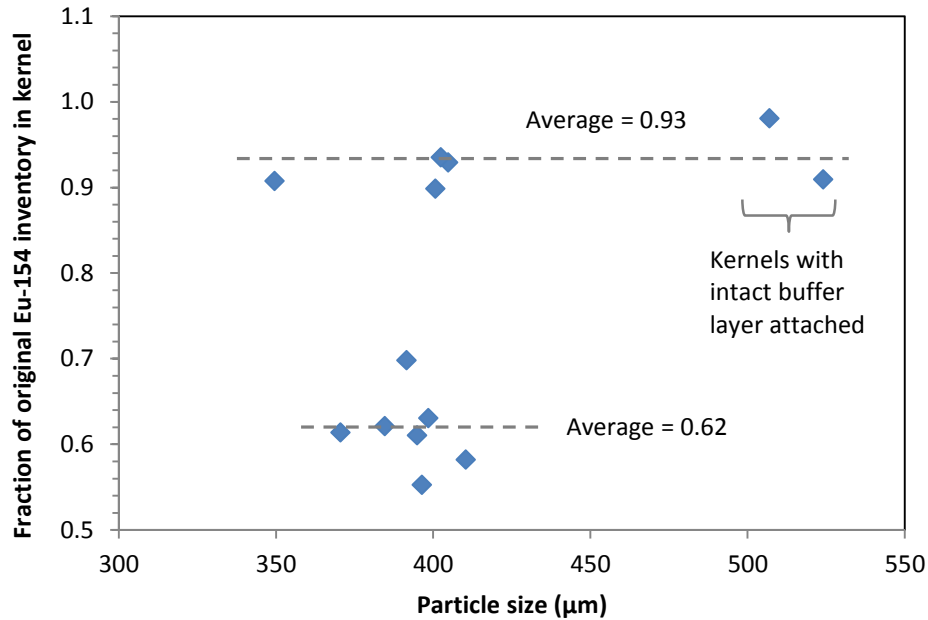


Figure 14. The fraction of the original Eu-154 inventory in each particle that was found in the recovered kernel vs. the estimated particle size of the recovered kernel.

The distribution of Cs-134 and Eu-154 between the recovered kernel and coating fragments was compared to the original measured inventory of Ag-110m in the intact particles. Figure 15 shows the fraction of the original intact particle Cs-134 and Eu-154 inventory that was found in the recovered kernels vs. the Ag-110m M/C ratio for the intact particles. The following observations can be made:

- The particles with the highest inventory of Eu-154 in the recovered kernels (i.e., the upper distribution discussed in connection with Figure 14) had the highest M/C Ag-110m inventories. However, it is not clear if this indicates that the europium behavior is related to temperature (i.e., the higher apparent silver release from some particles was due to higher temperatures and, therefore, the higher apparent release of europium from the kernels is likewise due to higher temperatures) or if it is influenced by differences in particle microstructure that also influence Ag-110m behavior.
- There is generally no significant correlation between the intact particle Ag-110m M/C ratio and the fraction of Cs-134 retained in the kernel. However, it is noteworthy that the two particles that exhibited very low cesium retention in the kernels also had very low silver retention in the particles; nonetheless, other particles with roughly the same Ag-110m M/C ratio for the intact particles had a much higher fraction of Cs-134 in the kernels.

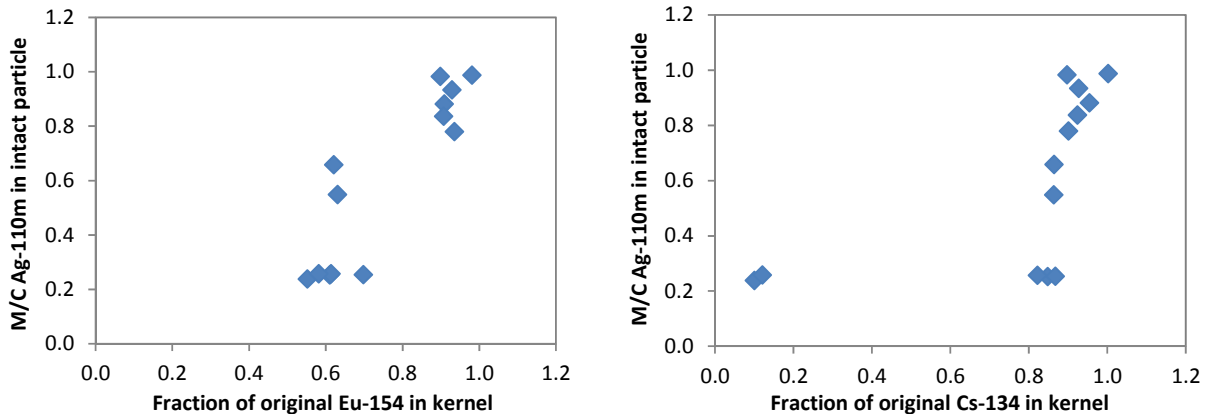


Figure 15. The relationship between the Ag-110m M/C activity ratio in the intact particles and the fraction of the original intact particle inventory of Eu-154 (left), and Cs-134 (right) that was found in the recovered kernels.

### 5.3 Kernel and Coating Analysis Conclusions

Some of the major conclusions from this focused study are as follows:

- The fission product inventory in the intact particles was generally well accounted for in all of the kernels and coating fragments recovered after fracturing.
- Cerium and ruthenium reside mostly in the kernels and most of the inventory found in the coatings may, in fact, be concentrated in the buffer layer or possibly in an outer kernel carbide skin that broke off and stayed with the buffer. This is not surprising given the expected stability of these elements because of the oxide (cerium) or metallic inclusions (ruthenium) in fuel kernels.
- In contrast, cesium exhibited widely varied behavior. Two particles had very little Cs-134 in the kernels, with most of the inventory found in the coatings. The reason for the different behavior in these two particles is not clear, but it seems to point to significant differences in the retentive ability from kernel to kernel due to as-yet unknown factors. The remaining particles exhibited a larger fraction of Cs-134 inventory in the coatings than observed with Ce-144 and Ru-106 (i.e., an average of 10% of the original intact particle inventory), with evidence to suggest that most of this may be located in the buffer.
- The fraction of Eu-154 remaining in the recovered kernels exhibited a bimodal distribution; all of the kernels in the upper distribution also had the highest level of silver retention in the intact particles in the population analyzed. This may point to an effect of temperature on europium retention in the kernels.

The method of recovering loose kernels (with or without intact buffer attached) was successful, with a recovery rate of approximately 65% of particles processed. The kernels generated in this study will be used in heating tests to measure fission product release at elevated temperatures. Gamma counting of the kernels after heating will allow the total inventory of fission products released to be quantified and help in refining the collection efficiency of the condensation plates in the Fuel Accident Condition Simulator furnace. In addition, particles generated in this manner (either from AGR-1 compacts or from AGR-2 or AGR-3/4 compacts) will be used in re-irradiation studies to measure the release of iodine and xenon from the fuel.

Additional recommendations for future analysis of this nature include the following:

- The study should be repeated with freshly-irradiated fuel (i.e., the analysis should be performed closer to the end of irradiation) to observe Ag-110m in the recovered kernels and coating fragments for comparison with the inventory measured in the intact particles.
- Follow-on microanalysis of the kernels of various particles based on their observed behavior (e.g., the level of cesium or europium retention in the kernels) would be of great interest in order to determine if observable differences in microstructure could be correlated with the fission product behavior.
- Burn-leach analysis of the coating fragments could be performed to recover the intact SiC layers and to determine the inventory encapsulated in this layer compared to the inventory in the carbon layers. A similar analysis was performed on coating fragments from AGR-1 Compact 4-1-1 particles (Demkowicz et al. 2016a). In that instance, approximately 15% of the predicted Ag-110m inventory and 1% of the Ru-106 inventory was determined to be residing in the SiC layer of several particles.
- Non-destructive analysis of particles (using x-ray imaging and tomographic reconstruction) prior to selecting them for this analysis would allow specific features to be targeted. For example, particles with their buffer layers completely detached from the IPyC could be selected to increase the likelihood of recovering buffer-encased kernels (similar to AGR1-531-008 and AGR1-531-037).

## **6. PARTICLE MOUNT PREPARATION AND CERAMOGRAPHY**

Deconsolidated, burned-back particles from Compact 5-3-1 were loaded into 10 cylindrical mounts and encapsulated with Buehler EpoHeat epoxy at the MFC Analytical Laboratory. These mounts are listed in Table 13, along with details on both particles (including identifiers when gamma-counted) and mount characteristics. All mounts were pneumatically transferred to HFEF for surface preparation and ceramography. Except for Mount U4, all mounts were intended as candidates for additional studies at the MFC Electron Microscopy Laboratory (EML) if successfully prepared and if warranted by particle features. Mounts U5 and U6 (three particles each) were not prepared because of concerns over potential radiation doses during handling at EML.

### **6.1 Single Particle Mounts**

The design used for Mounts 19U through 25U is shown in Figure 16. Each particle was loaded through a narrow funnel. A thick, double-sided adhesive tape (backed by a glass slide) was used to hold the particle in place while Buehler EpoHeat two-part epoxy was poured into the mount. The epoxy was cured in a furnace for 90 minutes at 55°C. An annular groove in the lower interior of the mount prevented the epoxy from sliding inside the steel during handling and grinding. In combination with the glass-backed tape, the annular groove also encouraged most of the epoxy meniscus—caused from shrinkage of the epoxy during curing—to form at the mount top. Nevertheless, the epoxy still receded slightly inward at the mount base during curing, pulling the particle inward in the process. A circular recess in the mount base limited the amount of steel that had to be ground off while approaching the particle midplane.

Table 13. Compact 5-3-1 particle mounts.

Mount ID	Particle Numbers	Mount Design	Primary Purpose	Status
U4	Not gamma counted	32-mm OD Micarta with annular ID groove	Multi-level optical characterization of TRISO layer behavior on 99 random particles	Examined at nine levels for internal particle morphology
U5	3 (Ag-110m M/C <0.16) 55 (Ag-110m M/C = 0.18) 57 (Ag-110m M/C <0.15)	25-mm OD stainless steel with annular ID groove	Microstructural influences on fission product behavior	Not prepared, in storage
U6	30 (Ag-110m M/C = 0.94) 39 (Ag-110m M/C = 1.00) 42 (Ag-110m M/C = 0.99)	25-mm OD stainless steel with annular ID groove	Microstructural influences on fission product behavior	Not prepared, in storage
19U	59 (Ag-110m M/C <0.18)	25-mm OD stainless steel with annular ID groove	Microstructural influences on fission product behavior	Ceramography complete, in storage
20U	38 (Ag-110m M/C < 0.19)	25-mm OD stainless steel with annular ID groove	Microstructural influences on fission product behavior	Ceramography complete, transferred to EML
21U	19 (Ag-110m M/C <0.19)	25-mm OD stainless steel with annular ID groove	Microstructural influences on fission product behavior	Ceramography complete, in storage
22U	6 (Ag-110m M/C = 1.00)	25-mm OD stainless steel with annular ID groove	Microstructural influences on fission product behavior	Ceramography complete, transferred to EML
23U	31 (Ag-110m M/C = 1.05)	25-mm OD stainless steel with annular ID groove	Microstructural influences on fission product behavior	Ceramography complete, transferred to EML
24U	33 (Ag-110m M/C = 0.95)	25-mm OD stainless steel with annular ID groove	Microstructural influences on fission product behavior	Ceramography complete, transferred to EML
25U	18 (Abnormally low fission product inventory)	25-mm OD stainless steel with annular ID groove	Study kernel size and microstructure for insight on low inventory of all fission products	Ceramography complete, in storage

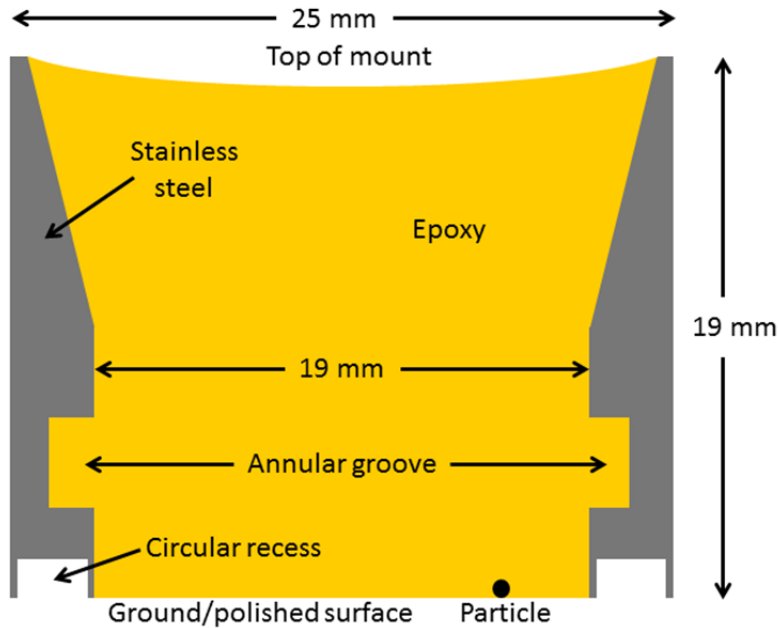


Figure 16. Cross-sectional diagram through center of a Compact 5-3-1 single particle mount.

The glass slide and tape were left in place for pneumatic transfer to HFEF. After more than a year in storage due to a facility shutdown, the glass and tape were remotely pried off the mounts with a putty knife at the HFEF containment box. Coarse grinding was conducted with a Struers MD-Piano 600-grit diamond disc until each particle was contacted. At this point, each mount thickness was measured at its center with a new gauge (see Figure 17). These reference thicknesses were compared to additional measurements made as coarse grinding continued to roughly estimate how much of each particle had been ground away (complementing periscope inspections of exposed layers). This was not exact because the mounts did not always grind evenly, evidently because the grinding force delivered by a pneumatic ram to the upper epoxy meniscus (often more asymmetric than indicated in Figure 16) could be biased toward one side despite a flexible, pivoting “foot.” Consequently, the thickness at the particle location could be different than that measured at the mount center. Furthermore, actual proximity to the midplane depended on the sizes of individual particles, but comparisons could only be made to the nominal as-fabricated SiC radius. Attempts were made to take silhouette images of each particle on the HFEF metallograph for comparisons to the SiC radius at the ground plane for calculating more accurate distances to midplane. Unfortunately, considerable browning of adjacent epoxy by beta radiation occurred during the extended storage period, and the blurry halo of epoxy damage typically prevented discerning the actual silhouettes (excepting on Mount 25U as discussed in Section 6.1.7).

All mounts were incrementally impregnated with epoxy under vacuum (back-potted) to stabilize internal particle structures. The initial back-pot was done shortly after coarse grinding through the SiC and IPyC layers, which opened radial gaps between the IPyC and buffer layers for epoxy penetration. A second back-pot was normally performed after grinding into the kernels to fill any buffer-kernel gaps and to further stabilize kernels. A foam-tipped swab was used to smooth eyedropper-applied back-potting epoxy in advance of vacuum impregnation, which reduced the thickness of surplus epoxy that had to be ground off before continuing to abrade the mount surface.

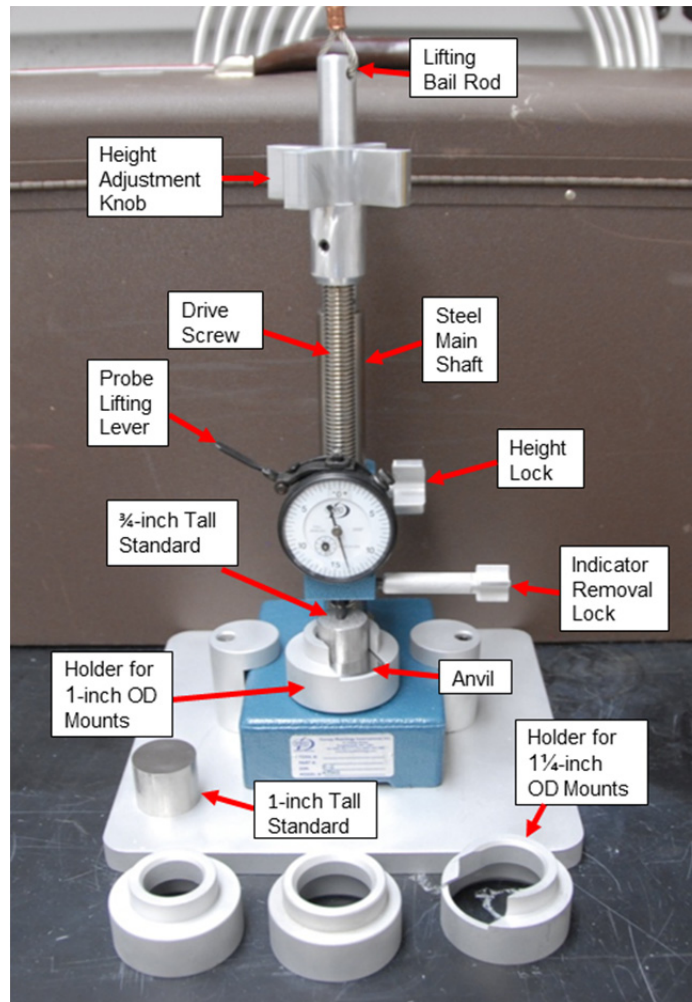


Figure 17. Dial indicator-based mount thickness gauge with standards and mount centering holders.

Coarse grinding continued on all mounts (except Mount 22U, which is discussed in Section 6.1.4) until nearly half of each particle had been ground away. Fine grinding was then performed with an MD-Piano 1200-grit diamond disc, but periscope observations often revealed unusually deep scratches in the epoxy. A metallograph check detected numerous metallic fragments embedded in the epoxy, along with thin strips of stainless steel that were tearing off the outer rim and collecting in the circular recess. This difficulty was overcome by back-potting the recess in each mount, followed by additional 1200-grit grinding. Metal fragments loosened by the grinding were removed from the disc by “dressing” it with a new, soft, fine-grained cleaning tool supplied by Struers with recently available 2000- and 4000-grit discs. This tool was found to be very effective at removing coarse ceramic debris (e.g., kernel fragments and SiC shards) from 600- and 1200-grit discs, which greatly extended their service lives. Until these soft cleaning tools became available, contaminated discs had to be discarded immediately to prevent damaging the mounts.

A 2000-grit disc was used briefly on Mounts 21U and 24U in an attempt to improve SiC layer flatness in the hope that force and time could be reduced for the subsequent polish with a 3- $\mu\text{m}$  diamond suspension. Even with a relatively hard, stiff MD-Dur polishing pad, the traditional 3- $\mu\text{m}$  polish typically produces some rounding of the SiC exterior, as well as considerable relief of the soft IPyC and buffer layers. However, no noticeable improvement was found in the roughness of their SiC layers during a metallograph inspection, although buffer and IPyC layers were slightly smoother. Both of these mounts later needed as much force (40 N) and time (12 minutes) for the 3- $\mu\text{m}$  polish as the mounts finely ground with only a 1200-grit disc. All of the Compact 5-3-1 single particle mounts were then polished with an MD-Nap pad and 1- $\mu\text{m}$  diamond suspension (6 minutes at 20 N), and all but Mount 25U were finished with an MD-Chem pad and 0.04- $\mu\text{m}$  colloidal silica suspension (6 minutes at 20 N).

Ceramographic investigations were aimed at conspicuous behavior of TRISO layers during irradiation. These studies were conducted on a Leitz metallograph using a variable resolution Jenoptik ProgRes C14+ camera. Highlights are presented in the following subsections. Particles are classified according to an internal morphology scheme (see Appendix C) developed for analyzing fuel particles exposed in cross-sectioned AGR-1 fuel compacts (Ploger et al. 2012). Type A particles exhibit a continuous gap between the buffer and IPyC layers in the plane of polish, Type B particles show bonding between the buffer and IPyC layers along the entire interface, and Type AB particles display partial debonding between these layers. These three basic particle types are subdivided according to whether the buffer remained intact or fractured. Figure C-1 presents representative examples of all six characteristic morphologies.

### **6.1.1 Particle AGR1-531-059 (Mount 19U)**

Particle AGR1-531-059 (relatively low Ag-110m M/C ratio) was ground within approximately 53  $\mu\text{m}$  of its SiC midplane, based on a trigonometric comparison of its measured radius in the polished plane (357  $\mu\text{m}$ ) to the computed average as-fabricated SiC radius for Variant 1 AGR-1 fuel of 361  $\mu\text{m}$  (Maki 2009). However, consideration of the substantial variability in as-fabricated particle sizes indicates that this value could be in error by as much as 60  $\mu\text{m}$ . As mentioned previously, measuring the actual particle radius is essential to an accurate determination of midplane proximity. Unfortunately, as suggested by the left image in Figure 18, the particle silhouette (no more than 15  $\mu\text{m}$  outside the SiC exterior) was completely obscured within the thick region of epoxy blackened by beta radiation. Radial features in the epoxy beyond this region likely resulted from embrittlement.

In the context of Appendix C, particle AGR1-531-059 is classified as Type Ai. Nevertheless, the kernel and buffer in the left portion of Figure 18 are biased toward the lower side of the IPyC and SiC layers. This lack of concentricity infers that there may be residual buffer-IPyC bonding on the lower side beyond the plane of polish. Another noteworthy aspect of Figure 18 is the irregular separation between the kernel and buffer. Irradiated AGR-1 particle cross sections generally show a demarcation between the kernel and a thin, low porosity layer on the inside of the buffer. This reaction layer may be related to the uranium carbide “skin” that forms between the kernel and buffer during particle fabrication (Hunn et al. 2005). Less often, but not infrequently, this reaction layer adheres to the kernel, and a distinct boundary may be observed between the porous buffer and this relatively dense layer. These slight separations may occur during grinding as the hard kernel attempts to rotate within the buffer, which is held along its exterior by back-potted epoxy. In Figure 18, however, the separation is very inconsistent, occasionally exhibiting aspects of both modes but more often occurring inside the kernel. Kernel fractures are atypical and may not be artifacts of sample preparation, as discussed in Section 6.1.3.

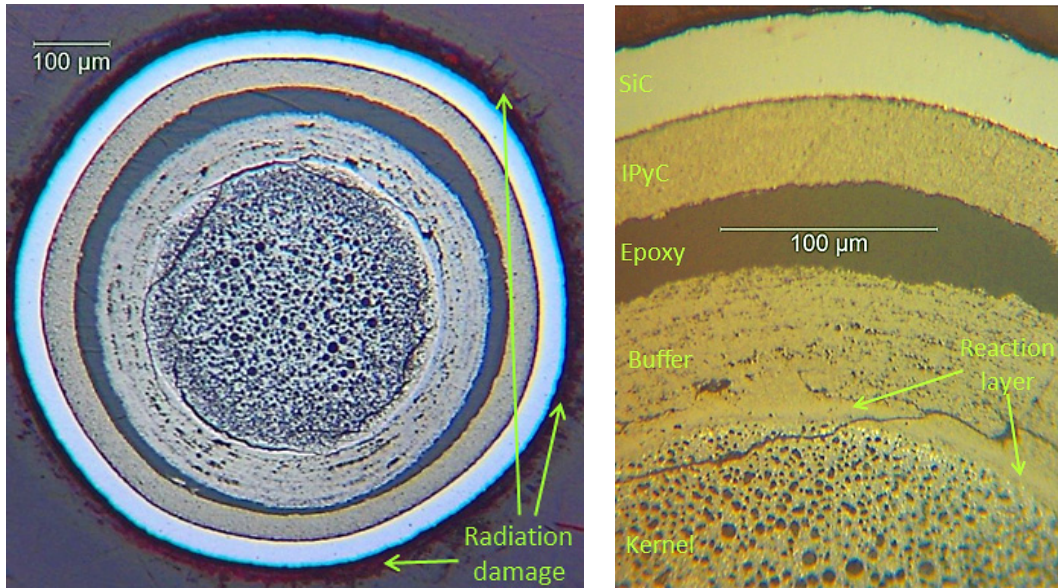


Figure 18. Beta-browned epoxy surrounding particle AGR1-531-059 (left) and irregular separation near its kernel-buffer interface (right).

### 6.1.2 Particle AGR1-531-038 (Mount 20U)

Type ABf particle AGR1-531-038 (relatively low Ag-110m M/C ratio) was ground within approximately 92  $\mu\text{m}$  of its SiC midplane (in the absence of a silhouette, this is calculated using the average as-fabricated size of a burned-back AGR-1 Variant 1 particle). Grinding was deliberately halted before reaching midplane on this particle to preserve features of interest. As displayed in Figure 19, the kernel protruded into cavities where the buffer split. The buffer fracture on the right side evidently happened first, allowing more kernel expansion there than on the lower-left side. Only remnants of the reaction layer can be found around the original kernel in Figure 19. The substantial gaps between these remnants probably represent portions of the layer that broke out during grinding, often leaving voids in their places (darker than back-potted epoxy). If so, this would indicate that the reaction layer is more brittle than the buffer. This grinding-induced breakout may have been aggravated by both stainless steel fragments and small shards of SiC that apparently were knocked loose from the SiC exterior by the steel fragments. Note that the SiC exterior in Figure 19 is substantially rougher than in Figure 18.

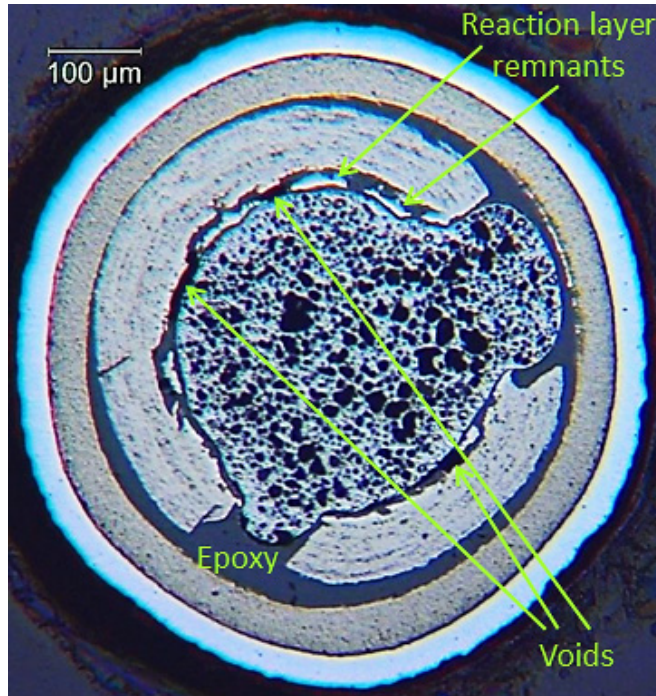


Figure 19. Kernel protrusions into fractured buffer cavities in particle AGR1-531-038.

An anomalous region can be seen along the inner IPyC layer near the large kernel protrusion in Figure 19. Although initially suspected of being a reaction layer formed by close proximity to the kernel protrusion, a higher magnification view on the right side of Figure 20 indicates that it is a thin strip of adherent buffer that peeled off the buffer exterior during debonding. Its appearance is slightly different than similar strips of buffer elsewhere along the IPyC interior in particle AGR1-531-038 (e.g., in the left side of Figure 20), but this may be because it is somewhat thicker. However, its microstructure may also have been influenced by phenomena such as alpha particle recoil.

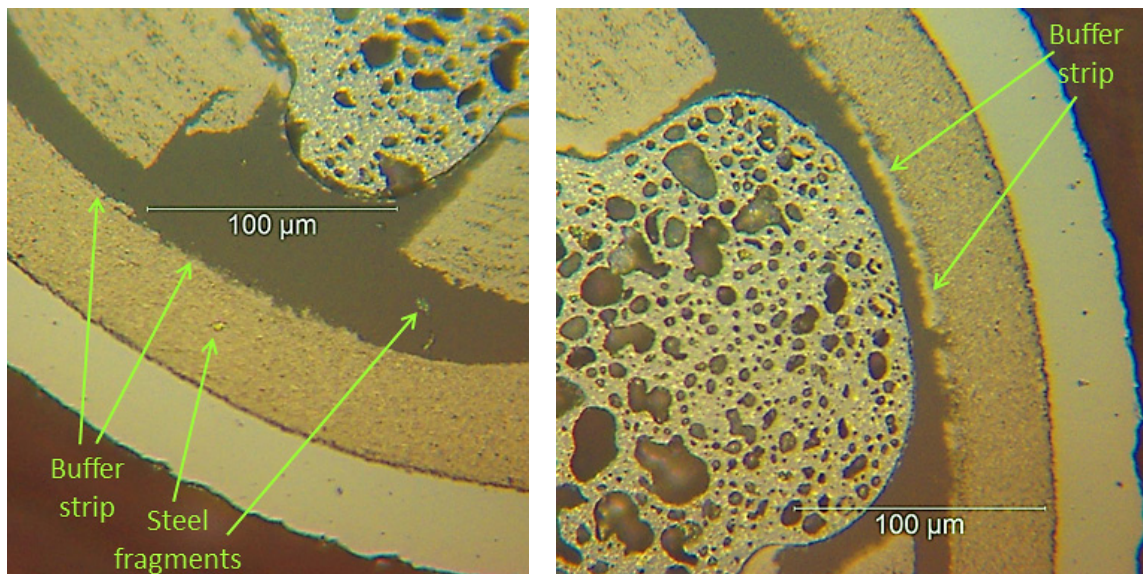


Figure 20. Thin strips of buffer adhering to the IPyC interior near kernel protrusions in particle AGR1-531-038.

### 6.1.3 Particle AGR1-531-019 (Mount 21U)

Type ABi particle AGR1-531-019 (relatively low Ag-110m M/C ratio) was ground within approximately 77  $\mu\text{m}$  of its SiC midplane (based on the average size of a burned-back Variant 1 particle). As shown in Figure 21, radial features surrounding this particle suggest that the epoxy embrittled from radiation damage during the long period of unplanned storage. Within the particle, a substantial thickness of buffer adhered to the IPyC interior along most of the interface, indicating that the buffer-IPyC bond was often stronger than the buffer itself. The residual bonding over the upper-left of the buffer-IPyC interface was strong enough to prevent complete debonding from buffer densification. Figure 21 also reveals unusual thin features of low porosity within the kernel. The pattern resembles the network of fractures observed in some other irradiated AGR-1 kernels; therefore, these features may represent kernel cracks that formed and subsequently “healed” during irradiation.

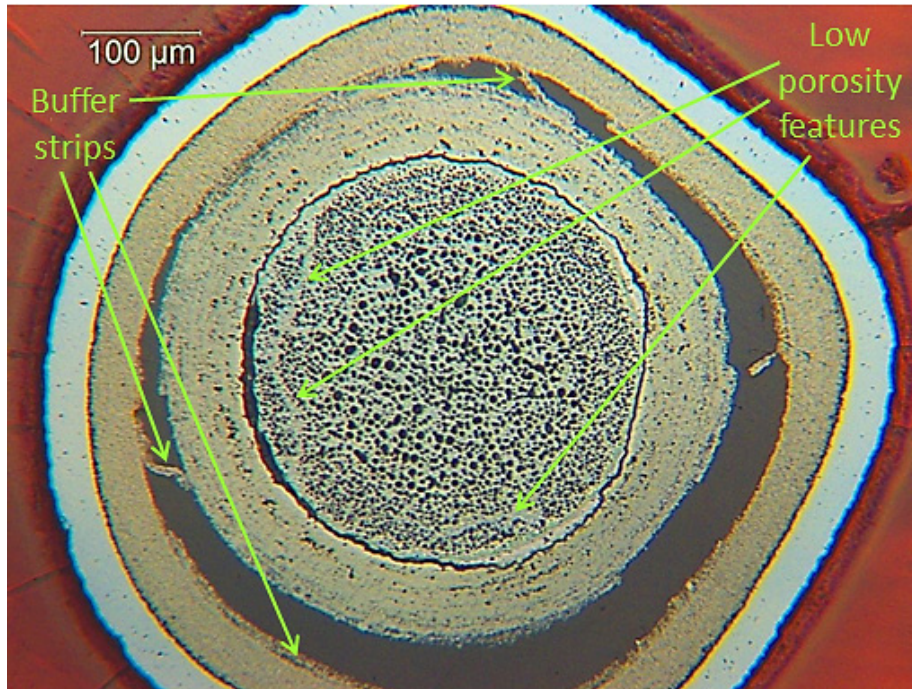


Figure 21. Outer buffer peeling and unusual kernel features in particle AGR1-531-019.

### 6.1.4 Particle AGR1-531-006 (Mount 22U)

Type Ai particle AGR1-531-006 (high Ag-110m M/C ratio) was ground within approximately 94  $\mu\text{m}$  of its SiC midplane (based on the average size of a burned-back Variant 1 particle). Grinding ceased deliberately before midplane on this particle to investigate anomalous behavior observed during early grinding. As with the other Compact 5-3-1 single particle mounts, Mount 22U was ground for 2-minute intervals with a 600-grit disc once the particle was reached, with a periscope inspection between each interval. After the second interval, which should not have penetrated the SiC, an irregular dark area was observed that suggested a patch of thin SiC had broken out. However, no IPyC could be seen through the opening. Small scratches were also found in the epoxy, which were attributed to small SiC fragments in the absence of shiny stainless steel fragments. After another coarse grinding interval, deep scratches were found across the entire mount and the SiC layer appeared extensively fractured. The interpretation at the time was that the SiC “caved in” under the minimal grinding force (10 N) before shattering into abrasive fragments, which rapidly caused further damage by impacting the particle. This tentative explanation implied that the SiC ground thus far had little or no underlying support from IPyC. After back-potting, Mount 22U was briefly ground with a very coarse 220-grit disc to remove most of the SiC fragments

without causing deeper damage. This was followed by 600-grit and 1200-grit grinding before following the standard polishing routine. The result is presented in Figure 22.

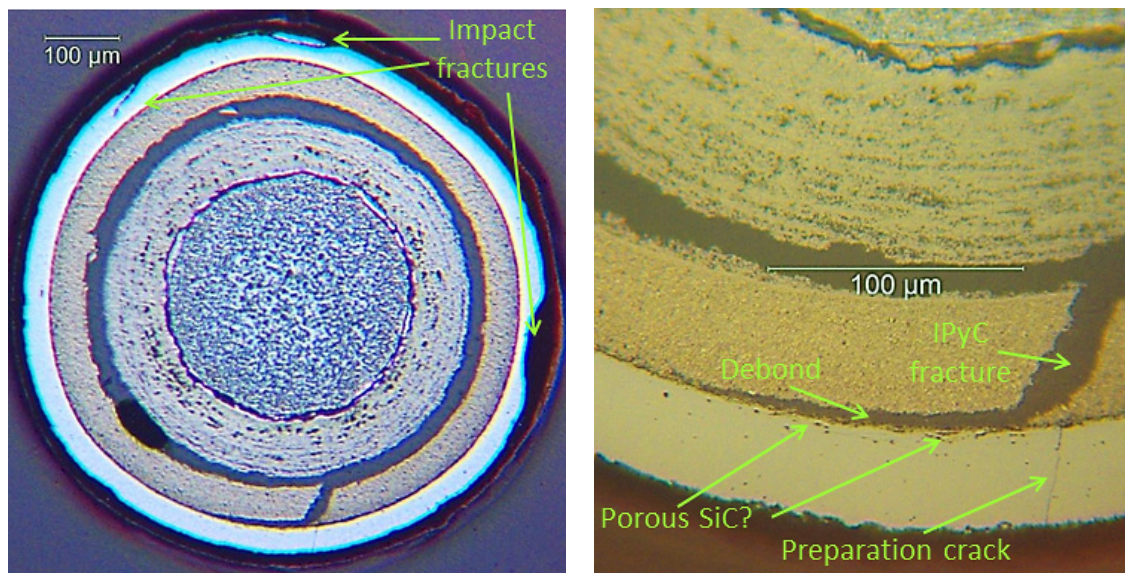


Figure 22. SiC fractures from preparation (left) and details near IPyC fracture (right) in particle AGR1-531-006.

As indicated in the left portion of Figure 22, some of the impact fractures from the early preparation remained in the SiC. However, grinding any deeper might have obliterated any features that could help to explain the anomalous behavior during grinding. Figure 22 clearly demonstrates that some of the SiC was indeed unsupported by IPyC. After the IPyC fractured, one side debonded from the nearby SiC. The IPyC that debonded may have been attached to the buffer at a different elevation, because buffer densification could have pulled the IPyC inward. IPyC-SiC debonding likely was more extensive in the particle portion ground away for the SiC to crush inward under minimal grinding force. IPyC-SiC debonds can also be precursors to tangential SiC fractures (Ploger et al. 2012), which would have further weakened the SiC. The right portion of Figure 22 highlights a radial crack extending through the SiC layer that aligns with the IPyC fracture. However, this through-wall SiC crack must have occurred during sample preparation because particle AGR1-531-006 exhibited no evidence of cesium loss during irradiation (the Cs-134 M/C ratio was 0.91, compared to an average of 0.91 for all particles, discussed in Section 3.2).

Another potential explanation for a large IPyC-SiC debond is a soot inclusion, which occurs when over-fluidized IPyC-coated particles pick up low-density carbon soot from coating chamber walls. This can also create porosity in the inner SiC layer (Hunn and Lowden 2006b) and a concentration of small pores that apparently exist in the SiC along the debonded area. Nevertheless, no foreign material can be seen in the right portion of Figure 22 within the debonded region; therefore, a soot inclusion cannot be confirmed. The apparent SiC porosity could also conceivably indicate mild corrosion by Pd fission products.

The IPyC behavior observed in this particle (i.e., IPyC fracture and localized debonding from the SiC layer) has been identified as a key precursor to SiC failure (Hunn et al. 2014a). Another AGR-1 Variant 1 particle from Capsule 5 (AGR1-523-SP01) was found to have released cesium during irradiation. This particle had similar IPyC behavior and was found to have extensive Pd corrosion of the SiC layer near the IPyC crack. This corrosion was attributed as the ultimate cause of SiC failure and cesium release (Hunn et al. 2014b). Particle AGR1-531-006 is therefore of significant interest because it may represent a similar particle that was in the intermediate stages of SiC failure when the irradiation

ended. Further analysis of this particle with more advanced microanalysis techniques will be presented in a separate report.

### 6.1.5 Particle AGR1-531-031 (Mount 23U)

Type Af particle AGR1-531-031 (high Ag-110m M/C ratio) was ground within approximately 80  $\mu\text{m}$  of its SiC midplane (based on the average size of a burned-back Variant 1 particle). As indicated in Figure 23, the flattest side of the buffer at the upper right probably was originally aligned with the faceted left side of the IPyC and SiC layers. The buffer and enclosed kernel were evidently free to rotate until the radial gap was filled with back-potted epoxy. The thin radial crack at the top of the buffer may have formed late in irradiation from the combination of kernel swelling and buffer densification inducing a large hoop stress, but grinding damage cannot be entirely discounted as a cause. The unusual color surrounding the kernel in Figure 23 likely represents residue from the alcohol used to wipe the mount surface before loading on the metallograph. In the process, alcohol occasionally wicks into (and later seeps out of) narrow features such as the separation between the kernel and uranium carbide skin and the separation between the skin and the buffer (both displayed in the right image in Figure 23). Interference fringes from such a stain are definitely present over the back-potted epoxy on the lower left of this particle.

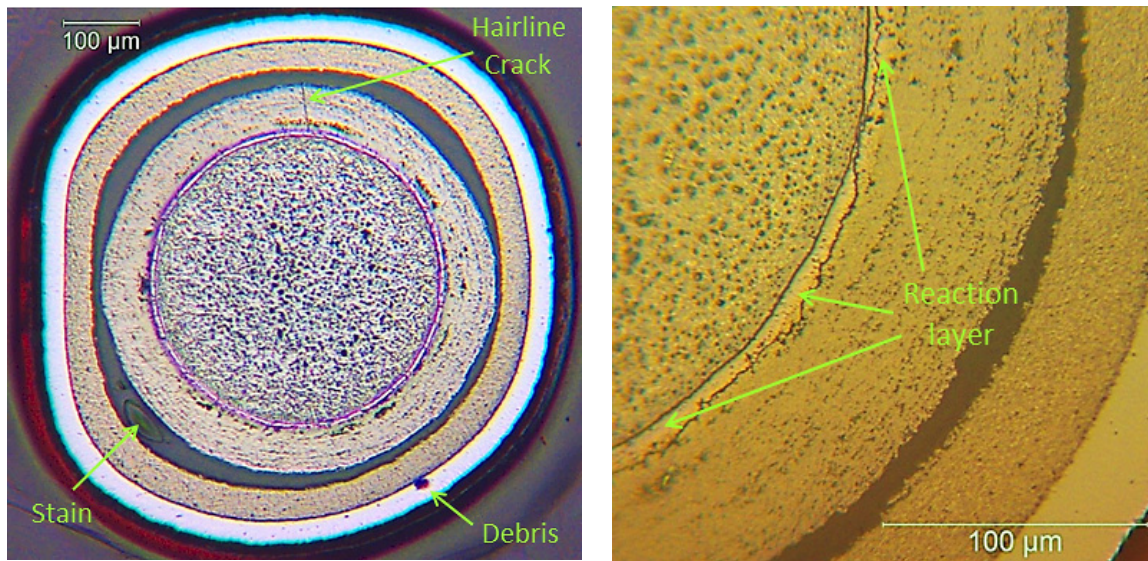


Figure 23. Rotated buffer inside IPyC layer (left) and uranium carbide skin separation (right) in particle AGR1-531-031.

### 6.1.6 Particle AGR1-531-033 (Mount 24U)

The measured radius in the ground plane of particle AGR1-531-033 (high Ag-110m M/C ratio) is 364  $\mu\text{m}$ , which is larger than the computed average as-fabricated SiC radius for Variant 1 AGR-1 fuel of 361  $\mu\text{m}$  (Maki 2009). This particle is thus somewhat larger than average; however, actual size cannot be determined in the absence of a sharply defined silhouette image. Similarly, while it is likely to be close to the IPyC-SiC midplane, exactly how close is unknown. As shown in Figure 24, back-potting was not completely effective in filling the buffer-IPyC gap. This relatively common Type Ai particle has some loose debris on its surface (i.e., in this case, loose fibers from the wiping cloth).

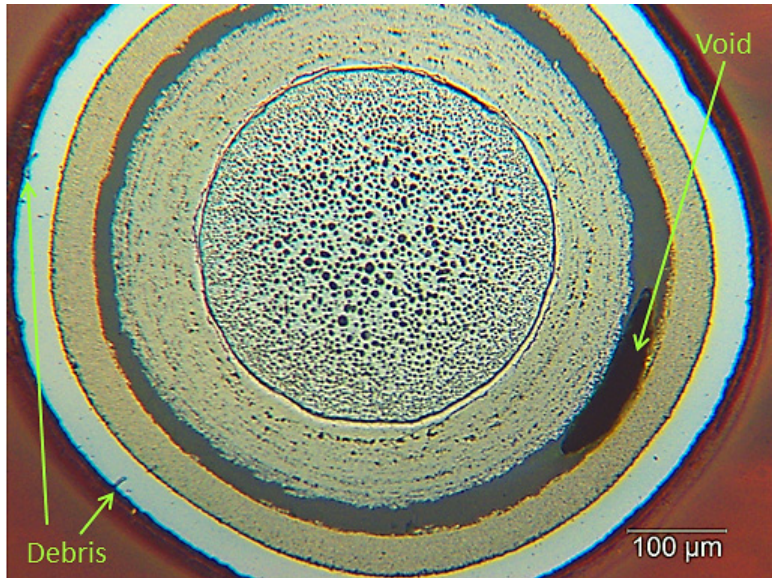


Figure 24. Type Ai particle AGR1-531-033.

**6.1.7 Particle AGR1-531-018 (Mount 25U)**

Type ABf particle AGR1-531-018 was investigated because it contained less than one-fourth of the average inventory of radioisotopes in the individually gamma-counted Compact 5-3-1 particles (Table 7). The correspondingly lower radiation damage in the surrounding epoxy permitted the silhouette to be discerned on the metallograph. Measuring the silhouette radius and the ground SiC radius established that this particle was ground 39 μm from the true SiC midplane. The radius of the round portion of the kernel (excluding the kernel protrusion in the left portion of Figure 25) is 188 μm, compared to the average as-fabricated kernel radius of 175 μm (Maki 2009). Although AGR-1 kernels swelled during irradiation (Ploger et al. 2012), there is no indication that this kernel was substantially undersized before irradiation; therefore, kernel size cannot explain the low inventory of fission products. Furthermore, the kernel microstructure shown at higher magnification in the right portion of Figure 25 appears very typical of normal irradiated kernels. Thus, ceramography could not determine the reason for the low measured inventories of fission products.

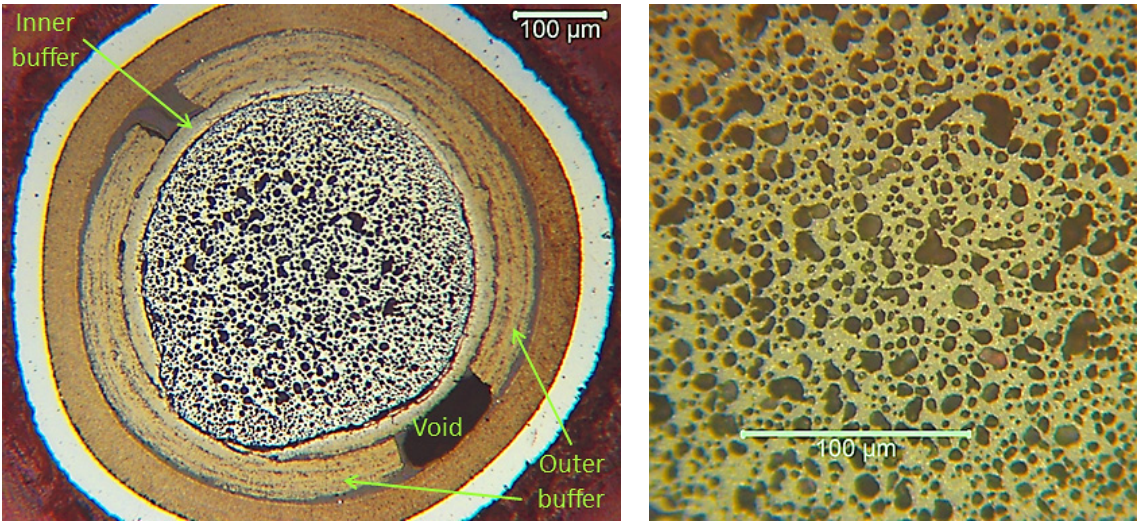


Figure 25. Buffer fracture pattern (left) and kernel microstructure (right) in particle AGR1-531-018.

The buffer fracture pattern in the left portion of Figure 25 is noteworthy. The radial fractures only go through the outer buffer portion, while the inner buffer opening is at a different azimuth. Buffers may separate circumferentially at mid-radius if sufficient porosity concentrates there during deposition. Such particles have infrequently been cross-sectioned without intersecting the outer buffer, presenting an unrealistically thin buffer in the plane of polish and exaggerated gap thickness across the entire particle in the ground plane. As mentioned in Section 6.1, Mount 25U did not receive a polish with 0.04- $\mu\text{m}$  colloidal silica in the interest of time, which is why the SiC in the left portion of Figure 25 is slightly rougher than for other particles.

### **6.1.8 Fission Product Behavior**

Ceramography was unable to detect any definite relationship between fission product behavior and internal particle morphology. All three particles with higher Ag-110m M/C ratios exhibited intact buffers, but two of three particles with lower ratios also had intact buffers (at least in their ground planes). Even after densification, AGR-1 buffers show considerable porosity; therefore, intact buffers would not be expected to inhibit Ag diffusion significantly. Particle AGR1-531-006 was found to contain a fracture through the dense IPyC layer, but it retained most of its Ag-110m.

Lastly, despite its fractured buffer, the optical appearance of particle AGR1-531-018 provided no clear clues on why this particle's inventory of all gamma-detected fission products was low relative to the average values. Nevertheless, the relatively sharp silhouette confirmed the smaller amount of radiation damage in the surrounding epoxy, which corresponds to the lower overall fission product activity measured in this particle.

## **6.2 Mount U4**

### **6.2.1 Preparation and Examination**

Soft Micarta (a laminar composite based on thermosetting plastic) was used as a mount material for Mount U4 (as displayed in Figure 26). Ninety-nine burned-back particles (subjected to the full DLBL process but not gamma-counted) were randomly selected by pouring on a glass slide and picking them with the vacuum needle. The particles were poured into the mount onto a piece of thick, double-sided adhesive tape stretched across the mount base. Particles tended to land toward the mount center. The tape was backed by a glass slide to hold the particles in place while Buehler EpoHeat two-part epoxy was poured into the mount. The epoxy was cured in a furnace for 90 minutes at 55°C. As with the steel single particle mounts, an annular groove inside the lower part of the mount encouraged most of the epoxy meniscus from curing shrinkage to form at the mount top. However, curing also produced an uneven mount base with some stagger in particle elevations.

The glass-backed tape was left in place for pneumatic transfer to HFEF. After arriving there, Mount U4 had to be stored for over a year before it could be prepared. Considerable radiation damage occurred to the epoxy in this interval, especially embrittlement of epoxy adjacent to the particles by beta radiation. Substantial gas also was trapped among closely grouped particles when the epoxy was poured. In combination, these effects resulted in poorly bound particles when clustered. The initial back-pot was performed as soon as 600-grit grinding opened some large gas bubbles. However, this was only partially successful because further grinding with a 1,200-grit disc both opened new cavities and dislodged some of the back-pot (despite the vacuum impregnation). The back-pot appeared to adhere poorly to severely embrittled epoxy, which also impeded back-pot penetration into adjacent voids. A second back-pot was performed. After grinding off surplus epoxy, the first level was ready for a 3- $\mu\text{m}$  polish, which was adequate to reveal features of interest on the metallograph. At this point, approximately 70 particles had been exposed, but only 19 contained exposed kernels to enable morphological classification in the context of Appendix C. Although most of the 70 particles were not yet ground deeply enough to expose kernels, more than 19 particles could have been classified except for loss of kernels during the grinding or polishing (often with their surrounding buffers). Images of the 19 particles were captured with the

Jenoptik ProgRes C14+ camera. Numerical identifiers were assigned according to particle positions in a low-resolution macrophotograph taken of Mount U4 with an in-cell camera.

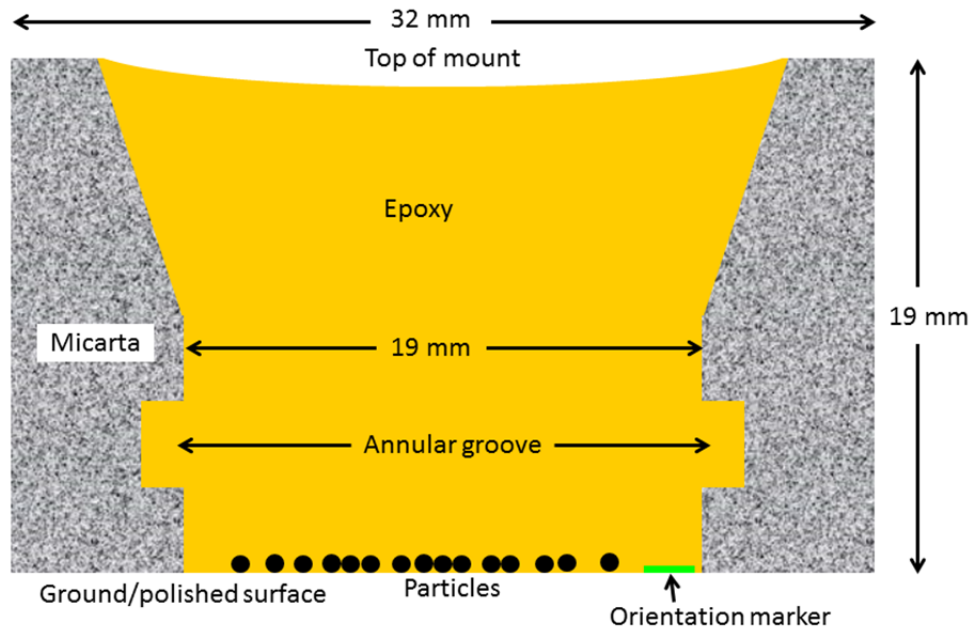


Figure 26. Design and particle loading arrangement in Mount U4.

This general approach was followed to prepare and examine eight more levels. Distances between levels were measured at the mount center with the thickness gauge (Figure 17); grinding time and force were kept consistent to maintain spacing near 50  $\mu\text{m}$ . (Somewhat more material was ground off between the first and third levels to expose more kernels.) However, because Mount U4 may not have been ground evenly, spacing measured between levels at the mount center would not necessarily be accurate for particles closer to the periphery. Thickness measurements were further compromised by “spongy” embrittled epoxy near central particles, which deformed by varying amounts under the dial indicator probe pressure. The rounded probe tip sometimes produced a dimple in the resilient surface, whose depth depended on the support provided by the underlying back-pot at each level.

Back-pots were performed between the third and fourth levels and between the sixth and seventh levels to limit losses of kernels, buffers and kernels, and entire particles. Nevertheless, as indicated in Figure 27, back-potting was only partially successful at stabilizing internal particle structures. Much of the damage shown occurred during preparation of the sixth level when an entire particle pulled out and broke up into fragments that rapidly damaged other particles.

Back-potting was not always effective at penetrating the embrittled epoxy surrounding particles, as demonstrated by the left side of Figure 28. Here a particle rotated in its socket of original epoxy after grinding had exposed the buffer and after two back-pots had been performed. After the rotation, the next back-pot had a large open region next to the ground portion to enter and hold the particle in position. Several particles in Figure 27 behaved this way. However, other particles with superficially similar appearances in Figure 27 did not rotate but merely were partially covered with surplus back-pot (as displayed in the right side of Figure 28). This sort of particle often was located within a bubble of trapped gas that became impregnated by epoxy during back-potting. The original epoxy underlying such particles could still be “spongy” and compress under grinding pressure rather than grinding the same amount as neighboring regions. As a consequence, even particles in relatively close proximity would not necessarily grind uniformly. Nevertheless, particle rotations and thin, partial back-pot coverings usually did not interfere with morphological investigations and particle classifications.

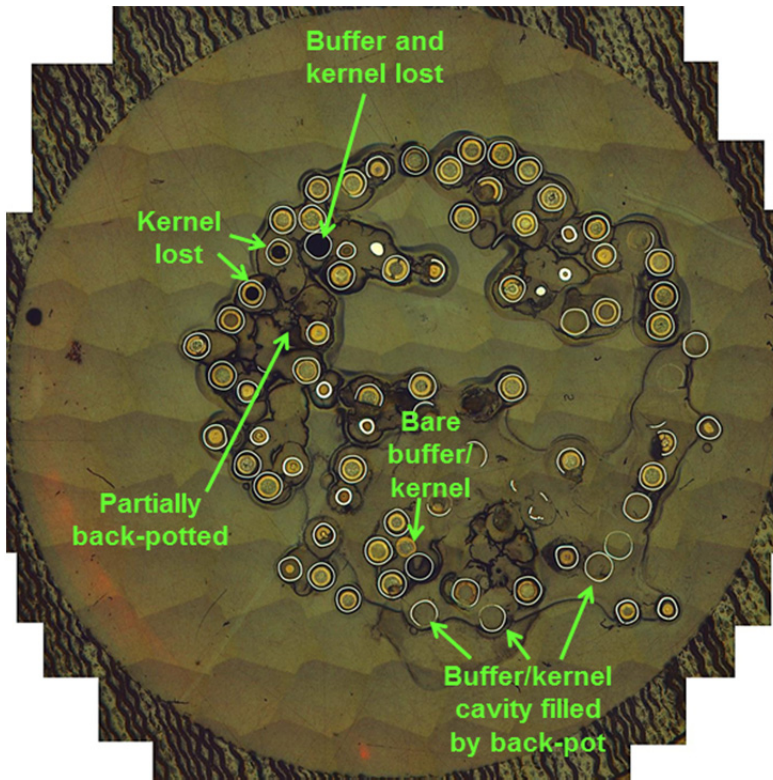


Figure 27. Montage of Mount U4 at the seventh level examined.

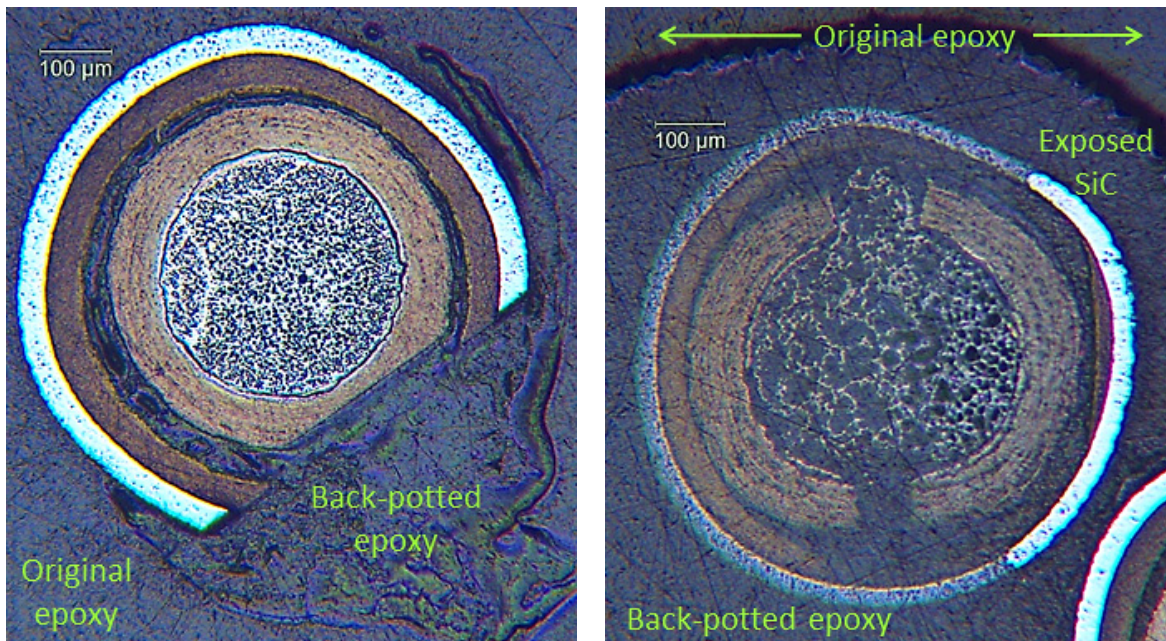


Figure 28. Mount U4 particles at seventh level, rotated after some grinding (left) and partially covered by back-pot (right).

## 6.2.2 Mount U4 Ceramography Results

Ultimately, 79 of the 99 particles in Mount U4 were classified at one or more levels, with 75 at two or more levels. On average, each of the 79 Mount U4 particles was classified at 4.5 levels. Most of the 20 particles that could not be classified were severely damaged before their kernels were exposed, although kernels were never reached in a few deeply recessed particles.

Morphological classification results are presented in Figure 29, where the Mount U4 multi-level percentages are contrasted with values determined by only considering level 5 of Mount U4 and the single level classification results from one transverse and two longitudinal cross sections through Compact 5-1-2 (Ploger et al. 2012). Figure 29 shows a somewhat lower percentage of Type Ai particles for multiple levels in Mount U4 than for level 5 and a correspondingly higher percentage of Type ABi particles for multiple levels than for level 5. This trend was expected because a single level can miss localized regions of buffer-IPyC bonding, causing a Type AB particle to be classified erroneously as a Type A. A similar trend was expected between Type Af and Type ABf particles for the same reason, but no difference is found in Figure 29 between the multi-level and level 5 percentages (perhaps due to the smaller number of particles with fractured buffers). Both Compacts 5-3-1 and 5-1-2 are AGR-1 Variant 1 fuel, although Compact 5-3-1 had somewhat higher burnup, fast fluence, and irradiation temperatures. Nevertheless, no definite relationships were uncovered between particle morphologies and irradiation conditions among AGR-1 compacts (Ploger et al. 2012); therefore, differences between level 5 of Mount U4 and Compact 5-1-2 may primarily reflect the number of particles examined in level 5. In any case, although Figure 29 suggests reasonable consistency between multi-level and single level classifications, larger Compact 5-3-1 sample sizes would be needed to come to more definite conclusions in this regard.

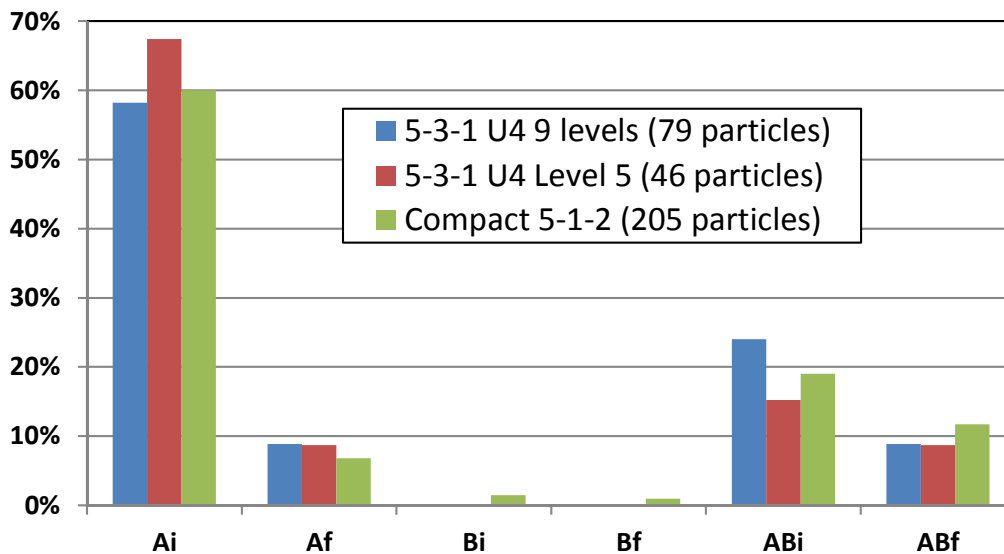


Figure 29. Mount U4 multi-level results (average 4.5 levels) versus single level results from Mount U4 and Compact 5-1-2 cross sections.

Ceramographic examinations on Mount U4 particles included investigation of fractures in the IPyC and SiC layers, as well as debonding between these layers. Four of the 79 classified particles revealed a crack through the IPyC layer at one or more levels, and IPyC-SiC debonding was observed at each crack tip. All four particles were Type AB, two of which had a fractured buffer. These IPyC crack data from Mount U4 are included in Figure 30, along with results from AGR-1 compact cross sections (Ploger et al. 2012), and they reinforce key findings from compact ceramography. Specifically, the likelihood of through-IPyC cracks was much greater in irradiated Variant 1 fuel (AGR-1 Capsule 5), which may be related to its relatively low IPyC density (Hunn and Lowden 2006a). In addition, the IPyC crack frequency was appreciably greater in Type ABf particles than in Type ABi for each fuel variant (Ploger et al. 2012).

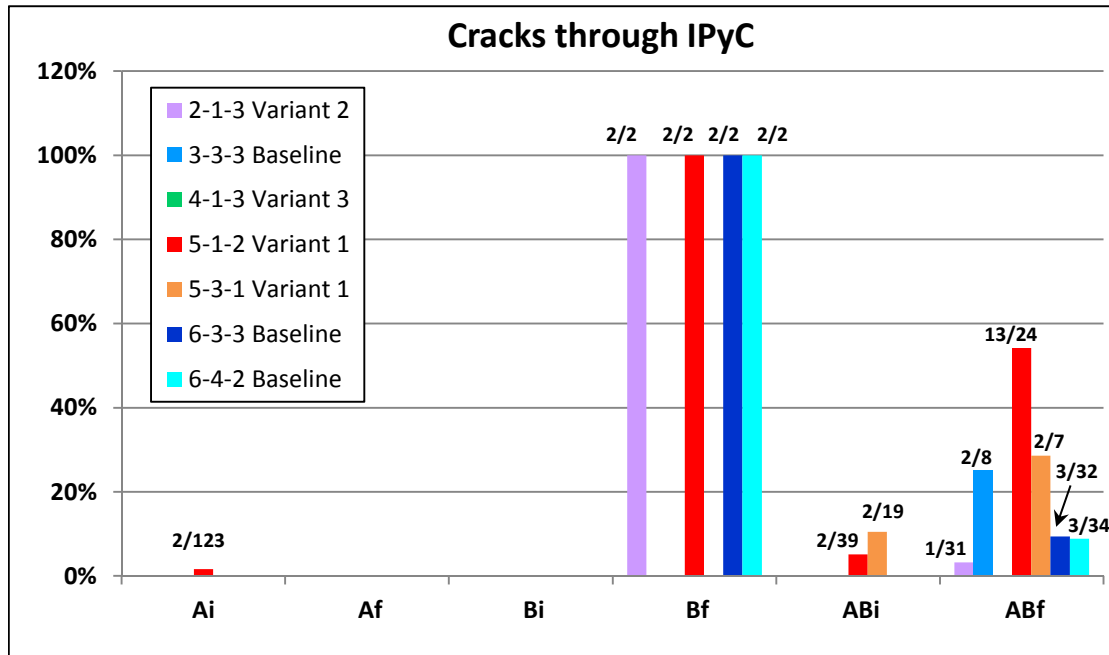


Figure 30. Frequency of IPyC cracks by particle type for cross-sectioned AGR-1 compacts and deconsolidated, burned back particles in Compact 5-3-1 Mount U4.

Mount U4 produced some results differing from compact ceramography. Whereas all four Type AB particles with IPyC cracks in Mount U4 exhibited IPyC-SiC debonds, only seven of fifteen Type AB particles with IPyC cracks in Compact 5-1-2 showed such debonds (Ploger et al. 2012). This appears to be a result of the multi-level examination in Mount U4 because IPyC-SiC debonds tend to be more localized than IPyC cracks (i.e., multi-level examination was more likely to identify the debonds compared to single-level examinations). One Type ABf particle on Mount U4 displayed a debond in one of two levels that showed an IPyC crack, while another Type ABf exhibited a debond in two of three levels with an IPyC crack. A Type ABi particle revealed a debond in two of five levels with an IPyC crack.

Only one particle (Type ABi) contained an IPyC-SiC debond at every level with IPyC cracks. This unusual Type ABi particle is presented in Figure 31 and Figure 32. It not only exhibited IPyC cracks and IPyC-SiC debonds at all six levels (Mount U4 Levels 4 through 9), but it also had fractured SiC in all six levels. Figure 31 suggests that the internal structure changed in the following sequence:

1. Buffer-IPyC debonding began (probably at the upper left side) in response to buffer densification.
2. Buffer-IPyC debonding progressed in both directions along the interface until locally strong bonding was encountered on the right and lower left sides.

3. IPyC fractures occurred where buffer-IPyC debonding had arrested, which may reflect the weak Variant 1 IPyC layer, because buffer shrinkage stresses there likely could alternatively have been accommodated by buffer fractures.
4. IPyC-SiC debonds initiated at the IPyC crack tips as the shrinking buffer pulled the IPyC inward.
5. IPyC-SiC debonding progressed until the tangential stress in the inner SiC at the debond tip exceeded the tensile strength of the SiC, when tangential SiC cracks began to propagate (Miller et al. 2004).

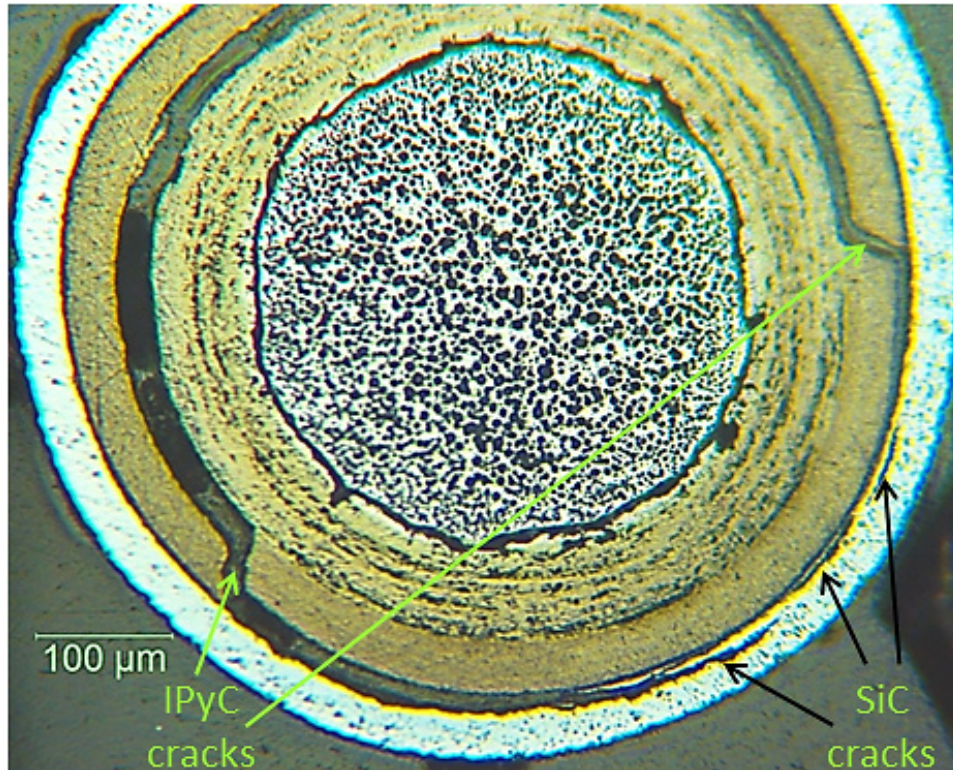


Figure 31. The only Mount U4 particle with SiC cracks, shown at the sixth polish level examined.

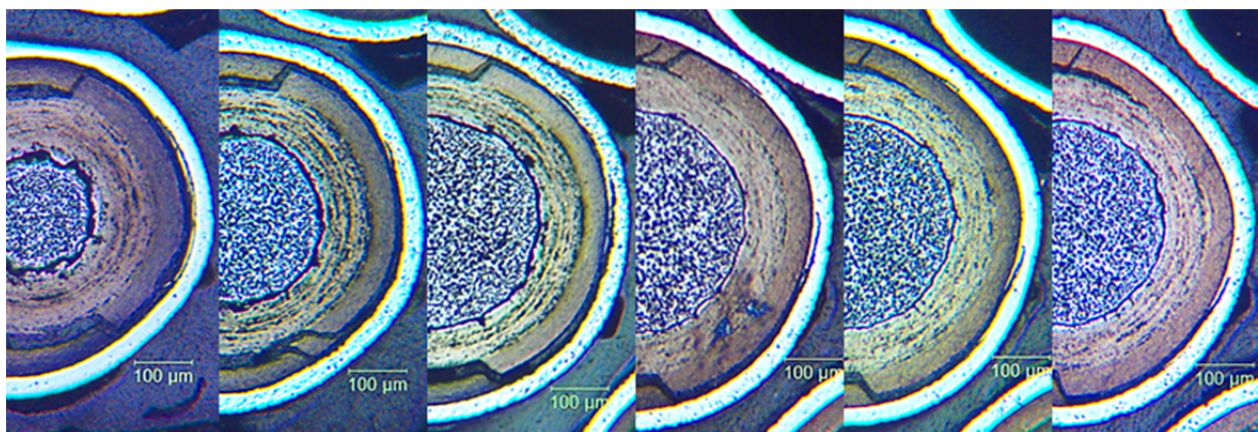


Figure 32. IPyC cracks, IPyC-SiC debonds, and SiC fractures from Level 4 (left) to Level 9 (right).

The analysis above is not completely adequate for the Figure 32 composite, especially for SiC fractures that evidently propagated tangentially both in the ground planes and perpendicular to them without breaching the entire SiC thickness. In images from the fourth and fifth mount levels, the IPyC layer fully debonded from the SiC layer; therefore, the SiC cracks observed here likely initiated at different elevations. Furthermore, the extensive SiC fracture in the leftmost image in Figure 32 (Level 4) is not clearly connected to the SiC cracks in Levels 6 through 9, and it may have initiated higher in this particle where no image was captured in the absence of an exposed kernel. The short SiC crack in the level 5 image could be connected to SiC cracks in either level 4 or level 6. The SiC cracks in levels 6, 7, and 8 are probably connected because they occur in pairs at each level, but it is not possible to be certain. More levels at even finer spacing would be needed to resolve such three-dimensional issues.

AGR-1 compact ceramography found SiC fractures only in Type Bf particles, although SiC cracks were also found in two particles without any exposed kernel that could not be classified (Ploger et al. 2012). The Type ABi particle in Figure 31 and Figure 32 demonstrates that SiC cracks can form in other morphological types. However, this may only be true for Variant 1 fuel.

### **6.3 Future Work**

The selected single-particle mounts described in this section have been transferred to the electron microscopy laboratory for further analysis with advanced microanalysis techniques, including scanning electron microscopy and energy-dispersive spectroscopy. Sample preparation will be performed with the focused ion beam, followed by further detailed specimen analysis, including transmission electron microscopy and scanning transmission electron microscopy with elemental analysis. These analyses will focus primarily on more detailed and higher-resolution investigation of fission product migration behavior in the particle coating layers, especially the SiC layer. The results of these investigations will be presented in a separate report.

## **7. COMPACT 5-3-1 POST-IRRADIATION EXAMINATION RESULTS SUMMARY**

Key findings from the destructive PIE of Compact 5-3-1 are summarized as follows:

- The compact contained no particles with failed SiC or TRISO coatings (based on DLBL results).
- Approximately 1% of the predicted inventory of Ag-110m was retained in the compact outside of SiC. Silver release from particles spanned a very large range (Ag-110m M/C ratio values ranged from 1.05 to less than 0.15 for 58 gamma counted particles). No obvious correlations between particle morphology and silver release were observed based on a small sample set of seven particles analyzed in cross section with optical microscopy.
- Cerium and europium were found in the compact at levels greater than the equivalent inventory in one particle, indicating the release of small quantities through intact SiC. Levels of strontium were almost as high.
- The inventory of cesium in the compact outside of the SiC was very small (i.e., the compact fraction of Cs-134 and Cs-137 recovered in DLBL solutions was  $2.45 \times 10^{-6}$  and  $6.46 \times 10^{-6}$ , respectively).
- DLBL data revealed that a Pd-105 compact fraction of  $5.43 \times 10^{-3}$  was found in the compact outside of the SiC, indicating release through intact coatings at a similar level as silver.
- A study of separated kernels and coatings indicated several particles with very little cesium retention in kernels, while others had relatively high retention. The reasons for this behavior are not obvious, but could be related to kernel microstructure.
- This study also suggests that most fission products residing in the particle, but outside the kernel, are located in the buffer layer.

- Europium exhibited the highest fraction located outside the kernel (most likely with the majority in the buffer layer) of the fission products detected by gamma counting.
- Ceramography was unable to determine why a low inventory of fission products was measured in particle AGR1-531-018; however, the lower radiation damage seen in the surrounding epoxy relative to other single-particle mounts qualitatively confirmed the basic gamma counting result that this particle had much lower radioisotope inventory.
- The morphology of the kernel, buffer layer, and IPyC layer in the deconsolidated Compact 5-3-1 particles examined is generally similar to that observed during ceramography of AGR-1 compact cross sections. Specifically, many particles displayed a continuous gap between the buffer and IPyC layers that was driven by buffer densification and followed by buffer-IPyC debonding during irradiation. Partial debonding occurred in many other particles along the observable buffer-IPyC interface. Approximately 18% of the particles examined exhibited fractures in the buffer layer.
- IPyC fracture tendencies observed in deconsolidated Compact 5-3-1 particles reinforced findings from ceramography of Compact 5-1-2 cross sections. AGR-1 Variant 1 fuel was found to be more likely than other variants to contain fractures through the entire IPyC layer with IPyC-SiC debonds at the crack tips. IPyC-SiC debonds were found more frequently in particles with IPyC cracks when the particles were examined at multiple levels.
- One of the individually cross-sectioned particles (AGR1-531-006) was notable in that it exhibited an IPyC fracture and small IPyC-SiC delamination, but no observable buffer fracture within the plane of polish. PIE of other AGR-1 fuel compacts and particles has indicated that IPyC fracture and IPyC-SiC delamination could be a precursor to failure of the SiC layer by focused palladium attack (Hunn et al. 2014a). Therefore this particle is of interest, as it may represent a particle that was in the preliminary stages of SiC failure by this mechanism at the end of irradiation. This particle has been preserved for microanalysis and comparison with particles with similar coating morphology but failed SiC layers.

## 8. LESSONS LEARNED AND RECOMMENDATIONS

Extensive use of blanks should be employed during the DLBL process. This will aid in interpretation of the ICP-MS data, which is susceptible to influence by natural contamination.

Additional studies have been recommended in regard to the analysis of separated kernels and coating fragments (Section 5.3). These include repeating the analysis with fresh fuel to obtain data on silver segregation in the kernels and coating layers, performing follow-on microanalysis on selected particles to investigate possible causes of the varied level of cesium retention in different kernels, and repeating the study with the use of nondestructive, three-dimensional particle analysis to understand specific particle morphology prior to attempting to remove the coating layers.

In mounts where many particles are loaded in close proximity, gas trapped between particles after epoxy has been poured should be removed under vacuum to better bind the particles to epoxy. Mounts should be ground and polished as soon as practicable after loading to limit radiation damage to the epoxy surrounding the particles.

## 9. REFERENCES

Barnes, C. M., W. C. Richardson, D. Husser, M. Ebner, 2008, "Fabrication Processes and Product Quality Improvements in Advanced Gas Reactor UCO Kernels," *Proceedings of the 4th International Topical Meeting on High Temperature Reactor Technology, HTR2008, Washington, DC, USA, September 28 – October 2, 2008*, HTR2008-58039.

- Bower, G. R., S. A. Ploger, P. A. Demkowicz, J. D. Hunn, 2016, "Measurement of Kernel Swelling and Buffer Densification in Irradiated UCO TRISO Particles," submitted to *Journal of Nuclear Materials*, November 2016
- Chadwick, M. B., et al., 2011, "ENDF/B-VII.1 Nuclear Data for Science and Technology: Cross-Sections, Covariances, Fission Product Yields and Decay Data," *Nuclear Data Sheets*, Vol. 112, pp. 2887-2996. Specific decay data accessed at: <http://www.nndc.bnl.gov/exfor/endl00.jsp>.
- Collin, B. P., 2015, *AGR-1 Irradiation Test Final As-Run Report*, INL/EXT-10-180097, Rev. 3, Idaho National Laboratory.
- Demkowicz, P.A., 2010, *AGR-1 Post-Irradiation Examination Plan*, PLN-2828, Rev. 1, Idaho National Laboratory.
- Demkowicz, P. A., L. Cole, S. Ploger, P. Winston, 2011, *AGR-1 Irradiated Test Train Preliminary Inspection and Disassembly First Look*, INL/EXT-10-20722, Idaho National Laboratory.
- Demkowicz, P., J. Harp, P. Winston, S. Ploger, 2012, *AGR-1 Fuel Compact 6-3-2 Post-Irradiation Examination Results*, INL/EXT-12-27123, Idaho National Laboratory.
- Demkowicz, P. A., J. M. Harp, P. L. Winston, S. A. Ploger, 2013, *Analysis of Fission Products on the AGR-1 Capsule Components*, INL/EXT-13-28483, Idaho National Laboratory.
- Demkowicz, P. A., J. M. Harp, P. L. Winston, S. A. Ploger, I. J. van Rooyen, 2016a, *AGR 1 Compact 4-1-1 Post-Irradiation Examination Results*, INL/EXT-15-36169, Idaho National Laboratory.
- Demkowicz, P. A., S. A. Ploger, P. L. Winston, J. M. Harp, 2016b, *AGR-1 Compact 3-2-1 Post-Irradiation Examination Results*, INL/EXT-15-36352, Idaho National Laboratory.
- Grover, S. B., D. A. Petti, J. T. Maki, 2010, "Completion of the First NGNP Advanced Gas Reactor Fuel Irradiation Experiment, AGR-1, in the Advanced Test Reactor," *Proceedings of HTR-2010, Prague, Czech Republic, October 18-20, 2010*, Paper 104.
- Harp, J. M., 2014, *Analysis of Individual Compact Fission Product Inventory and Burnup for the AGR-1 TRISO Experiment Using Gamma Spectrometry*, ECAR-1682, Rev. 2, Idaho National Laboratory.
- Hawkes, G. L., 2012, *AGR-1 Daily As-Run Thermal Analyses*, ECAR-968, Rev. 3, Idaho National Laboratory.
- Hunn, J. D., A. K. Kercher, P. A. Menchhofer, J. R. Price, 2005, *Results from ORNL Characterization of Nominal 350  $\mu\text{m}$  NUCO Kernels from the BWXT 59344 Batch*, ORNL/TM-2005/541, Oak Ridge National Laboratory.
- Hunn, J. D., F. C. Montgomery, P. J. Pappano, 2006, *Data Compilation for AGR-1 Variant 1 Compact Lot LEU01-47T-Z*, ORNL/TM-2006/508, Oak Ridge National Laboratory.
- Hunn, J. D., R. A. Lowden, 2006a, *Data Compilation for AGR-1 Variant 1 Coated Particle Composite LEU01-47T*, ORNL/TM-2006/020, Rev. 1, Oak Ridge National Laboratory.
- Hunn, J. D., R. A. Lowden, 2006b, *Data Compilation for AGR-1 Baseline Coated Particle Composite LEU01-46T*, ORNL/TM-2006/019, Oak Ridge National Laboratory.
- Hunn, J. D., G. E. Jellison Jr., R. A. Lowden, 2007, "Increase in Pyrolytic Carbon Optical Anisotropy and Density during Processing of Coated Particle Fuel Due to Heat Treatment," *Journal of Nuclear Materials*, Vol. 374, p. 445.
- Hunn, J. D., C. A. Baldwin, T. J. Gerczak, F. C. Montgomery, R. N. Morris, C. M. Silva, P. A. Demkowicz, J. M. Harp, S. A. Ploger, 2014a, "Detection and Analysis of Particles with Failed SiC in AGR-1 Fuel Compacts," *Proceedings of the 7th International Topical Meeting on High*

*Temperature Reactor Technology (HTR2014), Weihai, China, October 27-31, 2014, HTR2014-31254.*

- Hunn, J. D., C. A. Baldwin, T. J. Gerczak, F. C. Montgomery, R. N. Morris, C. M. Silva, 2014b, *AGR-1 Irradiated Compacts 5-2-3 and 5-2-1 PIE Report: Evaluation of As-Irradiated Fuel Performance with Leach-Burn-Leach, IMGA, Materialography, and X-ray Tomography*, ORNL/TM-2014/171, Oak Ridge National Laboratory.
- INL, 2015, *Technical Program Plan for INL Advanced Reactor Technologies Technology Development Office/Advanced Gas Reactor Fuel Development and Qualification Program*, PLN-3636, Rev. 4, Idaho National Laboratory.
- Maki, J. T., 2009, *AGR-1 Irradiation Experiment Test Plan*, INL/EXT-05-00593, Rev. 3, Idaho National Laboratory.
- Ploger, S. A., P. A. Demkowicz, J. D. Hunn, J. S. Kehn, 2012, *Ceramographic Examinations of Irradiated AGR-1 Fuel Compacts*, INL/EXT-12-25301, Rev. 1, Idaho National Laboratory.
- Sterbentz, J.W., 2011, *JMOCUP As-Run Daily Depletion Calculation for the AGR-1 Experiment in the ATR B-10 Position*, ECAR-958, Rev. 1, Idaho National Laboratory.
- Sterbentz, J. W., 2013, *JMOCUP As-Run Daily Depletion Calculation for the AGR-1 Experiment in the ATR B-10 Position*, ECAR-958, Rev. 2, Idaho National Laboratory.
- van Rooyen, I. J., D. E. Janney, B. D. Miller, P. A. Demkowicz, J. Riesterer, 2014, "Electron Microscopic Evaluation and Fission Product Identification of Irradiated TRISO Coated Particles from the AGR-1 Experiment: A Preliminary Review," *Nuclear Engineering and Design*, 271, pp. 114-122.

## **Appendix A**

### **Deconsolidation-leach-burn-leach Procedure**

# Appendix A

## Deconsolidation-leach-burn-leach Procedure

The majority of the functions performed by the MFC Analytical Laboratory in support of the AGR PIE occur in the MFC-752 Hot Cells. Each of the six cells, also known as the Junior Caves, has a nominal 6 × 5-ft floor area, 2-ft-thick concrete walls, a shielding window, and two Central Research Laboratory manual manipulators. They are supplied with compressed air, vacuum, and miscellaneous electrical and electronic connections integral to the cell. Tubing is available to provide liquid chemicals if direct flow is required. The cells have an air atmosphere and are maintained at a negative pressure to provide contamination control. Materials from the Hot Fuels Examination Facility or the Fuel Conditioning Facility may be received via pneumatic rabbit in Analytical Hot Cell 1 and transferred to other hot cells by a chain-driven cart that connects Hot Cells 1 through 6.

The Analytical Laboratory performs the deconsolidation and leach-burn-leach cycles according to Laboratory Instruction AL-5000-LI-018, “Electrolytic Deconsolidation and Leach-Burn-Leach Method.” The task is to deconsolidate the compact, electrochemically breaking down the compact carbonaceous matrix and releasing the TRISO particles. The particles and matrix debris are then subjected to two 24-hour cycles submerged in hot concentrated nitric acid in a Soxhlet extractor. The particles and debris are transferred to a muffle furnace, where all exposed carbon is oxidized at 750°C in air for 72 hours. The burned-back particles and any remaining residue are then returned to the Soxhlet extractor for another two 24-hour extraction cycles in 16 M nitric acid.

The compact is received via pneumatic rabbit in Analytical Laboratory Hot Cell 1 and is transferred to Hot Cell 5 by a chain-driven cart that connects Cells 1–6. The compact is removed from the modified aluminum Swagelok bulkhead fitting that serves as a container and is weighed on the remote function balance in Cell 4. The weight is taken by placing the compact in a clean, tared glass scintillation vial and transferring it to the balance for measurement.

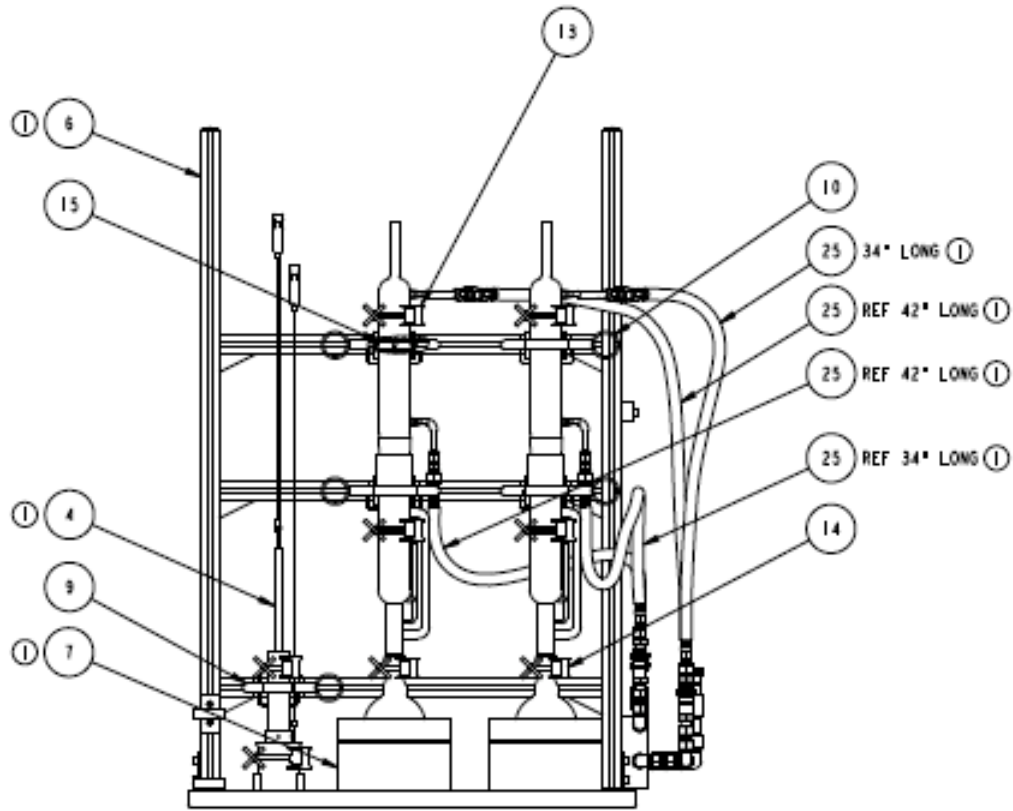
Once the compact weight is recorded, it is returned to Cell 5, where it is put into a clean, single-use deconsolidation tube. The entire deconsolidation setup is shown in Figure A-1. The deconsolidation tube is a 28-mm outer diameter glass tube that has a grating that supports the compact while the acid and applied electrical current break down the matrix. Based on experimentation during process development, it was concluded that a grating with 4-mm perforations allowed the particles to drop through with minimal plugging by the partially decomposed matrix. The deconsolidation tube fits loosely inside the Soxhlet thimble, which is a fused silica tube that has a porous No. 2 fused silica frit in the bottom that allows acid to flow through, but traps the majority of solids. The deconsolidation tube containing the compact is placed inside the thimble, which is in turn placed inside a glass tallform beaker. The two electrodes for the deconsolidation step are made of 20-gauge platinum-rhodium wire. The cathode is placed in the acid, either between the thimble and the deconsolidation tube, or between the thimble and the tallform beaker. The anode is a platinum-rhodium wire that has been threaded through a glass tube that is flared at the base to form an “elephant foot.” The anode wire is coiled at the bottom end to increase the contact area where it sits on the compact. The beaker is filled with 4 M nitric acid to nearly the level of the bottom of the compact. The Tenma Model 72-6908 DC power supply is energized and the current set at 1 amp. Acid is added until current flow is established, and the beaker is filled to cover approximately the bottom 1 mm of the compact. During system development and testing, it was determined that more coverage led to larger quantities of the matrix flaking off and partially plugging the perforated support in the deconsolidation tube. An open crossbar support test showed large pieces falling through before the matrix was uniformly broken down. The 4-mm perforated support was chosen as an effective compromise.



Figure A-1. Deconsolidation configuration.

The Soxhlet extractor system is composed of two standard glass units made in three sections: the boiling flask (situated in a heating mantle), the center section (where the thimble containing the specimen is located and where condensation collects and periodically drains through siphon action), and the water cooled condenser located on top. Two units were installed in Cell 5 on the basis that it might be necessary to perform leach cycles in parallel. By procedure, the boiling flask is filled with 150 mL of concentrated nitric acid and placed in the heating mantle, the center section is inserted in the boiling pot, and the thimble is placed inside the center section. The condenser is then attached and chilled water flow initiated. The chiller is installed outside the cell, at the rear, and maintains water temperature at 10°C with a flow of approximately 3.8 liters per minute. The chiller is interlocked so that the heating mantles cannot be energized unless a minimum water flow is maintained. The acid vapor rises to the top, is condensed, and drains down to fill the volume containing the thimble. Periodically, this volume fills to the level of a siphon tube that drains the collection volume back to the boiling flask. In this manner, the specimen is continually flushed with freshly condensed acid solution. The assembly is shown in Figure A-2.

For heating, the Soxhlet boiling flasks are placed into electrical resistance mantles. The heating mantles are installed in Cell 5 and shown as item 7 in Figure A-2. The heater is operator controlled and monitored outside the cell at the Cell 5 and 6 power control panel.



- I ASSEMBLY

Figure A-2. Framework with deconsolidation tube/vial (left) and two Soxhlet extractor stations.

The muffle furnace used for the burn-back phase is a Vulcan Model 3-55A bench top furnace, modified for installation in Hot Cell 5. An out-of-cell controller was fabricated to keep the electronics out of the radiation field. In this application, the furnace uses two 120-volt elements that are operated as individual heaters, departing from the manufacturer's configuration where the elements are wired in series and operated at 240 volts. In the manufacturer's arrangement, a failure of either heater element would disable the furnace. The manufacturer's data indicates that one heater element is capable of maintaining the oven at 750°C. Using the elements independently minimizes the need for heating element replacement in the event of failure. The furnace is equipped and controlled by a Type K thermocouple that is connected via the existing Hot Cell 5 Type K thermocouple wiring. An additional backup thermocouple has been installed in the furnace. The furnace is equipped with a door interlock switch and a fan. The door interlock switch de-energizes the heaters when the furnace door is not closed. The low-voltage direct current fan is powered by the temperature controller.

Following the two pre-burn leach cycles, the Soxhlet thimble containing the particles is transferred to the muffle furnace. The furnace is heated to 750°C and held at this temperature for 72 hours. Air flow is maintained by adjusting the fan voltage on the external control panel to provide a detectable movement of the pinwheel mounted over the exhaust chimney. Once the desired duration is reached, the furnace is allowed to cool to <70°C and the thimble is returned to the Soxhlet extractor to perform the post-burn leaches.

The two post-burn leaching steps are performed with the same procedure described above for the pre-burn leaches. The particles are allowed to air dry in the thimble following completion of the final post-burn leach cycles. When dry, the particles are transferred to a metal storage container from which fractions are removed for particle inspection and selection.

The deconsolidation and two pre-burn leaches are expected to provide information on fission products that were external to the SiC layer and leached from the remaining matrix debris. These leach solutions would also provide information on any failed particles present in the compact, as the kernels would be exposed following deconsolidation and would be dissolved in the nitric acid solution. The post-burn leaches provide two basic pieces of information. If any particles are present with defective or otherwise failed SiC layers (cracked or porous SiC but intact pyrocarbon), the kernels will be exposed by the burning of intact pyrocarbon and dissolved in the nitric acid solution. As the burn step will also burn all of the remaining matrix debris as well as the outer pyrolytic carbon layers, the post-burn leaches will also dissolve any fission products that remained in these components and could not be dissolved during the pre-burn leaches. In the absence of any particles with defective SiC, the total of all leach solutions should provide a total measure of fission products that were present outside of the SiC layers in the compact.

## **Appendix B**

### **Particle Inspection and Irradiated Microsphere Gamma Analysis**

## Appendix B

### Particle Inspection and Irradiated Microsphere Gamma Analysis

Following any of the deconsolidation-leach-burn-leach steps, particles can be visually inspected using a custom-designed optical macroscopy system. Individual particles can then be selected for specific purposes such as gamma spectrometry, burnup analysis, or microscopy. After completion of the second post-burn leach step, the particles are allowed to air dry and are then transferred from the thimble to a metal can for storage and handling. A fraction of the particles contained in the can (nominally 200 to 500 particles at a time) is transferred to an inspection dish, which is viewed on the shielded Leica macroscope that is installed in MFC Analytical Laboratory Hot Cell 5. The macroscope is connected to the control computer through a custom wall penetration that maintains shielding integrity.

A Leica Z16APO modular macroscope is oriented horizontally, viewing the sample array from below by a front surface mirror (Figure B-1 and Figure B-2). The horizontal reflex configuration allows shielding to be installed to protect the camera. It also requires a minimal working footprint. Viewing from below allows a clear overhead for particle manipulation and reduces interference with master slave manipulators. The Leica Z16 is equipped with an 8-megapixel DFC-490 CCD color camera that allows live video imaging at medium resolution and still image acquisition at high resolution. The unit is equipped with a 0.5x objective lens that allows a working distance of 187 mm, maximizing distance between the radiation source and the optics and electronics while minimizing the working envelope. The lens combination provides a 16:1 zoom capability that yields a field of view ranging from approximately 26 mm × 26 mm to 1.6 mm × 1.6 mm, meaning that a maximum of ~1000 particles could be viewed at the minimum magnification of 9x, and 4 particles at the maximum of 144x. The digital image is communicated via a combination Firewire-Ethernet cable to the computer located outside the cell and displayed on the computer monitor. Images are captured and saved on the computer.

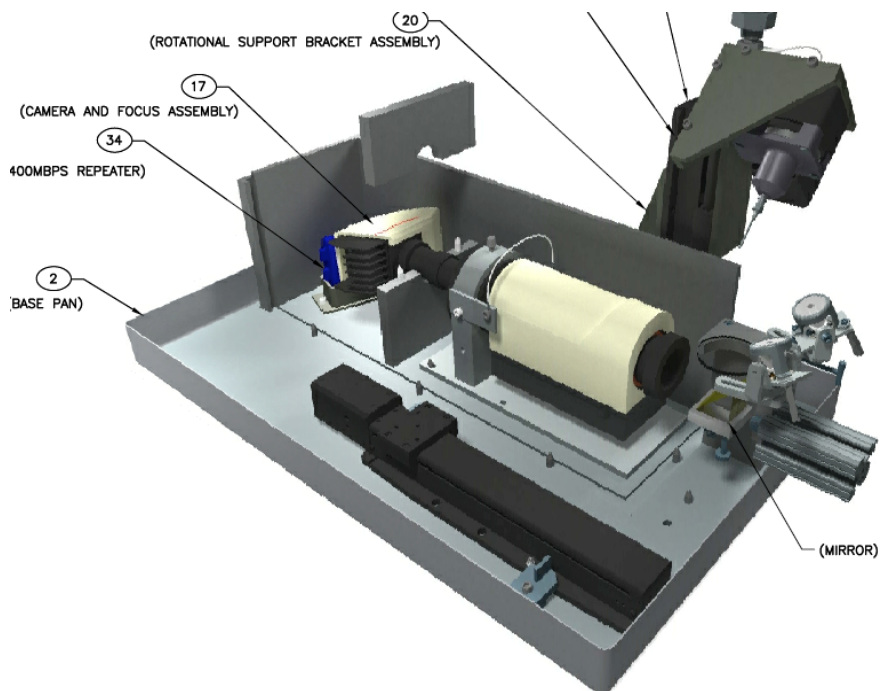


Figure B-1. Cutaway view of the camera optical orientation without shielding.

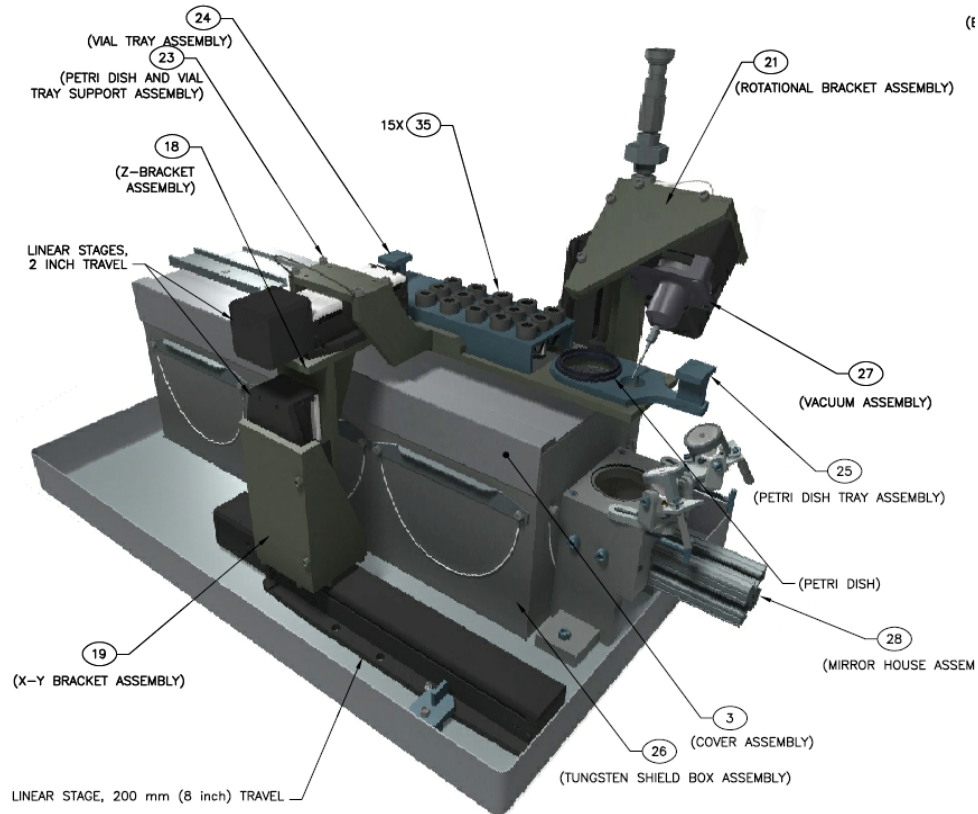


Figure B-2. Assembled isometric view of macroscope stages and shielding.

Particles placed on the optically flat glass inspection dish are viewed from below, which allows the selection needle to pick up particles from above. Lighting is provided by two high-intensity variable light-emitting diodes that are mounted in pivot posts on the top of the macroscope mirror box. This arrangement allows for some adjustment of shadow and highlight, but imperfect uniformity. When particles are placed on the inspection dish for viewing, the dish stage can be translated to view the dish and the focus adjusted as needed. Newmark stepper motor-driven linear stages are used to position the viewing dish and vial tray platform in the x, y, and z directions as well as to raise and lower the vacuum needle during particle selection. The stages are controlled with joysticks that are able to achieve a nominal 0.2-mm precision of movement. Manual control using visual input from the macroscope and through the cell window allows the operator to achieve a consistent needle and visualization position, minimizing the need for electronic positioning tracking. Selected particles are picked up using a vacuum tweezer needle, photographed, and then placed in glass V-vials for gamma spectrometry measurements. The needle stage moves up and down and can rotate the needle to allow a 360-degree view. Figure B-3 shows a particle attached to the vacuum needle.



Figure B-3. Post deconsolidation particle viewed on the end of the vacuum tweezer needle.

Once particles have been selected from the inspection dish, they can be moved to individual Wheaton 0.3-mL V-vials, which are held in a rack on the inspection dish stage, as shown in Figure B-2. Fifteen vials are arranged in the rack, which has an open bottom through which the V-vial can be viewed from below using the camera. The vacuum needle that is holding a particle is raised above rack height, and the stage is positioned to align the needle with an open V-vial. The needle is then lowered into the mouth of the vial, the vacuum is shut off, and as the vacuum leaks off, the particle drops into the vial. This is confirmed visually by watching the macroscope image on the computer screen.

Once particles have been selected and placed in the vials, the vials can be transferred to Analytical Laboratory Hot Cell 4, which is equipped with a gamma ray spectrometer that is located outside the hot cell, with gamma radiation transmitted through a port in the rear of the cell, as shown in Figure B-4.

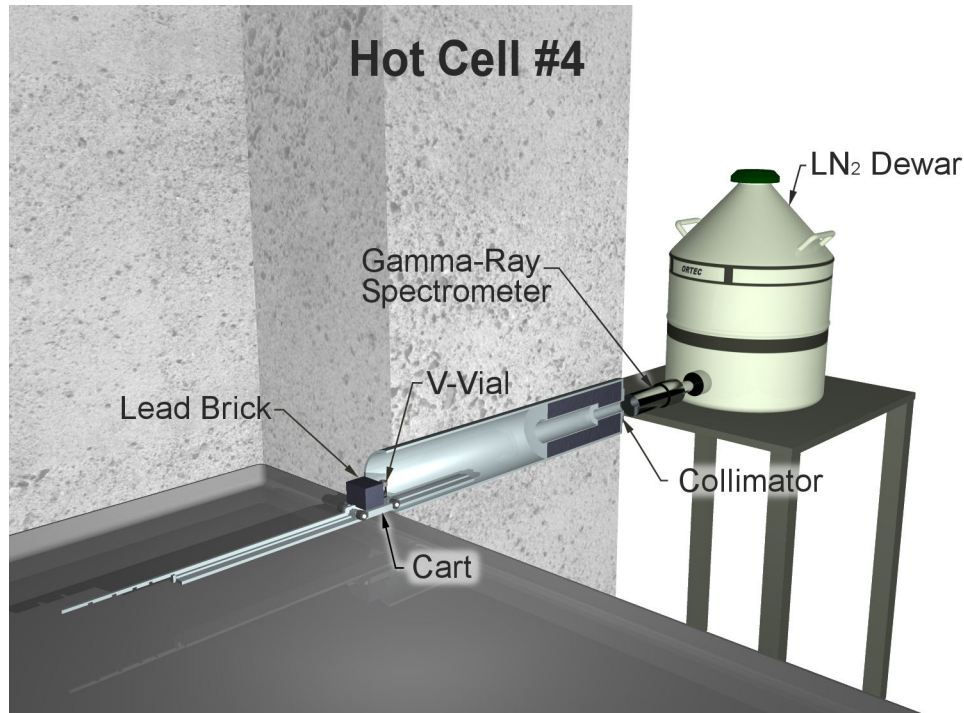


Figure B-4. MFC Analytical Laboratory Cell 4 spectrometer configuration.

The vial is positioned on the cart and moved to the position nearest the collimator to minimize the amount of background radiation from other sources inside the cell. The gamma spectrometer is an 18%-efficient Canberra germanium-lithium crystal that generates a signal that is parsed into specific energies by a Canberra Multi-Channel Analyzer, and the spectrum is further analyzed using Apex software. The system is calibrated for particle measurement using a National Institute for Standards and Technology traceable Eu-152 source plated onto a polyethylene bead that approximates the size of a TRISO particle in a glass vial of the type used to hold the particles for counting.

The analysis in the Apex software quantifies any isotopes with measurable gamma emissions. The measured activity is based on a weighted average of all the detected gamma rays from a particular isotope, with weight given to the primary gamma-ray (typically the gamma ray with the highest branching ratio) and diminishing weight given to other gamma rays as their branching ratio decreases. Gamma rays with poor statistics or with known interferences are not used in the weighted average. Isotopes of particular interest include Ag-110m, Cs-134, Cs-137, Ce-144 (determined by measuring gamma emissions from Ce-144 and the daughter isotope Pr-144), Eu-154, Eu-155, and Ru-106 (determined by measuring gamma emissions from the daughter isotope Rh-106). After the collected, irradiated microsphere gamma analysis spectra were initially surveyed to identify which fission products were available for analysis, an AGR-1 specific library was created containing isotope, primary gamma energy, secondary gamma energy, and branching ratio. It included the isotopes of particular interest listed above. The default Apex library values for these isotopes were used with some notable exceptions. The primary gamma ray energy for Ag-110m was changed from 657 to 884 keV to alleviate difficulties in resolving the 657 keV Ag-110m gamma from the leading tail of the much more intense Cs-137 662 keV gamma. The other Ag-110m lines often had too few counts in the peak for quantification. In addition to the primary isotopes of interest, the activities of several other isotopes or their minimum detectable activities were reported including activation products Co-58, Co-60, Eu-152, and Mn-54 and fission products Zr-95 (and its Nb-95 daughter) and Ru-103.

## **Appendix C**

# **Ceramographic Morphology Classification**

## Appendix C

### Ceramographic Morphology Classification

A comprehensive scheme for classifying AGR-1 particle morphologies was developed for analysis of cross-sectional particle images taken during ceramography of cross sections from six irradiated AGR-1 fuel compacts (Ploger et al. 2012). Several characteristic morphologies came to be recognized as these images were examined. The most common feature was a radial gap between the buffer and IPyC layers where the buffer densified inward (outer surface moved toward kernel) during irradiation. In some particles with inward buffer densification, the radial buffer-IPyC gap was interrupted by regions where the buffer stayed firmly bonded to the IPyC layer. Many of these particles debonded along most of the interface, while debonding was much less extensive on some other particles when the AGR-1 irradiation ended. The rarest case was where a particle had no buffer-IPyC gap. In these cases, the buffer stayed bonded to the IPyC layer around the entire circumference in the plane of the cross section examined. The buffers in these particles still evidently densified, but the inner buffer surface moved radially outward rather than the outer buffer surface moving inward. Kernels in these particles often had larger pores than seen inside kernels within inwardly densified buffers.

The scheme for classifying irradiated AGR-1 particles by morphology in the plane of polish is presented with representative examples in Figure C-1. A radial buffer-IPyC gap around the entire circumference (completely detached buffer-IPyC interface) is designated as Type A end-state morphology. Particles with fully bonded buffer and IPyC layers are termed Type B particles. Debonding along only part of the buffer-IPyC interface is called Type AB morphology. Buffer fracturing occasionally occurred in Types A, B, and AB, which resulted in the six characteristic morphologies displayed in Figure C-1.

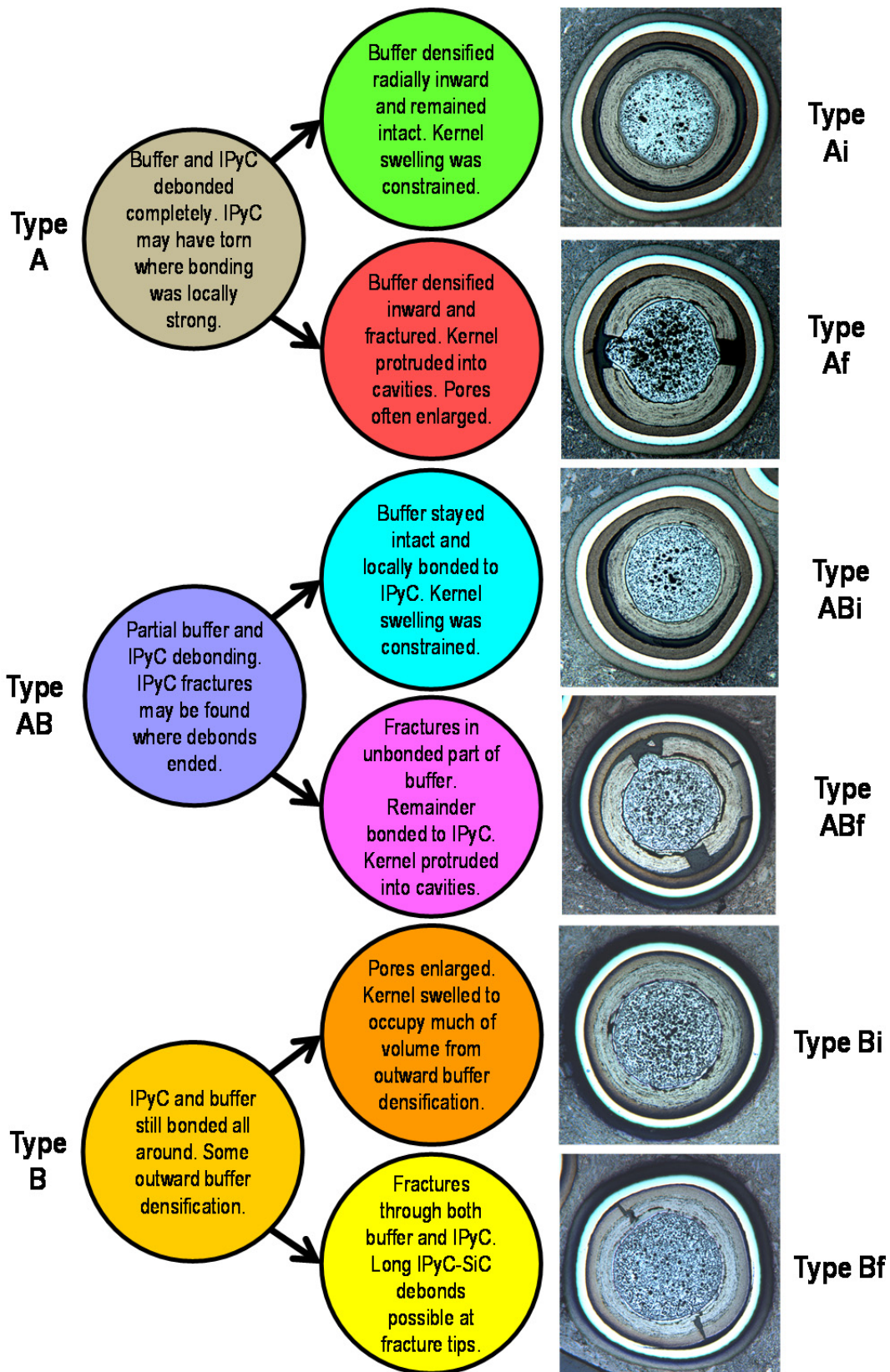


Figure C-1. Particle morphologies observed in AGR-1 fuel particle cross sections, where “i” denotes an intact buffer and “f” denotes a fractured buffer (Ploger et al. 2012).